Space and Time-Resolved Measurements at the Breakdown of the Quantum Hall Effect

Von der Gemeinsamen Naturwissenschaftlichen Fakultät
der Technischen Universität Carolo-Wilhelmina
zu Braunschweig

zur Erlangung des Grades eines
Doktors der Naturwissenschaften
(Dr. rer. nat.)

genehmigte

Dissertation

von

Bülent Erol Sağol

aus Adana-Türkei

1. Referent: Prof. Dr. G. Nachtwei

2. Referent: Prof. Dr. R. J. Haug (Universität Hannover)

Eingereicht am: 27.1.2003

Disputation am: 3.4.2003

(Druckjahr: 2003)

Publications of the Dissertation

Teilergebnisse aus dieser Arbeit wurden mit Genehmigung der Gemeinsamen Naturwissenschaftlichen Fakultät, vertreten durch den Mentor, in folgenden Beiträgen vorab veröffentlicht:

1. G. Nachtwei, N.G. Kalugin, B.E. Sağol, Ch. Stellmach, G. Hein,"*Function principle of a relaxation oscillator based on a bistable quantum Hall device*", Appl. Phys. Lett. **82**, 2068 (2003).

2. B.E. Sağol, G. Nachtwei, N.G. Kalugin, G. Hein, K. Eberl, "*Supercritical nondissipative currents in quantum Hall systems*", 26th International Conference on the Physics of Semiconductors (ICPS-26) Edinburgh, Scotland (2002).

3. B.E. Sağol, G. Nachtwei, N.G. Kalugin, G. Hein, K. Eberl, "*Suppressed breakdown and enforced reappearance of the quantum Hall effect in Corbino devices*", 15th International Conference on High Magnetic Fields in Semiconductor Physics (SemiMag-15) Oxford, England (2002).

4. B.E. Sağol, G. Nachtwei, K. von Klitzing, G. Hein, K. Eberl,"*Time scale of the excitation of electrons at the breakdown of the quantum Hall effect*", Phys. Rev. B 66, 075305 (2002).

5. K. Güven, R.R. Gerhardts, I.I. Kaya, B.E. Sağol, G. Nachtwei,"*Two-level model for the generation and relaxation of hot electrons near the breakdown of the quantum Hall effect*", Phys. Rev. B 65, 155316 (2002).

6. B.E. Sağol, G. Nachtwei, K. von Klitzing, K. Eberl, "*Short-pulse excitation of quantum Hall systems: delocalization times and inelastic scattering lengths of hot electrons*", Physica B 314, 268 (2002).

7. B.E. Sağol, G. Nachtwei, I.I. Kaya, K. von Klitzing, K. Eberl, "*Space and time-resolved measurements of electronic excitation in quantum Hall conductors*", Proceedings of the 25th International Conference on the Physics of Semiconductors, Osaka, Japan-2000, edited by N. Miura and T. Ando, Springer Proceedings in Physics (Springer, New York, 2001), Vol. 87, Pt. II, p. 959.

8. I.I. Kaya, G. Nachtwei, B.E. Sağol, K. von Klitzing, K. Eberl, "*Spatial evolution of the generation and relaxation of excited carriers near the breakdown of the quantum Hall effect*", Physica E 6, 128 (2000).

9. G. Nachtwei, I.I. Kaya, B.E. Sağol, K. von Klitzing, K. Eberl, "*Spatially resolved measurements of hot electron generation and relaxation at the breakdown of the quantum Hall effect*", Physica B 272, 127 (1999).

Contents

List of Figures

List of Tables

1 Introduction

In 1980 von Klitzing discovered the quantum Hall effect (QHE) in a two-dimensional electron system (2DES), realized with a Silicon metal-oxide-semiconductor field-effect transistor at liquid Helium temperatures and strong magnetic fields [1]. The quantization was observed in the Hall resistivity ρ_{xy}, which exhibited plateaus at values of $\rho_{xy}=h/ie^2$, where h is the Planck constant, e the elementary electron charge and i an integer number, which represents the number of completely filled Landau levels. At each plateau of the Hall resistivity, the longitudinal resistivity ρ_{xx} vanishes, indicating a dissipationless current flow. The resistance quantum $R_K=h/e^2$ is named as the von Klitzing constant and corresponds to the value 25812.807 Ω. The high accuracy of the quantization, the reproducibility and the independence from the sample geometry have led the QHE in 1990 to be accepted as an international resistance standard. For his discovery, von Klitzing was awarded the Nobel prize in physics in 1985 [2].

The discovery of von Klitzing opened a new era in the physics of low dimensional electron systems. Just two years after his discovery, in 1982, Tsui and Störmer have discovered another quantized Hall plateau of $\rho_{xy}=3h/e^2$, accompanied by a minimum in ρ_{xx}, when the lowest energy, spin-polarized Landau level was filled by the fraction 1/3 [3]. This was the discovery of the fractional quantum Hall effect, and one year later in 1983, Laughlin presented variational ground-state and excited-state wave functions [4], which explained this effect. For their discoveries Laughlin, Störmer and Tsui were awarded the Nobel prize in physics in 1998 [5, 6, 7].

A typical sample for QHE measurements is shown in Fig. 1.1 (a). The dark surfaces represent the ohmic contacts, which are contacted to the 2DES below the surface of the GaAs crystal. At temperatures below 4.2 K, a current I is applied between the main contacts 1 and 4. Between contacts 5 and 6 the longitudinal voltage V_x and between contacts 3 and 5 the Hall voltage V_{Hall} are measured, both as a function of the perpendicular magnetic field B. Fig. 1.1 (b) shows the results of such a QHE measurement. At certain magnetic field values the Hall resistivity $\rho_{xy}=V_{Hall}/I$ exhibits plateaus and the longitudinal resistivity $\rho_{xx}=(V_x/I)/(w/l)$ vanishes.

Shortly after the discovery of the QHE, experiments were performed to determine the physical limits of the effect [8, 9]. Not only the sample properties

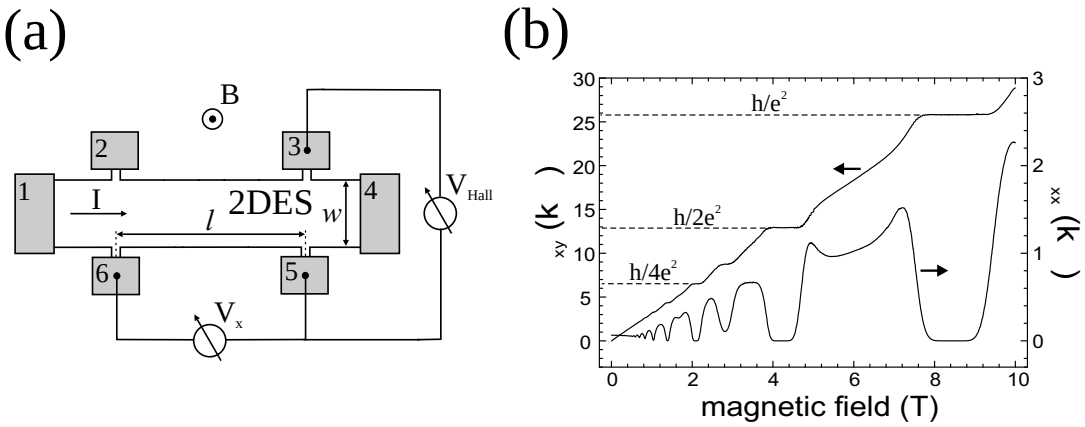

Figure 1.1: The quantum Hall effect. (a) Experimental setup to measure the QHE. The dark surfaces are the ohmic contacts, which are contacted to the 2DES below the surface of the GaAs crystal. The current I is applied between main contacts 1 and 4, and the voltages V_x and V_{Hall} are measured as a function of perpendicular magnetic field. (b) At certain magnetic field values the Hall resistivity ρ_{xy}=V_{Hall}/I has plateaus, and the longitudinal resistivity ρ_{xx}=$(V_x/I)/(w/l)$ vanishes.

like electron density, electron mobility, but also the sample temperature and the electrical current through the 2DES were found to be important for the formation of the quantum Hall (QH) plateaus. When the temperature is increased, ρ_{xx} increases smoothly and ρ_{xy} deviates from the plateau values. On the other hand the current dependence is more abrupt. If the sample current exceeds a certain limit, a sudden breakdown of the QHE is observed. At this critical value the longitudinal resistance ρ_{xx} increases abruptly by several orders of magnitude.

The breakdown of the QHE attracted attention both in basic research and metrology. In the basic research the breakdown is important for the basic understanding of the QHE. In the metrology it is important because of being the critical limit of high precision measurements for the determination of the resistance standard. For high precision measurements, the sample current should be as high as possible but not exceeding the critical limit, so that the QH conditions are held.

Most of the theories on the breakdown of the QHE can explain only certain aspects of the breakdown, failing to conclusively explain the full variety of the experimental observations. Such a complete conclusive theory which provides a detailed understanding of microscopic processes of the breakdown of the QHE is still missing. A detailed survey of the breakdown of the quantum Hall effect can be found in the review article of Nachtwei [10], which includes almost all the developments in this research field until 1999.

The QHE breakdown is in principle nothing but the excitation of electrons

from the filled Landau levels below the Fermi level, to the empty Landau levels above the Fermi level. If these excited electrons relax to the energy levels below the Fermi level, the QHE is recovered. Experiments with multi-terminal quantum Hall devices have shown, that both the excitation [11, 12, 13, 14] and the relaxation [15] of electrons develop over a certain drifting distance of electrons.

The experiments probing the relaxation of hot electrons back to the QH state [15] yielded a linear relation between the mean free path ℓ_{mfp}, and the average drift length ℓ_D, between two inelastic scattering events. By dividing these drift lengths by the drift velocity, it was possible to estimate the relaxation times τ_{rel} (of the order of nanoseconds), which are just the average drifting times of hot electrons necessary for the relaxation. As ℓ_{mfp} at temperatures below 4 K is dominated by elastic scattering at impurity potentials, the relaxation of excited electrons back to the QHE was attributed to inter-Landau-level transitions, supported by Coulomb scattering at impurities. This explanation of the QHE breakdown was based on the so called "quasi-elastic inter-Landau-level scattering" (QUILLS) model, which was proposed by Eaves *et al.* [16].

In this work we have performed space and time-resolved measurements at the breakdown of the quantum Hall effect, in order to gain a better understanding of the excitation and relaxation of electrons and their effects on the QHE breakdown. **Chapter 2** introduces the fundamentals of a two-dimensional electron system (2DES) in GaAs/AlGaAs heterostructures, which leads to the QHE through the Landau quantization in magnetotransport measurements. A phenomenological description and a summary of the earlier work on the QHE breakdown is included at the end of the chapter. In **Chapter 3** the fabrication of the quantum Hall devices (Hall bars and Corbino devices) and the final preparations before the measurements are described in detail.

In **Chapter 4** the results of space-resolved measurements at the QHE breakdown, which allow to determine typical parameters of the electron relaxation and excitation, are presented. To simulate the excitation measurements, a phenomenological model is introduced, which combines the idea of avalanche-like electron heating [13, 17] with the idea of quasi-elastic inter-Landau-level scattering [16]. In **Chapter 5** time-resolved breakdown measurements at Hall bar devices are presented, and a simple drift model is introduced, which qualitatively explains the presented results. In **Chapter 6** the results of time-resolved breakdown measurements at Corbino devices are introduced. The main motivation behind this was to investigate the possible existence of edge effects at the QHE breakdown. At the end of the chapter there is a section on relaxation measurements at Corbino devices. **Chapter 7** presents a simple relaxation oscillator based on a quantum Hall device with Corbino geometry near the breakdown of the QHE, and finally **Chapter 8** summarizes the presented work.

2 Fundamentals of the Quantum Hall Effect

For the observation of the quantum Hall effect (QHE), a two-dimensional electron system (2DES) at very low temperatures and high magnetic fields is absolutely necessary. This chapter introduces the fundamentals of such a system in GaAs/AlGaAs heterostructures, which leads to the QHE through the Landau quantization in magnetotransport measurements. A phenomenological description of the breakdown of the QHE is included at the end of this chapter.

2.1 Two-dimensional electron systems at the GaAs/AlGaAs heterostructures

For the observation of the QHE the realization of a two-dimensional electron system (2DES) is absolutely necessary. By two-dimensional it is meant that the electrons have well separated quantized energy levels for one spatial dimension, but are quasi-free to move on the other two spatial dimensions. 2DES can be observed in many material systems like in layer compounds [18], intercalated graphite [19], thin films [20], on the surface of liquid Helium [21], at semiconductor-oxide interfaces [22], and in semiconductor heterostructures [23] (for a review on electronic properties of 2D systems see [24]).

The most famous example of a semiconductor-oxide interface is the Si-SiO_2 interface, the core of the silicon MOSFET (**M**etal **O**xide **S**emiconductor **F**ield **E**ffect **T**ransistor), on which the QHE was originally discovered [1]. The Si-MOSFET works like a capacitor with an aluminium or poly-Si-electrode on one side, a p-type silicon on the other side, and a SiO_2 insulator between them [25]. By the application of a positive gate voltage, electrons in the silicon are attracted towards the gate contact. Because of the existence of the insulating layer they are trapped in the so called inversion layer at the Si-SiO_2 interface.

On the other hand, the most famous example of a semiconductor heterostructure is the GaAs/AlGaAs heterostructure, the core of the GaAs-MODFET (**MO**dulation **D**oped **F**ield **E**ffect **T**ransistor), on which the fractional quantum Hall effect (FQHE) was discovered [3]. The working principle of such a

device is very similar to the Si-MOSFETs. The only difference is the way of realization of the 2DES.

Fig. 2.1 shows the typical layer structure of such a heterostructure. By means of molecular beam epitaxy (MBE) a buffer layer is grown on top of an undoped semi-insulating GaAs substrate. The buffer layer is composed of alternating superlattice layers of AlGaAs and GaAs, which helps to define atomically smooth surfaces for the next growth layers. On top of the buffer layer a 1 μm undoped GaAs is grown, followed by a thin undoped AlGaAs layer, which is also called as **spacer**. Above the spacer a silicon doped n-type AlGaAs layer, and finally above that, a thin GaAs cap layer is grown, which is to prevent the wafer from oxidation.

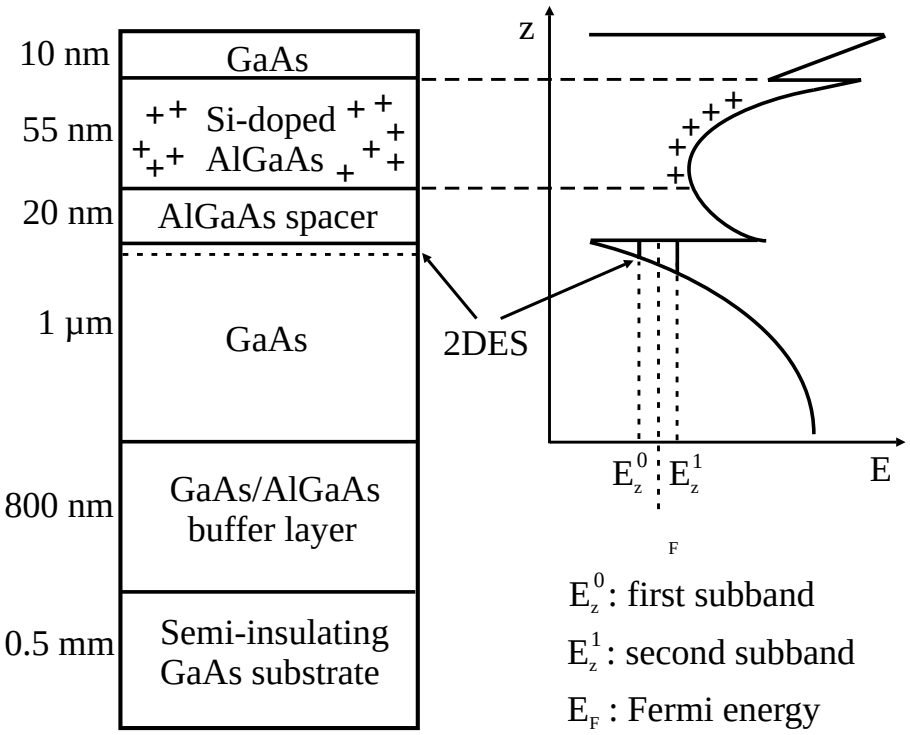

Figure 2.1: A typical modulation doped GaAs/AlGaAs heterostructure and the sketch of its conduction band. The electrons are provided by the silicon donors "+" of the doped AlGaAs layer, and trapped at the potential well in the undoped GaAs. The spacer layer separates the electrons from the donors and therefore decreases the Coulomb interaction between them. This improves the electron mobility of the 2DES.

The two-dimensional electron system develops at the heterojunction between the spacer and the 1 μm thick GaAs layer, by means of electron transfer from the silicon donors of the n-doped AlGaAs through the spacer layer into the GaAs region. The spacer layer therefore separates the electrons in the conduc-

tion band of the GaAs from their positively charged donors. This technique is called **modulation doping**, which results in a drastic reduction of the impurity scattering and therefore in a great increase of the electron mobility.

When the Schrödinger and Poisson equations are solved self-consistently, the corresponding energy band diagram of the structure can be obtained. Such a solution is sketched in Fig. 2.1 for the conduction band of the modulation doped GaAs/AlGaAs heterostructure. At the heterojunction there exits a quasi-triangular potential well, whose effective thickness is comparable or smaller than the de Broglie wavelength of the electrons. The energy of the electrons is quantized and grouped in the energy subbands E_z^i (i=0,1,2,...). At low temperatures (T<4 K) and with small carrier densities only the lowest energy subband is occupied with electrons. As a result, the electrons are strictly confined in this potential well in the z-direction, but are free to move in the xy-plane. The total energy is therefore E_z^0 plus the kinetic energy, such that

$$E = E_z^0 + \frac{\hbar^2(k_x^2 + k_y^2)}{2m^*}, \tag{2.1}$$

where m^* is the effective electron mass and k_x and k_y are the wavevector components in the momentum space. Because of the strong asymmetry of the potential well, the wavefunction of the electrons in the z-direction is mainly localized in GaAs. Therefore m^* can be taken as the effective electron mass in GaAs, which is m^*=$0.066m_0$.

2.2 Density of states of a 2DES without magnetic field

To describe the 2DES system completely, one requires the energies and wavefunctions of all its states, which is clearly an impossible task for anything but the simplest systems. Therefore for many applications the density of states $D(E)$ is adequate, which gives us the information about the distribution of energies. The definition is that $D(E)\delta E$ is the number of states of the system whose energies lie in the range E to $E + \delta E$ [26].

The wavefunction satisfying the free-particle Schrödinger equation and the periodicity condition in a rectangular 2DES with lengths L_x and L_y is of the form of a travelling plane wave:

$$\Psi_k(x, y) = \frac{1}{\sqrt{L_x L_y}} e^{(ik_x x + ik_y y)}, \tag{2.2}$$

where, k_x and k_y are integer multiples of $2\pi/L_x$ and $2\pi/L_y$ respectively. In the ground state the electrons of the 2DES may be represented as points inside a

circle in the k-space. The energy at the edge of the circle is called the Fermi energy E_F, such that

$$E_F = \frac{\hbar^2 k_F^2}{2m^*}, \tag{2.3}$$

where k_F is the magnitude of the wavevectors at the Fermi circle. There is only one point in the area element $(2\pi/L_x)(2\pi/L_y)$ of the k-space [27]. If we divide

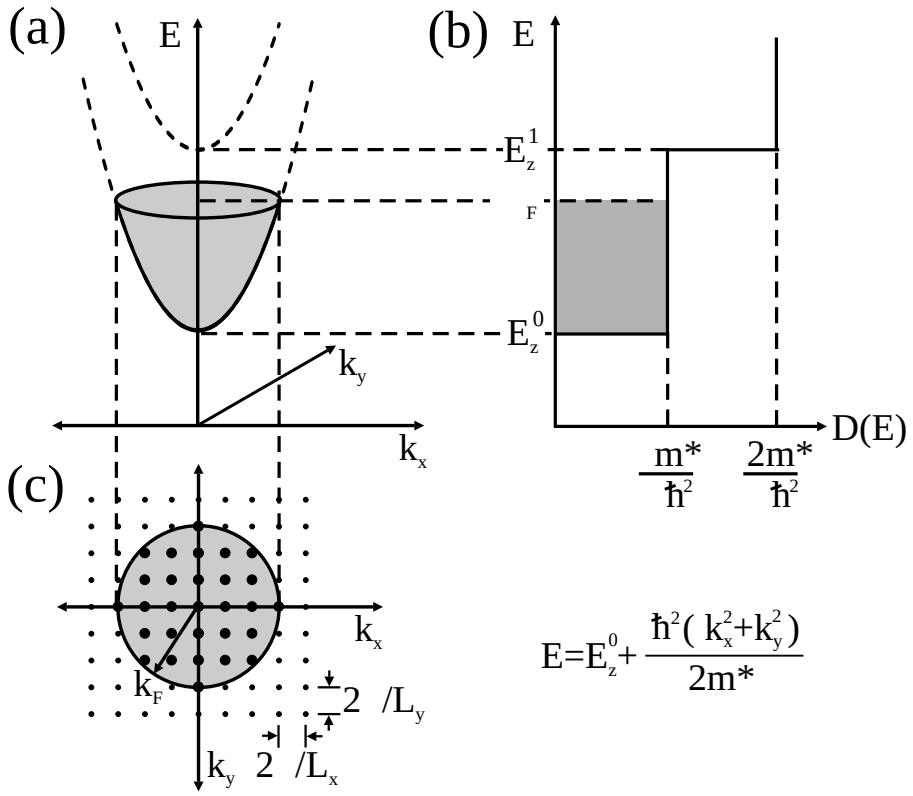

Figure 2.2: Density of states of a 2DES without magnetic field. (a) The total energy of the 2DES is the first subband energy E_z^0, which is a constant, plus the kinetic energy, which is a paraboloid. (b) The corresponding density of states, where the Fermi energy lies between the first and second subbands as it is the case in our samples. (c) The points in the Fermi circle represent the two-dimensional electrons in the k-space.

the total area of the Fermi circle by the area element and multiply this by 2, we obtain the number of electrons N,

$$N = 2\frac{\pi k_F^2}{(2\pi/L_x)(2\pi/L_y)} = \frac{Ak_F^2}{2\pi}, \tag{2.4}$$

where the factor 2 comes from the allowed spin-up and spin-down states, and $A{=}L_xL_y$ is the area of the 2DES. Since $n_s{=}N/A$ is the electron concentration of the 2DES, from Eq. 2.4 the Fermi wavevector becomes $k_F = \sqrt{2\pi n_s}$. If we put this in Eq. 2.3 we have a relation between the Fermi energy and the electron concentration:

$$E_F = \frac{\pi\hbar^2 n_s}{m^*}. \tag{2.5}$$

To obtain the energy distribution or the density of states we differentiate n_s with respect to E [27]. So from Eq. 2.5 we obtain

$$D(E) = \frac{\delta n_s}{\delta E} = \frac{m^*}{\pi\hbar^2}. \tag{2.6}$$

Therefore for each subband, the density of states is independent of the energy. This is the result of the parabolic dispersion $E \propto k^2$ [28]. If several subbands are occupied, each subband contributes with the same amount, so that we have a step-like behavior in the total density of states as seen in Fig. 2.2. When several subbands are occupied, the electrons can be found on several positions in the z-direction. Due to this, such systems are called **quasi-2DES**.

2.3 Density of states of a 2DES in magnetic field

The application of a uniform magnetic field normal (z-direction) to the plane (xy-plane) of the 2DES leads to a complete quantization of the energy spectrum [29, 30]. If the electron-electron interaction and the spin are neglected, the system can be defined by the magnetic-field-dependent Schrödinger equation

$$\frac{1}{2m^*}(\overrightarrow{p} + e\overrightarrow{A})^2\Psi(x,y) = \epsilon\Psi(x,y). \tag{2.7}$$

The simplest algebra is in Landau gauge, where there is only one component of the vector potential $\overrightarrow{A}$ such that $\overrightarrow{A}{=}(0, Bx, 0)$. In this case, the vector potential does not depend on y, which suggests that the wavefunction should be

$$\Psi(x,y) = \phi(x)\exp(ik_y y). \tag{2.8}$$

On substituting this into Eq. 2.7 and having $p_x^2{=}{-}\hbar^2\delta^2/\delta x^2$ we have the Schrödinger equation for a one-dimensional harmonic oscillator

$$\left(-\frac{\hbar^2}{2m^*}\frac{\delta^2}{\delta x^2} + \frac{m^*\omega_c^2}{2}(x + k_y\ell_B^2)^2\right)\phi(x) = E\phi(x), \tag{2.9}$$

with the **cyclotron frequency** $\omega_c = eB/m^*$ as in the classical case. The length scale ℓ_B is called the **magnetic length** given by

$$\ell_B = \sqrt{\frac{\hbar}{eB}}, \tag{2.10}$$

depending only on the magnetic field B. A typical value for magnetic length is $\ell_B \approx 26$ nm for B=1 T.

If Eq. 2.9 is solved, we obtain the following energies and the wavefunctions for the electron motion in the xy-plane

$$E_n = (n + 1/2)\hbar\omega_c, \tag{2.11}$$

$$\Psi(x, y) \propto H_n\left(\frac{x + k_y\ell_B^2}{\ell_B}\right) \exp\left(-\frac{(x + k_y\ell_B^2)^2}{2\ell_B^2}\right) \exp(ik_y y), \tag{2.12}$$

where n=0,1,2,..., and H_n are the Hermite polynomials. The energy depends only on n, but not on k_y, so that the states having the same n but different k_y are degenerate. The density of states collapses from the constant value (Fig. 2.2 (b)) to a series of δ-functions called the **Landau levels** at energies given by Eq. 2.11. But due to scattering the degeneracy is resolved, and the density of states looks like as in Fig. 2.3 (b). In parallel to this, the Fermi sphere rearranges into Landau tubes, and their cross sections with the paraboloid result in Landau circles [28] as shown in Fig. 2.3 (a) and (c).

The successive circles correspond to successive values of the quantum number n. In Fig. 2.3 (c) the area between successive circles is

$$\pi\Delta(k^2) = 2\pi k(\Delta k) = (2\pi m^*/\hbar^2)\Delta E = 2\pi m^*\omega_c/\hbar = 2\pi eB/\hbar. \tag{2.13}$$

If we divide this area by the area element in the k-space, we find N_L the number of electrons per Landau level [27]

$$N_L = 2\frac{(2\pi eB/\hbar)}{(2\pi/L_x)(2\pi/L_y)} = 2\frac{L_x L_y eB}{h}. \tag{2.14}$$

The factor 2 comes from the spin-up and spin-down states, when the spin splitting is not taken into account. Therefore the number of electrons in each Landau level per unit area is

$$n_L = 2\frac{eB}{h} \quad \text{(without spin splitting)}. \tag{2.15}$$

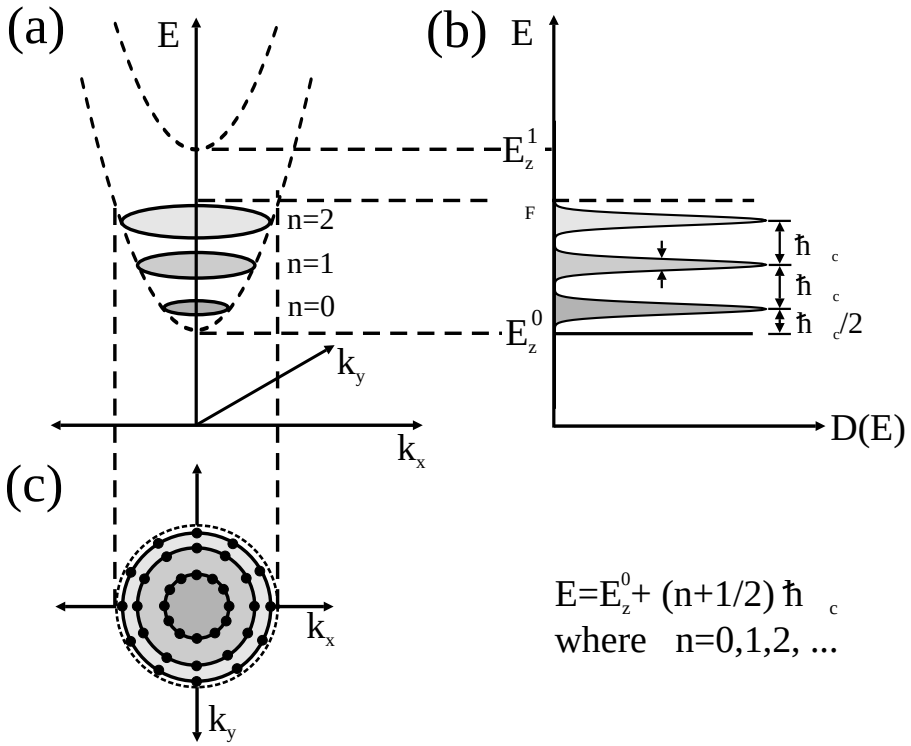

Figure 2.3: Density of states of a 2DES in magnetic field. (a) In a magnetic field the Fermi sphere rearranges into Landau tubes, and their cross sections with the paraboloid give the Landau circles. (b) Because of scattering the Landau levels look like Gaussians instead of δ-functions. (c) Each Landau circle has the same amount of electron orbitals.

This is also called the **degeneracy factor** of the Landau levels, which is independent of any semiconductor parameters like effective mass, or of the quantum number n.

The sharp δ-functions can appear only in an ideal system, where electrons are never scattered. It is more realistic to assume that an electron typically survives for a finite time τ_i between scattering events. Then the energy broadening of a level can be defined as the standard deviation or the full width at half-maximum $\Gamma{=}\hbar/\tau_i$. The precise shape of the Landau levels remains controversial [26] but the most common assumption is a Gaussian profile. As shown in Fig. 2.3 (b) the Landau levels become distinct when $\hbar\omega_c > \Gamma$.

Up to this point the electron spin has not been considered except for the fact that it doubles the number of states available. This is not acceptable in a magnetic field, because due to the magnetic moment of the spin the configurations spin-up and spin-down states have different energies. Therefore the full energy spectrum becomes

$$E_n = (n + 1/2)\hbar\omega_c \pm \frac{1}{2} g^* \mu_B B, \tag{2.16}$$

where $\pm\frac{1}{2}$ is the quantum number of the electron spin and $\mu_B = e\hbar/2m_0$ is the Bohr magneton. The factor g^* is the **effective Landé factor**, which may take quite different values in a solid because of the band structure, particularly because of the spin-orbit coupling. For bulk GaAs it is $g^* \approx -0.44$, but $g^* \approx +0.4$ for $Al_{0.3}Ga_{0.7}As$ and the value lies between these in the $GaAs/Al_{0.3}Ga_{0.7}As$ heterostructure [26].

As it is seen from the second term of Eq. 2.16, the energy difference between the spin-up and spin-down levels depends linearly on the magnetic field. Typically at low magnetic fields the Landau levels contain both spin states. As the field is increased the levels split partly into two, and they become completely separate at high magnetic fields.

When the spin splitting is taken into account, the degeneracy of a spin split Landau level becomes

$$n_L = \frac{eB}{h} \quad \text{(with spin splitting)}. \tag{2.17}$$

With this we can define the so called **filling factor** ν, which gives the number of filled Landau levels

$$\nu = \frac{n_s}{n_L} = \frac{hn_s}{eB}. \tag{2.18}$$

2.4 Magnetotransport in the classical regime

To characterize the transport properties of a 2DES in uniform perpendicular magnetic fields mostly the Hall bar geometry is used. Such a measurement setup is shown in Fig. 2.4. The dark surfaces represent the ohmic contacts, which are contacted to the 2DES. An electric field E_x applied between the contacts 1 and 4 causes an electric current I to flow in the Hall bar. Between contacts 5 and 6 the longitudinal voltage V_x and between contacts 3 and 5 the Hall voltage V_y are measured, both as a function of the perpendicular magnetic field B.

Immediately after the electric field is applied, the drift velocity of the electrons v is deflected in the y-direction because of the magnetic field. Electrons therefore accumulate on one edge of the Hall bar, and a positive ion excess is established on the opposite edge until the transverse electric force $F_E = -eE_y$ just cancels the Lorentz force F_L due to the magnetic field [27] (see Fig. 2.4).

Let us now formulate these facts mathematically. In a uniform magnetic field $\overrightarrow{B}$ the Lorentz force on an electron is

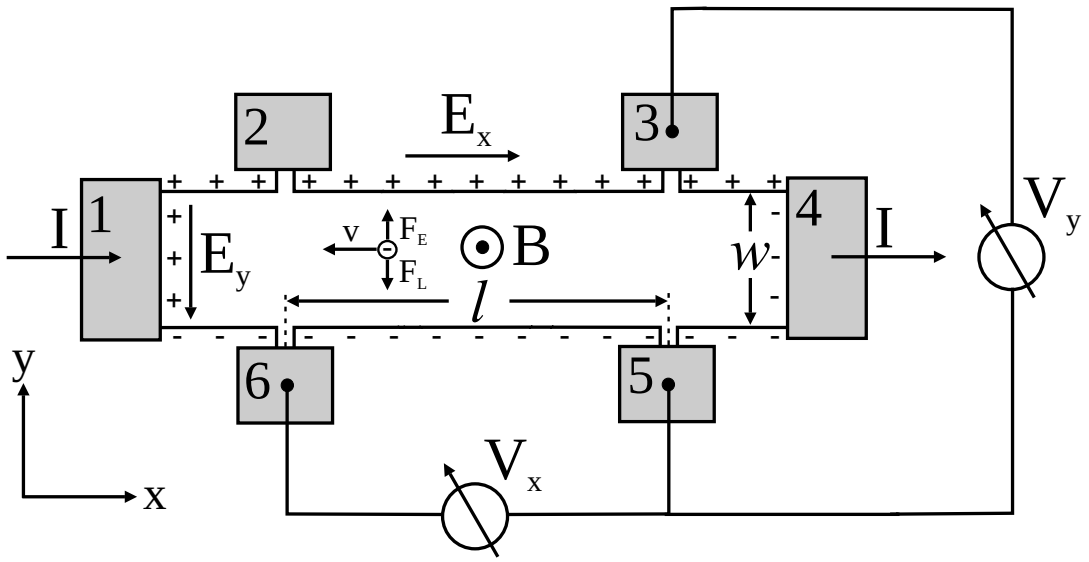

Figure 2.4: Magnetotransport measurement configuration on a Hall bar device. The dark surfaces represent the ohmic contacts, which are contacted to the 2DES. An electric field E_x applied between the contacts 1 and 4 causes an electric current I to flow in the Hall bar. Between contacts 5 and 6 the longitudinal voltage V_x and between contacts 3 and 5 the Hall voltage V_y are measured, both as a function of the perpendicular magnetic field B.

$$\overrightarrow{F_L} = -e(\overrightarrow{E} + \overrightarrow{v} \times \overrightarrow{B}) = m^* \left(\frac{d}{dt} + \frac{1}{\tau} \right) \overrightarrow{v}, \tag{2.19}$$

where $m^* d\overrightarrow{v}/dt$ is the free particle acceleration term, and $m^* \overrightarrow{v}/\tau$ represents the effect of collisions with τ being the scattering time. In the steady state in a static electric field the time derivatives are zero. Therefore the components of the drift velocity becomes

$$v_x = -\frac{e\tau}{m^*} E_x - \omega_c \tau v_y, \tag{2.20}$$

$$v_y = -\frac{e\tau}{m^*} E_y + \omega_c \tau v_x, \tag{2.21}$$

where $\omega_c = eB/m^*$ is the cyclotron frequency. Since current can not flow out of the Hall bar in the y-direction we must have $v_y = 0$. From Eqs. 2.20 and 2.21 this is possible only if there is a transverse electric field (Hall field)

$$E_y = -\frac{eB\tau}{m^*} E_x. \tag{2.22}$$

The potential components can be written as $V_y{=}E_y w$ and $V_x{=}E_x l$ respectively. From the classical **Drude model** [31] the longitudinal electric field is $E_x{=}(m^*/n_s e^2\tau)j_x$, where $j_x{=}I/w$ is the current density. From all these and from Eq. 2.22 we can calculate the longitudinal and transverse resistances R_{xx} and R_{xy}:

$$R_{xx} = \frac{V_x}{I} = \left(\frac{m^*}{n_s e^2 \tau}\right)\frac{l}{w} = \left(\frac{1}{n_s e \mu}\right)\frac{l}{w}, \tag{2.23}$$

$$R_{xy} = -\frac{V_y}{I} = \frac{B}{n_s e}. \tag{2.24}$$

where $\mu{=}e\tau/m^*$ is the **mobility**, a very important parameter that determines the quality of the 2DES. The higher the mobility the smaller is the scattering.

As it is seen from Eqs. 2.23 and 2.24, R_{xx} does not depend on the magnetic field B, and R_{xy}, which is called **the Hall resistance**, increases linearly with magnetic field B. This is the **classical Hall effect**, which was discovered by Edwin Herbert Hall in 1879 on a gold foil [32]. If the quantum Hall effect is observed in magnetotransport measurements the classical Hall effect should also be observed on the same sample, because it is the small magnetic field limit of the QHE. This can be seen in Fig. 2.5, where the classical Hall effect is observed between 0 and 0.4 T. The Hall effect is used as a conventional method to determine the electron concentration n_s and the mobility μ of a 2DES by using the Eqs. 2.23 and 2.24. The quantum Hall device in Fig. 2.5 has an electron concentration of $n_s{=}2.0 \times 10^{11}$ cm^{-2} and a mobility of $\mu{=}4.9 \times 10^5$ cm^2/Vs.

We can also formulate these in the tensor formalism. The transport properties of the 2DES can be described by the two-dimensional conductivity tensor, which relates the electric field $\overrightarrow{E}$ to the current density $\overrightarrow{j}$:

$$\overrightarrow{j} = \hat{\sigma}\overrightarrow{E} = \begin{pmatrix} j_x \\ j_y \end{pmatrix} = \begin{pmatrix} \sigma_{xx} & \sigma_{xy} \\ \sigma_{yx} & \sigma_{yy} \end{pmatrix}\begin{pmatrix} E_x \\ E_y \end{pmatrix}. \tag{2.25}$$

If Eq. 2.21 is put into Eq. 2.20 the velocity components can be written in terms of the electric field components. Using the relation $\overrightarrow{j}{=}{-}en_s\overrightarrow{v}$ the conductivity tensor components can easily be related to the electric field components through the conductivity tensor, which can then be written as

$$\begin{pmatrix} \sigma_{xx} & \sigma_{xy} \\ \sigma_{yx} & \sigma_{yy} \end{pmatrix} = \frac{\sigma_0}{1+(\omega_c\tau)^2}\begin{pmatrix} 1 & -\omega_c\tau \\ \omega_c\tau & 1 \end{pmatrix}, \tag{2.26}$$

where $\sigma_0{=}n_s e^2\tau/m^*$ is the classical **Drude conductivity**. From the above equation it is clear that $\sigma_{xx}{=}\sigma_{yy}$ and $\sigma_{xy}{=}{-}\sigma_{yx}$, which are nothing but the

Onsager relations for an isotropic homogeneous system. The resistivity tensor $\widehat{\rho}$ is the inverse of the conductivity tensor $\widehat{\rho}=\widehat{\sigma}^{-1}$, such that

$$\begin{pmatrix} \rho_{xx} & \rho_{xy} \\ \rho_{yx} & \rho_{yy} \end{pmatrix} = \frac{1}{\sigma_{xx}^2+\sigma_{xy}^2} \begin{pmatrix} \sigma_{xx} & -\sigma_{xy} \\ \sigma_{xy} & \sigma_{xx} \end{pmatrix}. \tag{2.27}$$

As it is seen from Eq. 2.27, the resistivity tensor components obey the same symmetry relations, such that $\rho_{xx}=\rho_{yy}$ and $\rho_{xy}=-\rho_{yx}$. From Eqs. 2.26 and 2.27 we obtain

$$\begin{pmatrix} \rho_{xx} & \rho_{xy} \\ -\rho_{xy} & \sigma_{xx} \end{pmatrix} = \rho_0 \begin{pmatrix} 1 & \omega_c\tau \\ -\omega_c\tau & 1 \end{pmatrix}, \tag{2.28}$$

where $\rho_0=1/\sigma_0$. From this tensor relation we have finally the longitudinal and the transverse resistivity components

$$\rho_{xx} = \frac{m^*}{n_s e^2 \tau} = \frac{1}{n_s e \mu}, \tag{2.29}$$

$$\rho_{xy} = \frac{B}{n_s e}. \tag{2.30}$$

From Eqs. 2.23 and 2.24 it is clear that the Hall resistance is identical with the Hall resistivity, and their longitudinal counterparts are related to each other with the geometry factor w/l

$$\rho_{xy} = R_{xy}, \qquad \rho_{xx} = \left(\frac{w}{l}\right) R_{xx}. \tag{2.31}$$

2.5 Magnetotransport in the quantum regime

Fig. 2.5 shows a typical magnetotransport curve with its three important regimes. At low magnetic fields (up to 0.4 T for this sample) the 2DES behaves classically, and the Hall resistivity increases linearly with magnetic field. This is the classical Hall effect regime. As the magnetic field is increased above 0.4 T, the 2DES leaves the classical regime showing a unique remarkable behavior. The Hall resistivity ρ_{xy} starts deviating from the linearity and the longitudinal resistivity ρ_{xx} develops strong oscillations. This is the **Shubnikov-de Haas (SdH) effect**, which was discovered by Shubnikov and de Haas in 1930 in a Bismuth crystal [33]. As the magnetic field is further increased, the 2DES enters the quantum Hall effect regime, where ρ_{xy} develops plateaus and ρ_{xx} drops to zero. In Fig. 2.5 the regimes are shown with sharp borders between each other, but in reality the transition from one regime to the other is rather smooth.

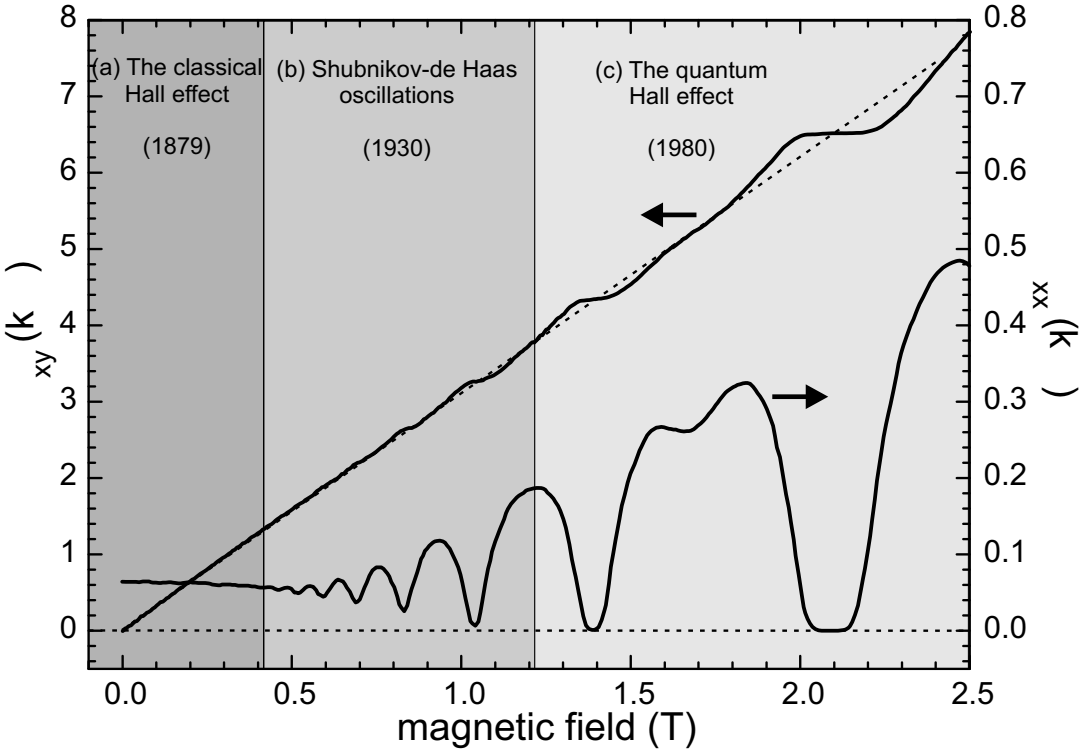

Figure 2.5: A typical magnetotransport curve with three important regimes. (a) The classical regime: at low magnetic fields the classical Hall effect is observed. (b) The regime of SdH-oscillations: at high fields the 2DES starts behaving quantum mechanically, such that both ρ_{xx} and ρ_{xy} develop oscillations. (c) The QHE regime: at higher fields ρ_{xx} goes to zero, and ρ_{xy} develops plateaus.

2.5.1 Shubnikov-de Haas oscillations

To explain the Shubnikov-de Haas oscillations we have to return to the concept of Landau quantization and Landau levels, since this is a pure quantum phenomenon. When the spin splitting is taken into account the density of states in Fig. 2.3 (b) looks like as it is in Fig. 2.6 (a). Electron concentration, magnetic field, temperature, and scattering play here an important role in deciding whether the spin states are split or not. Typically at low magnetic fields, the Landau levels contain both spin states. As the field is increased, the levels split partly into two, and they become completely separate at high magnetic fields.

Let us assume that initially we have the situation as depicted in Fig. 2.6 (a), where the Landau levels with quantum numbers n=0 and n=1 are split but the levels with spin-up and spin-down states are not fully split. From Eq. 2.18 we have here four completely filled Landau levels, so that the filling factor is ν=4. The **Fermi energy** E_F is defined as the energy of the topmost filled orbital at absolute zero (0 K) in the presence of no magnetic field (0 T). Therefore it is a

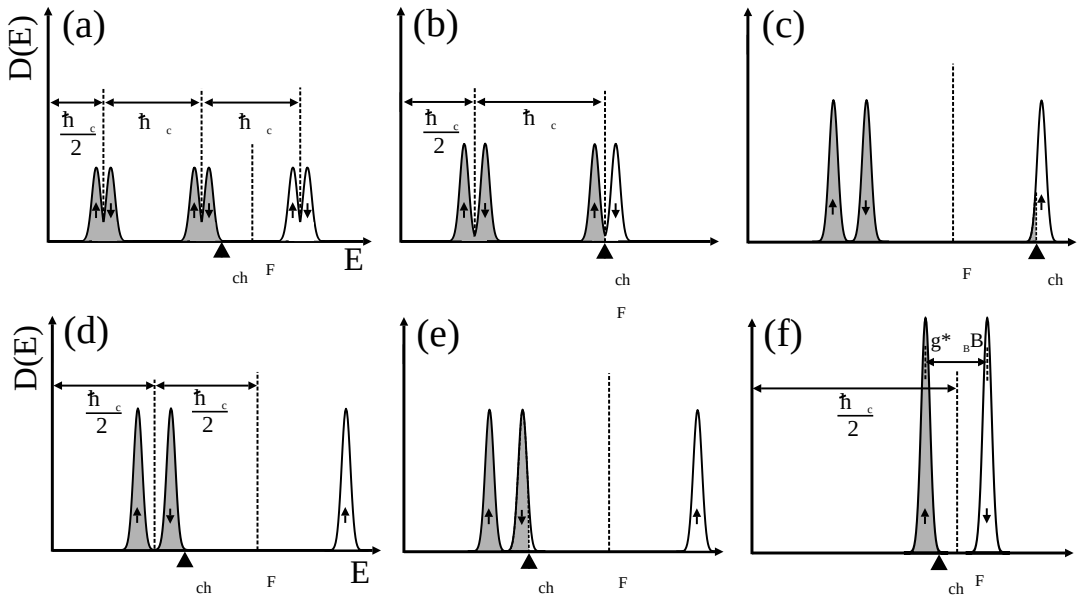

Figure 2.6: The position of the chemical potential as a function of filling factor (or magnetic field). (a) The density of states at ν=4, where the Landau levels with quantum numbers n=0 and n=1 are completely split, but the levels with spin-up and spin-down states are not completely split. (b) As the magnetic field is increased, the separation between the Landau levels grows and so does the number of states that each level holds. (c) μ_{ch} is above the Fermi energy when ν is slightly above ν=2. (d) μ_{ch} jumps below the Fermi energy ν=2, and (e) starts increasing as ν decreases. (f) The magnetic quantum limit is reached when all the electrons have up-spins.

constant on the energy axis E. The **chemical potential** on the other hand, is the energy of the topmost filled orbital at any temperature and magnetic field. Therefore it is not a constant but a function of temperature and magnetic field.

In Fig. 2.6 (a) the chemical potential is below the Fermi energy, because the filling factor ν=4 is an integer, and the Landau levels n=1 and n=2 are completely separated. As the magnetic field is raised, the separation between the Landau levels grows and so does the number of states that each level holds. In Fig. 2.6 (b) we have 3 completely filled Landau levels, and the chemical potential is not below the Fermi energy but equal to it, since the spin states are still not completely separated. Up to ν=2 the chemical potential raises continuously, but at ν=2 it has to jump below the Fermi energy again. This is illustrated in Figs. 2.6 (c) (d) and (e) around and at ν=2. At ν=1 the chemical potential lies below the Fermi energy (unlike at ν=3), because the spin levels are now completely separated. As shown in Fig. 2.6 (f), all of the electrons lying in the lowest Landau level have their spins aligned in the same direction. This is called the **magnetic quantum limit**. Below this limit, where ν<1 the electron-electron

interaction dominates and other interesting physical effects like **the fractional quantum Hall effect** [3] are observed.

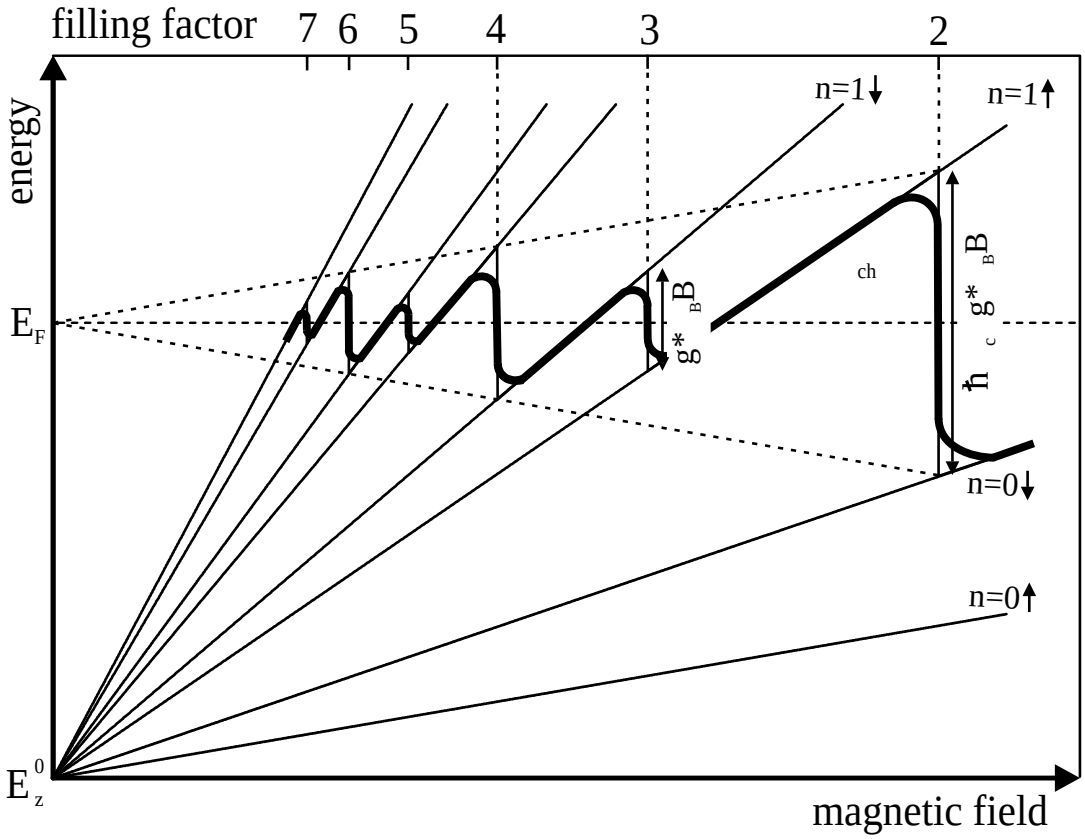

Figure 2.7: The movement of the chemical potential as a function of the magnetic field. For a perfect system with Landau levels in the form of δ-functions, the jumps are abrupt. But in reality they are rounded, because the Landau-levels are broadened due to scattering. At integer filling factors μ_{ch} jumps, and ρ_{xx} has minima.

This movement of the chemical potential is also illustrated in Fig. 2.7 as a function of the magnetic field B. For a perfect system with Landau levels in the form of δ-functions, the jumps are abrupt. But in reality they are rounded, because the Landau-levels are broadened due to scattering. At even integer filling factors the magnitude of the jumps is $\hbar\omega_c - g^*\mu_B B$, and for odd integers it is $g^*\mu_B B$. Using the self consistent Born approximation the scattering time τ_t is $\tau_t \propto 1/D(E_F)^2$, where $D(E_F)$ is the density of states at the Fermi energy [24]. When the Fermi energy lies exactly in between two Landau levels, $D(E_F)$ is minimum and therefore τ_t is maximum. This leads to the minima in the SdH-oscillations at integer filling factors. In other words, when the highest filled Landau level is completely filled, μ_{ch} will be in the gap between the highest occupied and the lowest unoccupied level, such that there will be no empty states available at energies close to μ_{ch}. This is analogous to an insulator, and

the conductivity will be a minimum [34]. From Eq. 2.18 the period of the SdH-oscillations can easily be written as

$$\Delta\left(\frac{1}{B}\right) = \frac{e}{hn_s}. \tag{2.32}$$

If a SdH curve is plotted as a function of inverse magnetic field, and the period of these oscillations is extracted, the electron density of the 2DES can easily be obtained from Eq. 2.32.

2.5.2 The integer quantum Hall effect

As the magnetic field is increased, the minima of the SdH-oscillations tend towards zero. Around the magnetic field values, where the longitudinal resistivity ρ_{xx} goes to zero, the Hall resistivity ρ_{xy} becomes independent of the magnetic field, and a plateau appears. The value of the Hall resistivity ρ_{xy} at such a plateau is the most striking feature of the quantum Hall effect, and can be calculated as follows. When a whole number of Landau levels is fully occupied, the filling factor ν becomes an integer i. Thus from Eq. 2.18 we have

$$n_s = i\frac{eB}{h}. \tag{2.33}$$

If we put this in Eq. 2.30 the Hall resistivity becomes [34]

$$\rho_{xy} = \frac{1}{i}\frac{h}{e^2} = \frac{25812.807}{i}\ \Omega. \tag{2.34}$$

In Fig. 2.8 the quantum Hall plateaus corresponding to the integers i=1,2 and 4 can be seen. The remarkable feature of this effect is that the value of the Hall resistivity is defined by the fundamental constants h and e (the Planck's constant and the charge of an electron) and can be measured with extreme accuracy. The resistance quantum R_K=h/e^2 is named as the **von Klitzing constant** and corresponds to the value 25812.807 Ω. The high accuracy of the quantization, the reproducibility and the independence from the sample geometry have led the QHE in 1990 to be accepted as an international resistance standard. For his discovery, von Klitzing was awarded the Nobel prize in physics in 1985 [2].

Although the simple calculation in Eq. 2.34 predicts the value of the quantized Hall resistance, it gives this value only at one magnetic field point, at which an integer number of Landau levels is completely filled. However, in experiments the plateaus extend over finite widths of magnetic field. To understand this the concept of **disorder** has to be introduced.

We have already shown in Figs. 2.3 and 2.6 that the Landau levels are broadened due to scattering of electrons. These scattering centers (impurities or the

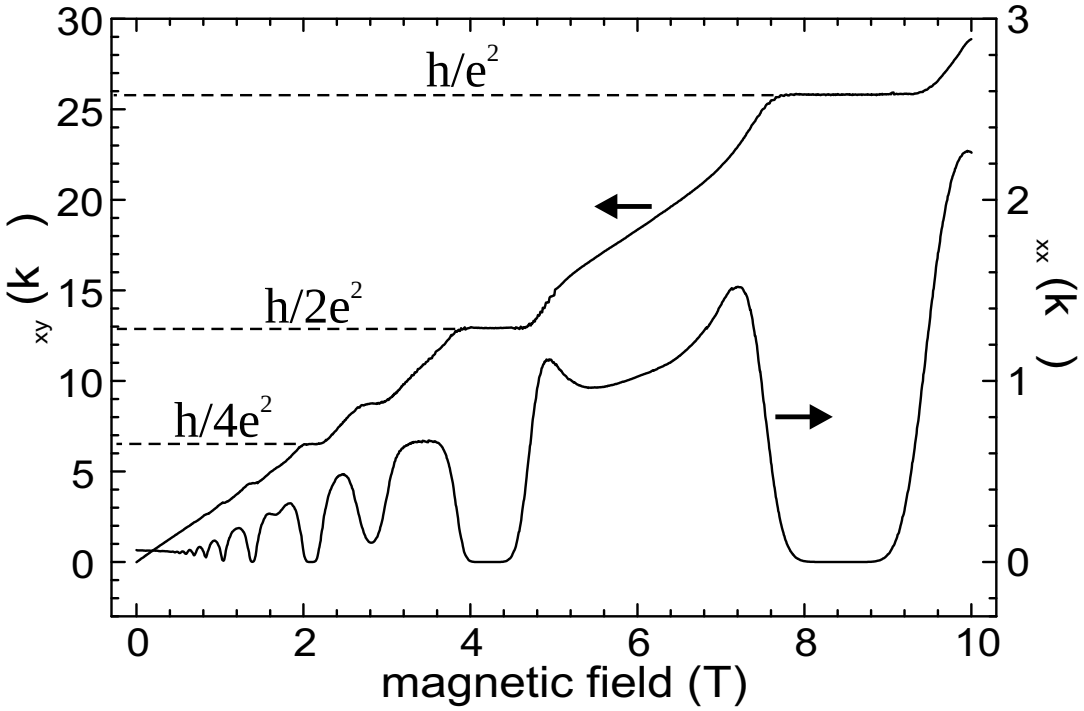

Figure 2.8: The integer quantum Hall effect. At integer filling factors i the Hall resistivity $\rho_{xy}=h/ie^2$ has plateaus and the longitudinal resistivity ρ_{xx} vanishes.

positively charged donors) are distributed randomly throughout the 2DES and cause energy fluctuations at the Landau levels. This means that the energy of a Landau level moves up and down throughout the sample (Fig. 2.9 (a)). The average magnitude of the fluctuations is equal to the broadening of the Landau levels as shown with the connection lines between in Fig. 2.9 (a) and (b).

Let us imagine that at first only one Landau level is filled. As the magnetic field is increased, the degeneracy of the level will decrease and the electrons will start filling the upper level, in the minima of the energy fluctuations. A two-dimensional map of the occupied states may look like as shown in Fig. 2.9 (c). Provided that the field does not change too much, the occupied states will be isolated in islands, which are not connected with each other. Because they are isolated, these electrons will not contribute to the conduction, and the Hall resistivity will remain constant, independent of whether these states are occupied or not. Therefore the Hall plateau can be observed over a range of magnetic field.

Therefore as seen in Fig. 2.9 (b) we have two classes of states: **delocalized states** at the centers of Landau levels, which allow the electrons to move through the 2DES and **localized states**, in the tails of the Landau levels, which are captured in the isolated puddles. When the chemical potential μ_{ch} is in the

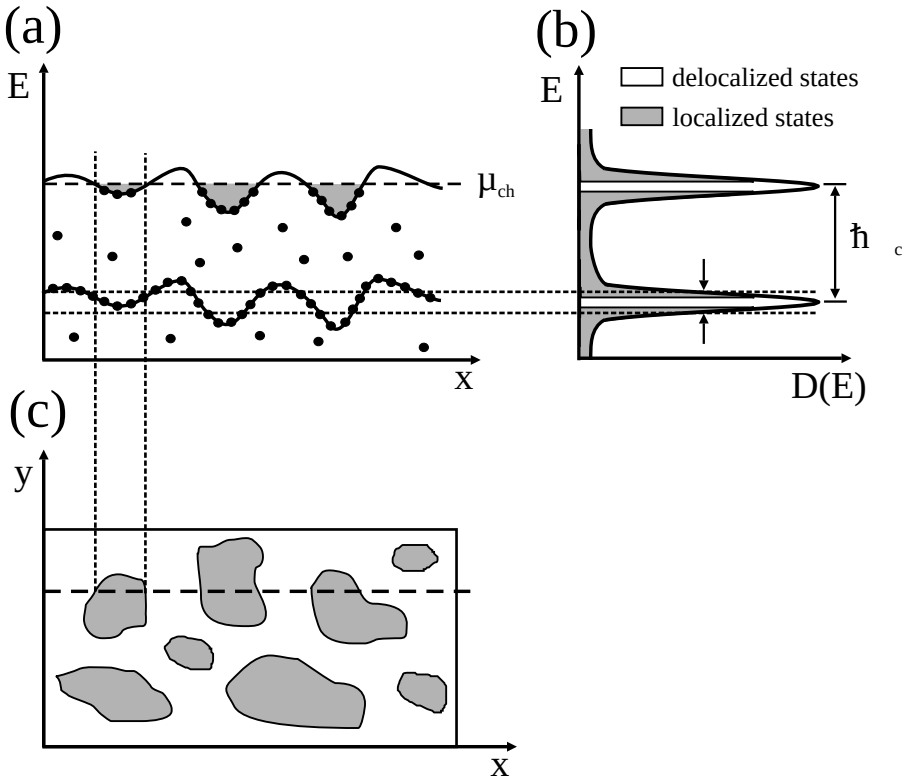

Figure 2.9: Disorder in 2DES (localized and delocalized states). (a) Spatial energy fluctuations caused by disorder. (b) Localized and delocalized states. (c) Metallic "puddles" of electrons.

localized states between the Landau level centers, both the longitudinal resistivity and conductivity become zero σ_{xx}=ρ_{xx}=0, and the Hall resistivity ρ_{xy} is quantized. However, when the chemical potential μ_{ch} is in the extended states, close to the Landau level centers, both σ_{xx} and ρ_{xx} are finite, and ρ_{xy} is not quantized.

2.6 The electrical breakdown of the QHE

Since the quantum Hall effect is observed at liquid helium temperatures, an adequate increase in temperature definitely causes the breakdown of the effect. However, the temperature limit of the QHE is not the subject of this work. Here, only the electrical breakdown of the quantum Hall effect will be discussed.

When the sample current is increased, the quantum Hall plateaus and the regions of ρ_{xx}=0 shrink [8, 35]. This shrinking can be observed in Fig. 2.10 (a) at filling factor ν=2, when the current is increased from 5 μA to 50 μA for this sample. The quantum Hall effect breaks down, if the current exceeds a critical value. When this happens, the quantum Hall plateaus disappear simultaneously,

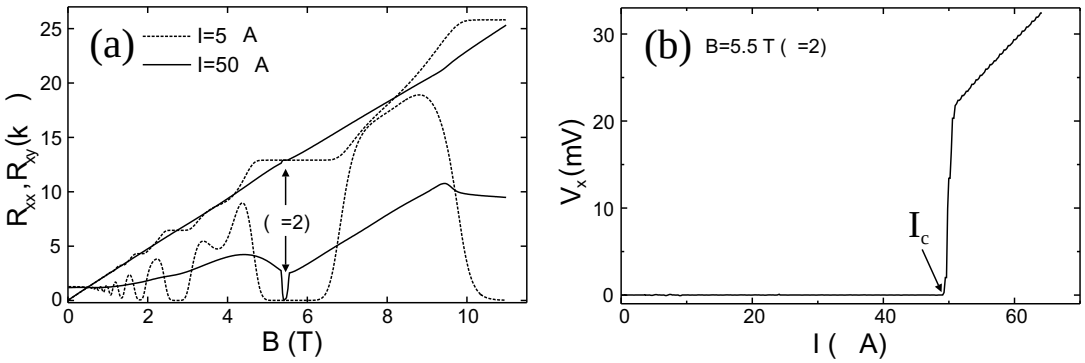

Figure 2.10: The electrical breakdown of the quantum Hall effect. (a) The quantum Hall effect breaks down, if the current exceeds a critical value. When this happens the quantum Hall plateaus disappear and at the corresponding magnetic field values the ρ_{xx} has finite values ($\rho_{xx}\neq 0$). (b) The breakdown behavior can also be observed in the current-voltage (I-V) characteristics of the QH devices. At the critical current I_c the longitudinal voltage V_x increases by several orders of magnitude.

and at the corresponding magnetic field values the ρ_{xx} has finite values ($\rho_{xx}\neq 0$). This can also be seen in Fig. 2.10 (a) at filling factors ν=1, 4 and 6. The critical current is a function of filling factor, and the breakdown has the tendency to start first at higher filling factors. This is due to the lower energy difference between neighboring Landau levels. For GaAs/AlGaAs heterostructures this energy difference has a maximum at ν=2, therefore the critical current at ν=2 is also a maximum, as it is clearly seen in Fig. 2.10 (a). While the QHE breaks down at filling factors ν=1, 4 and 6, it still exists at ν=2 for a sample current of 50 μA.

This breakdown behavior can also be observed in the current-voltage (I-V) characteristics of the QH devices as shown in Fig. 2.10 (b) for ν=2. When the sample current exceeds the critical current I_c, a sudden breakdown of the QHE is observed. At this critical value the longitudinal voltage V_x (or the longitudinal resistance ρ_{xx}) increases by several orders of magnitude.

Without addressing the physical process, which is responsible for the QHE breakdown, it is possible to show phenomenologically how the breakdown occurs. In the ideal case of the QHE regime (for the temperature and current approaching zero), the tensor components can be written as

$$\rho_{xx} = 0, \qquad \rho_{xy} = h/ie^2. \tag{2.35}$$

Since the current flows only in the x-direction, the y-component of the current density is always zero j_y=0, and the tensor relation $\overrightarrow{E}=\widehat{\rho}\,\overrightarrow{j}$ becomes

$$\begin{pmatrix} E_x \\ E_y \end{pmatrix} = \begin{pmatrix} 0 & \frac{h}{ie^2} \\ -\frac{h}{ie^2} & 0 \end{pmatrix} \begin{pmatrix} j_x \\ 0 \end{pmatrix} = \begin{pmatrix} 0 \\ -\frac{h}{ie^2} j_x \end{pmatrix}. \tag{2.36}$$

The Hall angle Θ is defined as the angle between the Hall field and the current direction. As shown in Fig. 2.11 (a), in the QHE regime the electric Hall field is perpendicular to the current flow direction, and therefore the interior power dissipation per unit area is zero:

$$\frac{\delta P_i}{\delta A} = \overrightarrow{j} \cdot \overrightarrow{E} = \begin{pmatrix} j_x \\ 0 \end{pmatrix} \cdot \begin{pmatrix} 0 \\ -\frac{h}{ie^2} j_x \end{pmatrix} = 0. \tag{2.37}$$

Thus, the current flows without dissipation in the interior of the 2DES when the Hall angle is Θ=90°. Because of the voltage distribution, shown with "−" and "+" signs, the equipotential lines have to cross through the diagonally opposite corners of the Hall bar. At these corners the Hall angle is $\Theta \neq 90°$, so that dissipation takes place. Because of the dissipation, these points are called **hot spots**, which were also experimentally observed by Klaß *et al.* [36]. Therefore the total power dissipation becomes $P_t = \rho_{xy} I^2$, which takes place only at the hot spots.

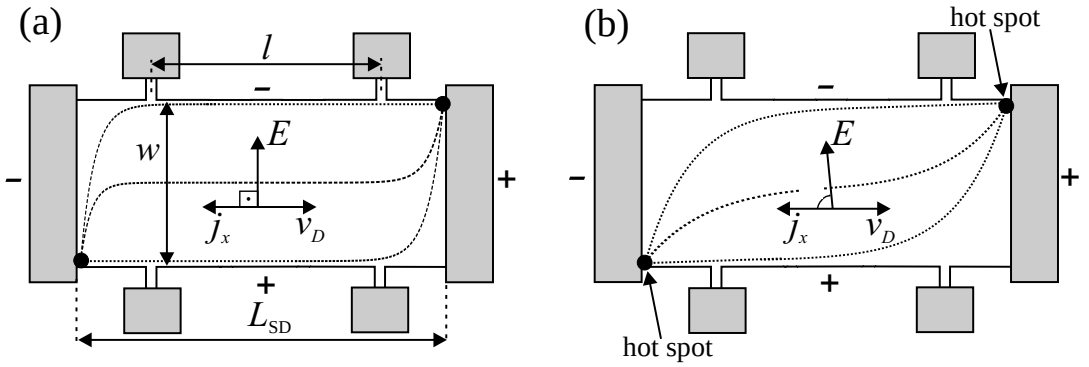

Figure 2.11: The Hall angle at the quantum Hall effect and breakdown conditions. (a) (QHE: $j_x < j_c$) The Hall angle Θ is 90°, therefore no dissipation occurs in the sample interior but only near the contacts. (b) (Breakdown: $j_x > j_c$) The Hall angle is $\Theta < 90°$, therefore dissipation occurs in the sample interior.

Above the critical current, there is a finite component of the electric field, E_x in the current flow direction. As a result, the Hall angle differs from 90° also in the interior of the sample, as shown in Fig. 2.11 (b). The tensor relation in Eq. 2.36 becomes

$$\begin{pmatrix} E_x \\ E_y \end{pmatrix} = \begin{pmatrix} \rho_{xx} & \rho_{xy} \\ -\rho_{xy} & \rho_{xx} \end{pmatrix} \begin{pmatrix} j_x \\ 0 \end{pmatrix} = \begin{pmatrix} \rho_{xx} j_x \\ -\rho_{xy} j_x \end{pmatrix}. \tag{2.38}$$

The dissipated power per unit area in the sample interior is then

$$\frac{\delta P_i}{\delta A} = \overrightarrow{j} \cdot \overrightarrow{E} = \rho_{xx} j_x^2. \tag{2.39}$$

This internal dissipation over the entire sample can then be estimated as $P_i{=}\rho_{xx} j_x^2 L_{SD} w{=}\rho_{xx} I^2 L_{SD}/w$ and the total dissipation power becomes

$$P_t = (\rho_{xx} L_{SD}/w + \rho_{xy}) I^2. \tag{2.40}$$

including the dissipation near the contacts. There is no ρ_{xx} term in the latter term, because $\rho_{xx} \ll \rho_{xy}$ holds even for the breakdown. The relative dissipation of the sample interior is defined as

$$\frac{P_i}{P_t} = \left(\frac{\rho_{xy}}{\rho_{xx}} \frac{w}{L_{SD}} + 1 \right)^{-1} \approx \frac{\rho_{xx}}{\rho_{xy}} \frac{L_{SD}}{w}. \tag{2.41}$$

Eq. 2.41 is a useful experimental criterion for the definition of the breakdown in Hall bars [10]. There exists a **pre-breakdown regime** in which ρ_{xx} increases slightly before the QHE breaks down [9]. The threshold value ρ_{xx}^{th} should be chosen well above the pre-breakdown values, typically of the order of 1-10 Ω.

2.7 An overview of the earlier work on QHE breakdown

The physical limits of the quantum Hall effect were investigated [8, 9], shortly after the discovery of the effect. For the formation of the quantum Hall (QH) plateaus, electron density, electron mobility, sample temperature and the electrical current through the 2DES were found to be important. The breakdown of the QHE naturally attracted attention in basic research because of its relevance for the understanding of the principal basics of the QHE. Moreover, because of its precisely defined values of the Hall resistance, the QHE has been used since 1990 as the resistance standard. For high precision measurements of this resistance standard, the sample current should be as high as possible but well below the critical limit. Because of these aspects, scientists either from National Bureaus of Standards [8, 37, 38] or from basic research institutions [9, 39, 40, 41] were involved in the early activities of investigating the breakdown of the QHE.

Up to now different mechanisms and models were proposed to explain the breakdown of the quantum Hall effect. These were for example based on the effective reduction of the Landau gap by the electric Hall field [42], intra-Landau-level transitions [43], inter-Landau-level transitions [16], electron heating [9, 17, 41],

electron-phonon interactions [17, 41, 43], potential fluctuations [12], or on the formation of compressible and incompressible islands [44].

The distribution of current flow and equipotential lines in the quantum Hall regime and their importance for the breakdown of the quantum Hall effect have been a subject of discussion. In 1988, Büttiker [45] combined earlier considerations of the electrical resistance on the basis of transmission and reflection of electrons [46, 47] and of the appearance of edge states at the boundary of a 2DES [48, 49, 50] providing an explanation of the QHE. Due to the confinement potential at the boundary, the Landau levels depart from their original values and cross the Fermi level near the boundary. At these crossing points, one dimensional edge states develop, which are capable of carrying current. If the difference of the chemical potentials $\Delta\mu_{ch}$ of the edge states is small ($\Delta\mu_{ch}<\hbar\omega_c$), and there is no backscattering between the opposite edges, the net current carried by a single edge state is

$$I_l = \frac{e}{h}\Delta\mu_{ch}, \tag{2.42}$$

being independent of the Landau level number l. Therefore, the total current for i completely filled Landau levels is carried by i edge channels. The value of the current is determined by the difference of the chemical potential $\Delta\mu_{ch}=eV_H$:

$$I = i\frac{e^2}{h}V_H, \tag{2.43}$$

which directly gives the quantized Hall resistance $\rho_{xy}=V_H/I=h/ie^2$. However for Hall voltages exceeding the Landau gap $V_H>\hbar\omega_c$, the tunneling into empty states of the next higher Landau levels is enhanced, and the current starts to spread into the two-dimensional bulk, causing the breakdown of the QHE. This was observed in experiments at certain samples with a narrow constriction (w=4 μm) of the current channel [51] and with a pronounced inhomogeneity [52, 53]. However, such an edge-induced breakdown at $V_H=\hbar\omega_c$ in the second QH plateau at B=4 T would correspond to critical current values of about 0.5 μA, which are by orders of magnitude smaller than the measured critical current values of wide Hall bar samples (w=200 μm) with typical sample parameters ($n_s=2\times10^{11}$ cm^{-2}, $\mu_H=5\times10^5$ cm^2/Vs). Therefore, the explanation of the breakdown of the QHE on the basis of edge channel transport in Büttiker's sense cannot be in general applicable.

To clarify the current distribution experimentally, electrical [54, 55], electro-optical [56, 57], inductive [58, 59] and scanning probe techniques [60, 61, 62] have been used. Regarding all these measurements, there has been no experimental evidence yet for an edge current dominated charge transport in the QH regime for higher currents. Therefore a dominant role of edge states for the breakdown of the QHE cannot be expected either [10].

Another serious objection against the edge current related breakdown is the proportionality of the breakdown current with the sample width. For samples with lower and medium electron mobilities, the breakdown current was found to scale with the sample width from some ten to hundreds of micrometers [63, 64, 65]. A similar linearity was observed for samples with antidot lattices in the submicrometer range [66, 67]. Therefore, at currents close to the breakdown, a homogeneous current distribution exists for samples with lower electron mobility (in the presence of a sufficient degree of disorder). In contrast, in samples with higher electron mobilities, a sublinear increase of the breakdown current with the sample width was reported [68, 69], indicating an inhomogeneous current distribution at the QHE breakdown. Further, it was shown experimentally that an inhomogeneous current flow leads to a breakdown in distinct local areas of the 2DES [70]. From all these experiments it is shown that the two-dimensional bulk currents dominate in the QHE breakdown, at least for the nonballistic transport in macroscopic samples. Moreover, it is also understood that the degree of disorder and the homogeneity of the current distribution are crucial for the breakdown of the QHE.

Besides this width dependence, an interesting length dependence of the QHE breakdown was also reported [12, 71]. The authors have discovered that the sharp increase of the longitudinal resistance at I_c observed in long devices is markedly suppressed with decreasing device length. Moreover, it was found that even when a current exceeding I_c is passed through a Hall bar device, the longitudinal voltage V_x along the 2DES remains practically vanishing, in a region close to an electron-injecting corner, but grows to exhibit well defined breakdown characteristics as the distance from the electron injecting corner increases [13]. All of these results were explained by an avalanche heating model of the electrons, reaching a steady state after a certain drifting distance. In other words, the electrons must travel a macroscopic distance to accomplish the breakdown phenomenon. However neither this electron heating model nor other proposed models are able to provide a complete microscopic picture of the breakdown. Therefore further work on the QHE breakdown is necessary.

2.8 Summary

The quantum Hall effect (QHE) is observed in two-dimensional electron systems (2DES) at liquid helium temperatures and in high magnetic fields. The two-dimensional electron systems in this work are realized at the heterojunctions of GaAs/AlGaAs heterostructures, by means of electron transfer from the silicon donors of the n-doped AlGaAs into the undoped GaAs region. The transport properties of such a 2DES are mostly characterized by using the Hall bar geometry, in which the longitudinal resistivity ρ_{xx} and the transversal (Hall) resistivity ρ_{xy} can be simultaneously measured.

The application of a uniform magnetic field normal to the plane of the 2DES leads to the Landau quantization of the energy spectrum. As a result of this quantization, Landau levels are formed, and Shubnikov-de Haas oscillations are observed in the ρ_{xx} measurements. The minima of these oscillations, which correspond to a fully occupied number of Landau levels (integer filling factor), tend to decrease and become zero ρ_{xx}=0, as the magnetic field is increased. The vanishing of the longitudinal resistivity occurs in a certain range of magnetic field values around these integer filling factors, corresponding to a dissipationless current flow. At these magnetic field values, the Hall resistivity ρ_{xy} exhibits plateaus with the quantized values $\rho_{xy}=h/ie^2$, where h is the Planck constant, e is the elementary electron charge, and i is the integer filling factor. This is the quantized Hall effect, which was discovered by von Klitzing in 1980.

When the sample current is increased above the critical value, the quantum Hall effect breaks down, such that the quantum Hall plateaus disappear, and the longitudinal resistivity increases by several orders of magnitude. So far many mechanisms and models were proposed to explain the breakdown of the quantum Hall effect, but a complete conclusive theory is still missing. Therefore, further work is necessary in particular for the detailed understanding of the microscopic processes in the QHE breakdown.

3 Device Fabrication and Final Preparations

In this chapter, the fabrication of quantum Hall devices (Hall bars and Corbino devices) and the final preparations before the measurements are described in detail.

3.1 Device fabrication

For the device processing a **clean room environment** is absolutely necessary, in which yellow light is generally preferred, because the photoresists are least sensitive to this wavelength. The crucial steps like photolithography, etching and deposition are all performed in clean rooms, where good filtering techniques and protective clothing on personnel are strictly required. The quantum Hall devices in this work were fabricated in the clean room facilities of "Max-Planck-Institut (MPI) für Festkörperforschung" in Stuttgart, and "Physikalisch-Technische Bundesanstalt (PTB)" in Braunschweig.

3.1.1 Device structure

All of the devices in this work were fabricated from modulation doped GaAs/AlGaAs wafers, with different electron concentrations and mobilities (see Table 3.1). The wafers were grown by Karl Eberl and coworkers in the MBE (Molecular Beam Epitaxy) facilities of Max-Planck-Institute in Stuttgart. In the previous chapter in Fig. 2.1 we have already shown the typical layer structure of such a wafer. On top of an undoped semi-insulating GaAs substrate a buffer layer is grown. The buffer layer, which is composed of alternating superlattice layers of AlGaAs and GaAs, helps to define atomically smooth surfaces for the next growth layers, and for segregation of undesired impurities. A 1 μm undoped GaAs layer is grown on top of the buffer layer, followed by a thin undoped AlGaAs layer (spacer). Finally an n-type AlGaAs layer and a thin GaAs cap layer are grown above the spacer. The cap layer prevents the wafer from oxidation.

	n_s (cm^{-2})	μ_H (cm^2/Vs)
Wafer W_1	2.0×10^{11}	9×10^5
Wafer W_2	2.0×10^{11}	5×10^5
Wafer W_3	2.7×10^{11}	1×10^5
Wafer W_4	2.75×10^{11}	1.3×10^5
Wafer W_5	2.1×10^{11}	2.4×10^5

Table 3.1: Electron density and Hall mobility of the fabricated wafers. The parameters were determined from the magnetotransport measurements at 1.5 K.

The quantum Hall devices were fabricated in three different geometries: Hall bars (Fig. 3.1 (a)), Hall bars with constriction (Fig. 3.1 (b)) and Corbino devices (Fig. 3.1 (c)). In Fig. 3.1 (d) the cross section of such a quantum Hall device is shown schematically. First a mesa layer is defined on the GaAs/AlGaAs wafer by chemical etching of the undesired regions. For the isolation of the devices the GaAs/AlGaAs heterostructure should be etched well below the 2DES, so that there is no electrical contact between the devices through the 2DES. Then Au, Ge, and Ni are evaporated on this mesa surface with defined patterns. Finally by the help of an annealing process, the deposited metal semiconductor mixture is forced to diffuse into the GaAs, contacting the 2DES. With this step the metal contacts become ohmic, and they are used either to apply current through the source and drain contacts of the device or to measure the potential drops V_x and V_{Hall} between the potential probe contacts. In the following sections the process steps will be described in detail.

3.1.2 Photolithography

The MBE grown wafers are in the form of circular plates of about 5 cm in diameter and 0.5 mm in thickness. Before starting the device processing they are cut into small rectangular pieces by means of a special machine, which is called the scriber. Cleaning operations are performed on these small samples before all major process steps throughout the device processing. Plasma etching, acids, bases, and solvent cleaning are the basic cleaning methods. In our processes we performed primarily **2-solvent cleaning** by aceton, and isopropyl alcohol (iso-propanol). The wafer samples were first rinsed with aceton and then with iso-propanol. If the contamination is stubborn, ultrasound can be very helpful. After 2-solvent cleaning the samples were purged with nitrogen gas and finally kept on the hot plate at 120°C for about 5 minutes. This step is called **dehydration baking**, which helps to improve adhesion of photoresist by creating more mechanical-chemical bonding on the surface.

Virtually all patterning techniques used in semiconductor processing employ energy sensitive chemical substances called **photoresists**. These substances are

applied to the wafer as thin film coatings, and then by means of photomasks they are selectively exposed to an energy pattern (light, electrons, etc.). After the exposure of energy, the resist film is subjected to a development process that selectively removes either the exposed or the unexposed parts. The remaining pattern can then be replicated in other materials, using techniques such as etching, deposition, etc. This technique of transferring geometric shapes from the mask to the surface of the wafer, is called lithography. If the exposure of the resist film is accomplished by using a light source, then it is called **photolithography**. The resolution is limited by the diffraction effect, which increases with the square root of the wavelength and with the gap between the mask and the wafer [72].

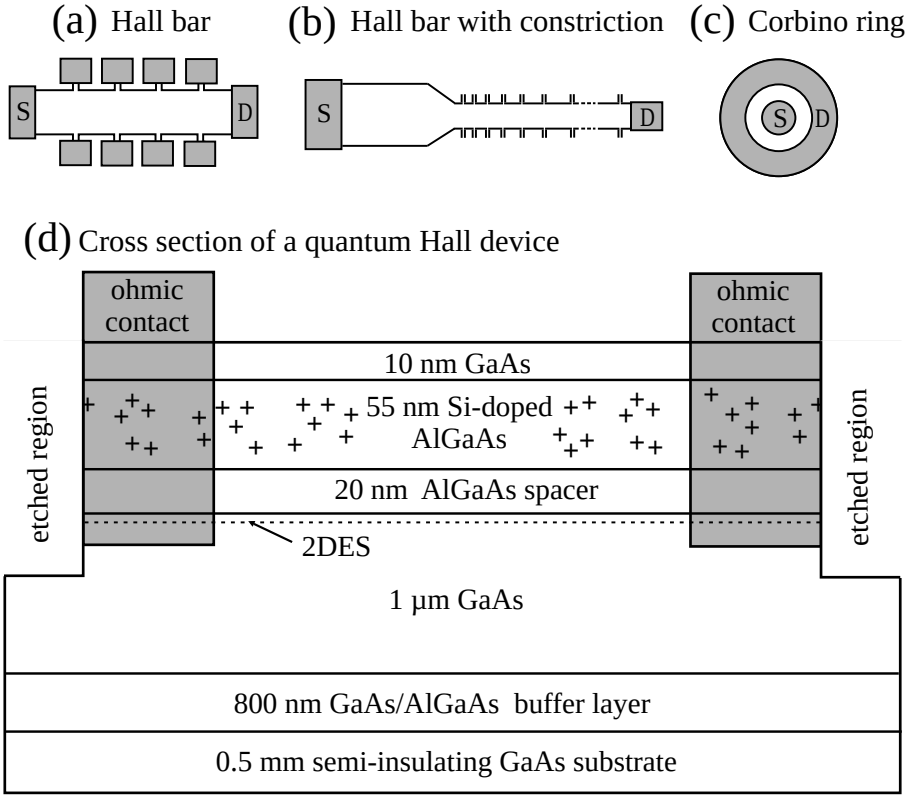

Figure 3.1: Top view of the fabricated QH devices and the cross section of an exemplary QH device. (a) Top view of a Hall bar. S and D represent the source and drain contacts. (b) Top view of a Hall bar with constriction. (c) Top view of a Corbino ring. (d) The cross section of a quantum Hall device. An isolated mesa layer is defined on a modulation doped GaAs/AlGaAs wafer by etching the undesired regions chemically well below the 2DES. On the mesa structure Au, Ge and Ni are evaporated. With an annealing process, this metal semiconductor mixture is forced to diffuse into the GaAs contacting the 2DES.

Photoresist coating is done by a special machine by means of spinning. The thickness of the resist coating is crucial depending on the process and can be adjusted by the spinning speed and the viscosity of the resist. In MPI we have used a positive Shipley S1805 photoresist without dilution. With a spinning speed of about 4500 r.p.m. (rotations per minute) and with a spinning time of 30 seconds, uniform resist layers with a thickness of 0.5 μm were obtained (Fig. 3.2 (a)). After the resist is spun, it must be baked for good adhesion with the GaAs surface. This process is also called **soft-baking**, which hardens the resist by removing the solvent and water remaining in the film after spinning. For the Shipley photoresist S1805 we have done the soft-baking on a hot plate at 90°C for 2 minutes. However, in the clean room of PTB, a Hoechst AZ5214E photoresist was used. It was spun with 3250 r.p.m. for 25 seconds, which gave a thickness of about 2 μm. The soft-baking was done at 90°C for 3 minutes.

After spinning and soft-baking of the photoresist, the samples were ready for the exposure of desired patterns. These patterns are achieved by photomasks and a photolithography machine, which uses high intensity ultraviolet light. The main idea behind the **exposure** is to change the chemical structure of the photoresist from one form to another, for example from polar to non-polar or from polymer to monomer structure (Fig. 3.2 (b)). Photomasks are glass or quartz plates, on which the desired patterns are defined in thin films of chromium, iron oxide, or silicon. On our photomasks we had mainly two layers, defining the steps of mesa isolation and ohmic contacts. Both in MPI and PTB we have done the exposure with Karl Süss machines for about 7-9 seconds.

After the exposure, the samples are placed in a developer solution for the **development** of the exposed photoresist, in which the patterns are revealed for the actual device processing steps (Fig. 3.2 (c)). For the Shipley resist, we used the Shipley Microposit 351 developer, which was diluted with deionized water up to 25%. It took 30 seconds for the development. For the Hoechst resist we used the AZ developer, which was diluted with deionized water up to 50%. The development time was 25 seconds.

The photoresist protects the wafer areas that it covers. However the bare parts, which are not covered by the photoresist, are unprotected. Therefore in the following process steps, the resist coated areas of the wafers are not affected from the applications like etching or deposition. This is the purpose and summary of the photolithography.

3.1.3 Mesa isolation

Isolation means restricting the electrically conductive portion of the wafer to specific parts of its surface area, so that electric current is restricted only in this active region. Isolation also permits the individual operation of designed device patterns. There are two basic ways for device isolation: ion implantation and

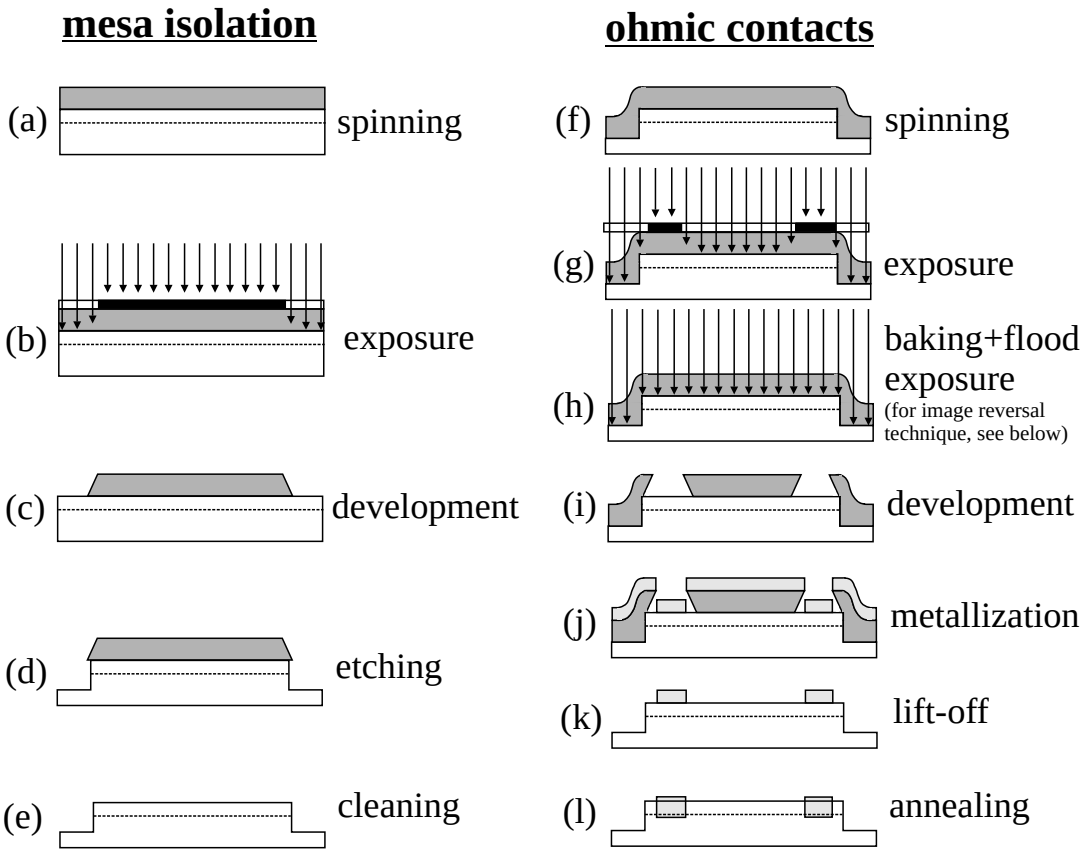

Figure 3.2: The fabrication steps for mesa isolation and ohmic contacts. The dashed line represents the 2DES.

mesa etching (Fig. 3.2 (d)).

In mesa etching techniques, it is required to transfer a mask pattern exactly onto the material surface. The etching process should therefore be anisotropic and ideally proceed only downwards into the material. If the etching is isotropic, a large undercut occurs and the mask pattern is not exactly transferred [72].

Wet etching is widely used because of its simplicity. The mesa structures formed are usually a few tenths of a micron smaller than the original mask pattern size, due to the etching across the surface. This should be taken into account in the mask design. We etched the mesas by liquid based etchants, which proceed at the surface of the GaAs through some ordered chemical reactions. First, the surface is oxidized, then the oxides (Ga_2O, Ga_2O_3, As_2O_3, As_2O_5) are dissolved, removing the Ga and As atoms from the surface. In the literature there are various wet etching solutions, with various etching characteristics [72].

In MPI for example we have used a solution of H_2O:H_2O_2:H_2SO_4=1000:8:1 as the etchant. At room temperature and with a slow stirring, the etch rate was about 55 nm/min. In PTB on the other hand, we have used CH_3CH_2OH:H_2O_2:H_3PO_4=3:1:1, which provided an etch rate of about

1900 nm/min. This is very fast compared to the previous etchant, causing some risks in controlling the etch depth. But for our purposes we did not observe any difference in the device performance. After the etching, the samples were cleaned with deionized water, and purged with a nitrogen gun. The remaining photoresist, which protected the mesa was removed by the standard 2-solvent cleaning procedure (Fig. 3.2 (e)).

3.1.4 Ohmic contacts

An **ohmic contact** is a metal-semiconductor contact, which has a very small contact resistance compared to the bulk or spreading resistance of the semiconductor. The contact is said to be ohmic when the ratio of the potential drop V across the contact versus the current I flowing through the contact is linear with a constant R_c=V/I. The primary requirements of ohmic contacts are a low specific contact resistance, an insignificant contact metal diffusion into the semiconductor both laterally and vertically, and reliability under severe environmental and bias stress conditions [73]. In ohmic contacts, basically thermionic emission over a Schottky barrier and tunneling through it are the main mechanisms that govern the current flow. For a detailed theoretical treatment, one can see the reviews by Rideout [74] and Piotrowska [75].

The ohmic contacts in this work are realized with the deposition of thin films of Au, Ge, and Ni, followed by lift-off and annealing. We first performed a photolithography step on the mesa, by exposing and developing the photoresist areas, where the contacts should be placed (Fig. 3.2 (f), (g), (h), (i)). This exposure step is done with alignment, by matching the alignment marks of the substrate and the photomask. The samples were then loaded into the metallization chamber, which is used for **deposition** of thin films by means of evaporation (Fig. 3.2 (j)). The samples were mounted on a holder facing down towards tungsten evaporation boats, where the thin film materials are heated and evaporated. The metallization chamber is then pumped down to about 1×10^{-6} mbar.

Eutectic Ni/AuGe (composition of 88% Au and 12% Ge) is the most commonly used contact material for n-GaAs [76, 77], which we used in the PTB cleanroom. We have evaporated 5 nm Ni, 200 nm AuGe, and 25 nm Ni. On the other hand in the MPI cleanroom we have evaporated 100 nm Au, 50 nm Ge, and 40 nm Ni. Both methods provided us ohmic contacts with good quality.

After the deposition process, the samples are removed from the metallization chamber and placed in an acetone bath. The application of acetone removes the photoresist, by causing the resist to dissolve. Meanwhile the metallic layer on top of the dissolved resist peels off from the surface, revealing the final pattern of the ohmic contacts. This method is called the **lift-off** (Fig. 3.2 (k)). For a successful lift-off, the photoresist walls should have negative slope walls

(undercut) causing discontinuities in the deposited thin film. This was achieved by two different methods:

1) Chlorobenzene application: After exposure and before development the samples were put in chlorobenzene (C_6H_5Cl) solution for 3 minutes, and subsequently baked at 85°C for 10 minutes. This application produces a thin , hard crust on the photoresist surface, which develops more slowly than the inner parts. The resulting undercut helps the lift-off. For the chlorobenzene application positive resist is used.

2) Image reversal technique: For this method a negative photoresist (AZ5214 from Hoechst) and a negative (image reversal) photomask are used. After the usual exposure (Fig. 3.2 (g)) with the image reversal photomask, the samples were baked at 120°C for 2 minutes. Then they were exposed without a photomask for 30 seconds (flood exposure, Fig. 3.2 (h)). When the samples are put in the developer solution, the areas, which are exposed two times, stay on the sample, but the areas, which are exposed only once, dissolve. The resulting pattern is the positive pattern (not image reversal) and the resist has an undercut.

Annealing is very crucial for obtaining good ohmic contacts (Fig. 3.2 (l)). It helps the diffusion of the metal-semiconductor film into the GaAs crystal, and reduces the metal thickness decreasing the serial resistance of the devices. In the literature [72], annealing temperatures vary between 400°C and 500°C. In our processes we performed the annealing at 430°C for about 1 minute, in forming gas (H_2:N_2=5%:95%) atmosphere to avoid oxidation. During annealing, Ge atoms, which are the donor impurities for GaAs, diffuse into the substrate and heavily dope the GaAs layer. Meanwhile the Ga atoms diffuse to the surface and form a metallic AuGa alloy [73, 75]. This two-way diffusion reduces the width of the Schottky barrier between the metallic AuGa alloy and the GaAs forming the ohmic contact. As the final step 10 nm Cr followed by 90 nm Au can be deposited for better bonding purposes.

It should be also kept in mind that if a clean GaAs is exposed to open air, in four days a thin (3 nm) oxide-carbon layer is formed at the surface, adversely affecting the contact quality [78].

3.2 Final preparations before the measurements

For the magnetotransport measurements it is necessary to place the fabricated QH devices in magnetcryostats, where magnetic field is applied at liquid helium temperatures. For this purpose chip carriers, sample holders and cryostats are needed. Moreover, in the experiments several measurement devices were controlled by a measurement automation, which also performed the data acquisition. These final steps before the measurements will be explained in the

following sections.

3.2.1 Bonding

Once a QH device has been attached to a chip carrier, **wire bonding** is one method of making the connection between the ohmic contacts and chip carrier pins. Aluminum and gold are typically used as the bonding wire. Bonding has three basic methods: ultrasonic, thermocompression and thermosonic. The ultrasonic method uses ultrasonic energy, whereas the thermocompression method uses heat and pressure to attach the wire. In the thermosonic method, the wire is feeded through a capillary, an electrical spark melts the wire tip to form a ball, and then the capillary moves downward to touch the bonding pad. After pressure the capillary moves upward, releases some wire and then it is positioned to make the second bond.

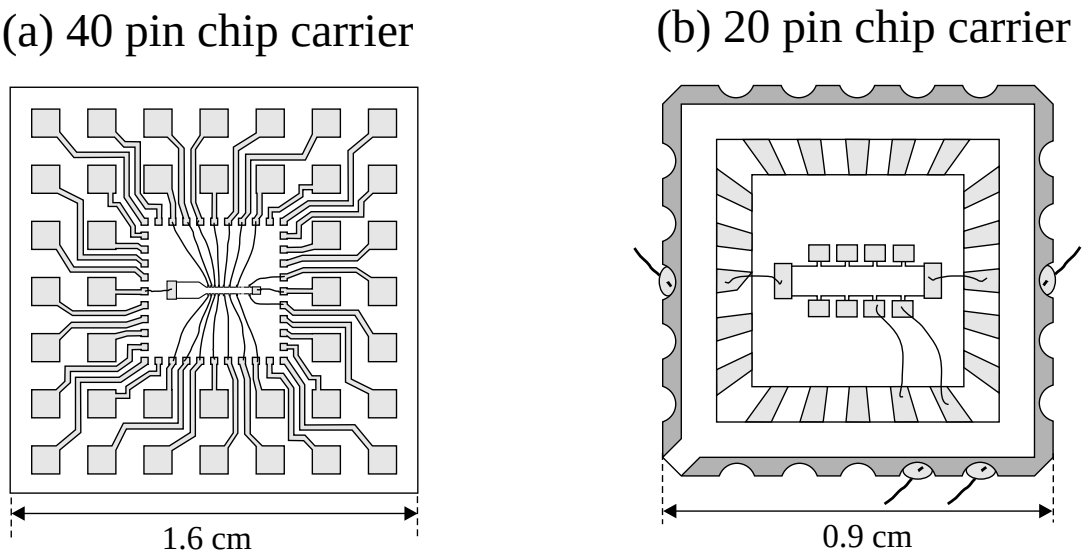

Figure 3.3: Scheme of 40-pin and 20-pin chip carriers. (a) 40-pin chip carrier specially designed for the space-resolved QHE breakdown measurements. Aluminum or gold wires were bonded between the ohmic contacts and the pins of the chip carrier. Connections between the chip pins and the sample holder were realized by means of a corresponding chip socket. (b) Conventional 20-pin chip carrier (from Kyocera Fineceramics) used for the time-resolved breakdown measurements. Additional wires were soldered from the side contacts of the chip carrier to the pins of the sample holder. The size of the Hall bars is exaggerated.

When the device fabrication was finished, the QH devices were glued on chip carriers with photoresist, and were fixed by baking the photoresist at 120°C for 5 minutes. For the space-resolved measurements we have fabricated specially

designed chip carriers with 40 electrical pins (Fig. 3.3 (a)). The fabrication was done on gold coated ceramic plates, by standard photolithography and wet etching. All of the 40 pins were necessary (19 pairs of side contacts for the spatial resolution and 2 for the source and drain contacts of the Hall bars) for the measurements. For the time-resolved measurements we have used conventional 20-pin chip carriers (Fig. 3.3 (b)) from Kyocera Fineceramics. In the figure, the light gray scale represents the gold contacts.

The electrical connections between the ohmic contacts of the QH devices and the pins of the chip carriers were achieved by using standard **wedge bonders** with gold or aluminum wires. In the facilities of MPI a bonder from Kulicke and Soffa Industries was used. For the space-resolved measurements we have bonded all the 40 contacts with gold wires. In Fig. 3.3(a), for simplicity only part of the 40 bonds are shown.

In the clean room facilities of PTB, the West Bond model has been set up as an ultrasonic 45-degree wedge bonder. The ultrasonic energy attaches a thin aluminum wire at room temperature. The wire is clamped and threaded diagonally under the bonding wedge, allowing independent feeding action but requiring front-to-back bonding direction. The tool is guided manually by the operator using hand/eye reference to bond targets and elevations. As schematically shown in Fig. 3.3 (b) for the time-resolved measurements we did not need all the 20 pins. We have bonded only 4 pins for the Hall bars, and 2 for the Corbino devices (only for source and drain contacts).

3.2.2 Sample holders

After bonding, the chip carriers were connected to specially designed sample holders. A sample holder serves as an information bridge between the measurement devices (voltmeter, pulse generator, current/voltage source) at room temperature and the QH sample at liquid helium temperature. It consists of a measuring head with electrical (or optical) sockets, and a long rod with electrical (or optical) cables.

The sample holders for both space and time-resolved measurements were designed and realized in MPI-Stuttgart. The sample holder for the space-resolved measurements had a specially designed 40-pin chip carrier socket at its cold side, together with an Allen Bradley resistor to monitor the temperature. In the rod there were 40 cables, which began from the socket connections and reached the measuring head. With a 40-pin connector on the measuring head and a corresponding cable, the 40 contacts of the QH samples were connected to a scanner (Keithley 7001 Switch System), which was programmed to select and scan the successive pairs of potential contacts of the QH devices.

In the sample holder for the time-resolved measurements, there were two 10-pin

cables, beginning from two 10-pin Fischer Connectors on the measuring head, and ending at the chip carrier place. Instead of using a chip carrier socket, we have realized the connections by soldering cables from the side contacts of the chip carrier to the pins of the sample holder (as shown in Fig. 3.3 (b)). At the chip carrier position there was a Lakeshore diode sensor (DT-471) for monitoring the sample temperature. For the application of steep electric pulses we have implemented in the sample holder a semi-rigid coaxial cable (Handy-Form II from Spektrum Elektrotechnik GmbH) with a 50 Ω impedance. The external conductor of the coaxial cable was from aluminum and it was tin-plated for soldering purposes. The cut-off frequency of the cable was 36 GHz, and it had a capacity of 98 pF/m.

3.2.3 Cryostats

The sample holders with the QH Hall devices were designed to fit into **liquid Helium cryostats** (Oxford Instruments) with superconductive solenoid magnets [79]. As seen from the scheme in Fig. 3.4, the magnet-cryostats have three main parts: a helium bath, a variable temperature insert, and a superconductive magnet coil.

The **helium bath** has two major purposes. First, it supplies helium to the variable temperature insert through a pickup tube, which has an adjustable orifice called the needle valve. Second, it keeps the magnet permanently at 4.2 K, below its critical temperature, T_c, so that the magnet is superconductive. This is absolutely necessary for the magnet operation. In order to maintain the thermal isolation of the liquid helium, high vacuum should be maintained within the outer vacuum case (OVC) of the cryostat. We have pumped the OVC with a turbo molecular pump, backed by a rotary pump, down to about 1×10^{-5} mbar. It is recommended that the cryostat is always pumped overnight before use. Excess helium evaporating from the helium bath is collected by a recovery system, where the helium gas can be liquefied again.

The experiments were performed in the **variable temperature insert (VTI)**, whose temperature could be varied over the range of typically 1.5 K to 300 K, using liquid helium coolant drawn from the helium bath [79]. The sample holders were placed in the VTI, in such a way that the samples were positioned exactly at the center of the magnet. The liquid helium was drawn from the main reservoir through the needle valve, which was adjusted from the top of the cryostat and was used to control or stop the helium flow into the VTI. Temperatures below 4.2 K were obtained by reducing the vapor pressure of static helium liquid, which was collected in the VTI. We have performed almost all the experiments by pumping the VTI by a rotary pump down to about 5 mbar, which corresponds to a temperature of 1.5 K. For a better thermal isolation, we have also pumped the inner vacuum case (IVC) between the helium bath and the VTI, down to

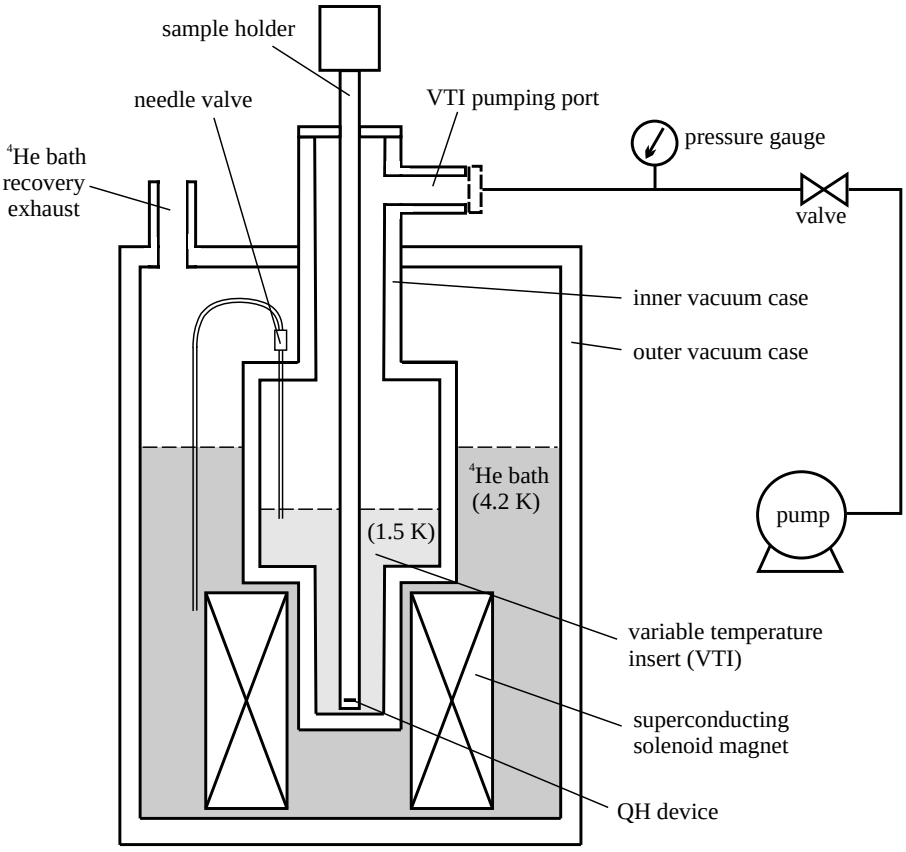

Figure 3.4: Scheme of a magnet-cryostat with sample holder. Liquid helium is drawn into the variable temperature insert (VTI), by slightly opening the needle valve and pumping down the VTI. By regulating the pressure and the needle valve, the temperature of the sample can be varied down to 1.5 K.

about 1×10^{-5} mbar.

The **superconductive magnet** consisted of two coils, each containing a number of concentric solenoid sections together with compensating coils [79]. Each section of the outer coil was wound from niobium titanium (NbTi) filaments surrounded by a stabilizing matrix of copper. The inner coil was made from niobium tin (Nb_3Sn). Protection resistors and diodes were provided for all magnet sections, restricting the development of potentially high voltages in the event of a magnet quench. A magnet quench is the rapid conversion from the superconductive to the normal resistive state.

3.2.4 Measurement devices

The electrical devices to operate the magnet-cryostat were common in all experiments: a power supply (Oxford IPS$^{120-10}$ max. current 120 A, max. voltage

10 V) to run the superconductive magnet, a digital voltmeter (Keithley 196) to read the magnetic field, a helium level meter (Oxford ILM^{210}) to detect the helium level in helium bath, and other periphery apparatus to detect and control the pressure and temperature of the VTI, to operate the needle valve, etc.

For the space-resolved measurements we have used a current voltage source (Keithley 236) for applying current through source and drain contacts, a digital voltmeter (Keithley 2182) to measure the potential drop across the side contact pairs, and a scanner (Keithley 7001 Switch System) to successively select and scan the side contact pairs.

For the time-resolved measurements we have used rectangular pulse generators (Hewlett Packard 8131A with pulse widths: 500 ps to 99.9 ms, transition times: $<$ 200 ps and Hewlett Packard 8133A with pulse widths: 150 ps to 10.5 ns, transition times: $<$ 100 ps), digital voltmeters (Keithley 2000, Keithley 2182), a current voltage source (Keithley 236) and digitizing oscilloscopes (Tektronix TDS820 up to 6 GHz and TDS220 up to 100 MHz).

3.2.5 Measurement automation

We have controlled the measurement devices and performed the data acquisition by LabVIEW software from National Instruments. LabVIEW is a graphical programming language that uses icons instead of lines of text to create applications [80]. In LabVIEW one builds a user interface, known as the front panel, by using a set of tools and objects. The code is then added by the programmer using graphical representations of functions to control the front panel objects. The block diagram that contains this code resembles a flowchart. LabVIEW is fully integrated for communication with hardware such as GPIB and plug-in data acquisition devices.

LabVIEW programs are called virtual instruments (or VIs), because their appearance and operation imitate physical instruments, such as oscilloscopes and multimeters [80]. Every VI uses functions that manipulate input from the user interface or other sources and display the information or move it to other files or other computers. For space and time-resolved measurements, for SdH oscillations and for I-V characterizations, we have developed a number of programs, which automated the device control and data acquisition.

When the device fabrication and final preparations were completed, we have performed the space and time-resolved measurements. The experimental setup and results of these experiments are discussed in the following chapters in detail.

3.3 Summary

For the space and time-resolved breakdown measurements, various quantum Hall devices were fabricated from MBE grown modulation doped GaAs/AlGaAs wafers. For the device fabrication, a special patterning technique (photolithography) was used, in which a light sensitive chemical substance (photoresist) was selectively exposed to light through a patterned glass plate (photomask). Before starting the device fabrication, first the photomasks, which contained the device structures with transparent and nontransparent patterns, were designed and produced.

The fabrication started by cutting small rectangular pieces from the wafers, followed by a 2-solvent cleaning procedure. After cleaning, photoresist was spun on the wafer pieces, and ultraviolet light was exposed on them through the mesa-photomask. After developing the samples in a developer solution, the desired mesa patterns were replicated on the samples. By placing the samples in a chemical solution, the mesa patterns were etched for the device isolation. After etching, the same procedure was repeated with the photomask for the ohmic contacts, and an ohmic contact material was evaporated on the samples. After lift-off and annealing steps the device fabrication was completed.

After the device fabrication, the samples were placed on special chip carriers, and the ohmic contacts were bonded to the chip carrier pins. The chip carriers were then placed in sample holders, and the sample holders were placed in magneto-cryoststats, where we performed our experiments at liquid helium temperatures and high magnetic fields.

4 Space-Resolved Measurements at the Breakdown of the QHE

In this chapter, recent results of space-resolved measurements near the breakdown, which allow to determine typical parameters of the hot-electron relaxation and excitation, are presented. From these measurements we have concluded, that the excitation is dominated by impurity-enforced inter-Landau-level scattering and the relaxation is triggered by Coulomb scattering at impurities. From the relaxation measurements by Kaya *et al.*, a clear correlation of the energy relaxation length and the energy relaxation time with the mean free path of the electrons [15] was derived.

4.1 Space-resolved relaxation measurements

In the literature there are already some studies on the geometry dependence of the QHE breakdown. In low and medium mobility samples (in the range 10^5-10^6 cm^2/Vs), a linear dependence of the critical current on the sample width was found [81]. This result implies a constant critical current density and indicates the relevance of intrinsic two-dimensional bulk properties of the 2DES for the QHE breakdown. Besides this width dependence, a length dependence of the breakdown was reported [12, 71]. Moreover, it was found that the breakdown develops over a certain drifting distance of electrons, which is explained on the basis of an avalanche heating process [13].

In their study, Kaya *et al.* have monitored the decay of the energy of hot electrons along their drift path by measurements of the longitudinal resistivity as a function of the distance from the position of the hot electron injection. As shown in the inset of Fig. 4.1, the electrons were heated in arrays of parallel channels of 100 μm length and 2 μm width. These parallel narrow channels with equivalent properties, provided a homogeneous temperature front of heated electrons before they enter the unpatterned wider region (at x=0, see Fig. 4.1). The current was adjusted such that the current density was above the critical current density in the channels (complete breakdown), but below the critical value in the wider region (width=90 μm) for x>0. A set of logarithmically

spaced, narrow potential probes was used to monitor the longitudinal resistivity, by measuring the voltage drop across each successive potential probe pairs.

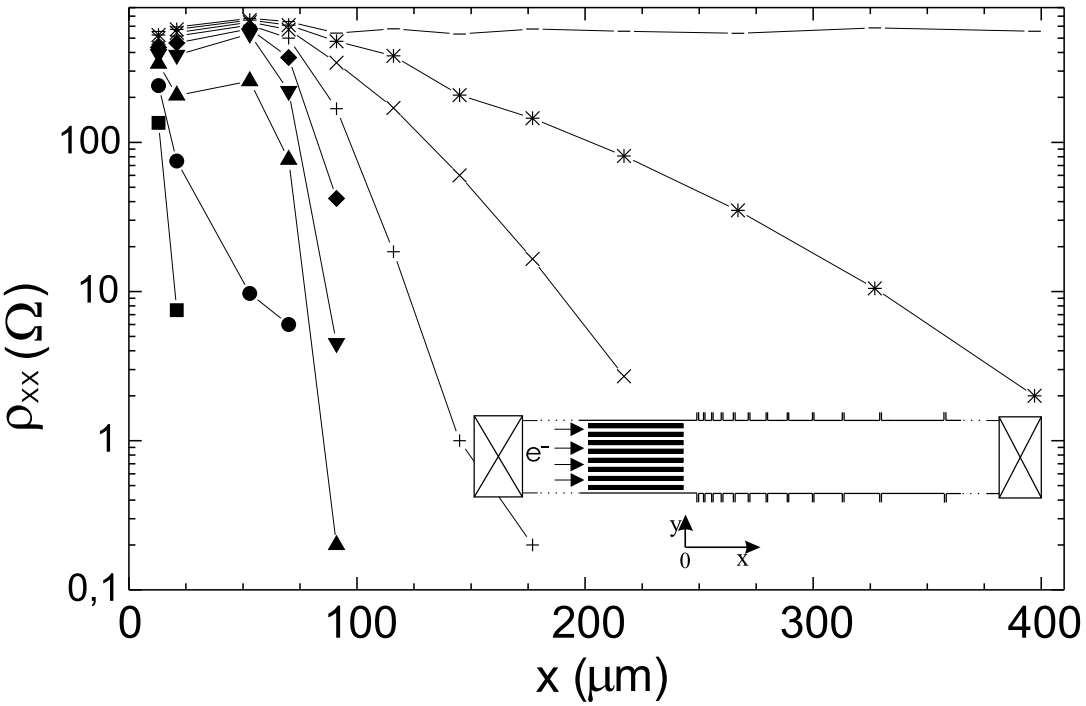

Figure 4.1: A space-resolved relaxation measurement (ρ_{xx} as a function of contact position). Dependence of the ρ_{xx} minimum (ν=2, B=4.8 T) on the distance x from the end of the constriction array (sample: n_s=2.2×10^{11} cm^{-2}, μ_H=4×10^4 cm^2/Vs), at different currents from I=34.0 μA (square) to 35.6 μA (dash) in 0.2 μA steps. Inset: scheme of the sample geometry. Data from Kaya *et al.* [15].

This array of constrictions resulted in distinct differences of the resistivity profiles $\rho_{xx}(x)$ for the two current directions. For electrons injected from the array of constrictions, the resistivity fell almost exponentially from a saturation value, with a decreasing slope while approaching the critical current I_c (see Fig. 4.1). This plot clearly demonstrates that hot electrons, heated in the channel array (ρ_{xx}>100 Ω), penetrate deeply into the wider region over length scales up to hundreds of micrometers. This is a clear indication that a certain drifting distance is necessary for the hot electrons to relax to the lattice temperature. At I_c, $\rho_{xx}(x)$ remained at the saturation value throughout the sample. For currents I<I_c of the opposite direction (current towards the array of constrictions), the QHE persisted throughout the sample. The current range, within which the relaxation near the breakdown could be observed, increased with mobility (from $\Delta I/I_c$≈5% to 25% for μ_H from 4.0×10^4 to 5.3×10^5 cm^2/Vs [15, 82, 83]).

The observed resistivity profiles $\rho_{xx}(x)$ can be approximated by the exponential dependence

$$\rho_{xx}(x) = \rho_{xx}^{0} exp\left(-\frac{x - x_0}{L_0}\right) \tag{4.1}$$

in the region with $x>x_0$, where ρ_{xx} is smaller than a certain saturation value ρ_{xx}^{0}. The value x_0 marks the end of the saturation area ($0<x<x_0$) which is mainly due to a weaker temperature dependence of ρ_{xx} at rather high electron temperatures close to the injection front. L_0 is the characteristic decay length of the resistivity at a given current $I<I_c$. To deduce L_0 as a function of the current I, the authors have considered a simple two-level-model [15]. Here, the resistivity ρ_{xx} was assumed proportional to the number of electrons N activated to the upper level. The change in time of the population of the upper level, $\mathrm{d}N/\mathrm{d}t$, depends on the balance between the generation rate due to Joule heating and the relaxation due to energy loss processes. As a result, they have obtained

$$L_0 = \frac{\ell_D}{(1 - (I/I_c)^2)}, \tag{4.2}$$

with $\ell_D=v_D\tau_0$ as the average drifting length of the electrons between two inelastic scattering events [15].

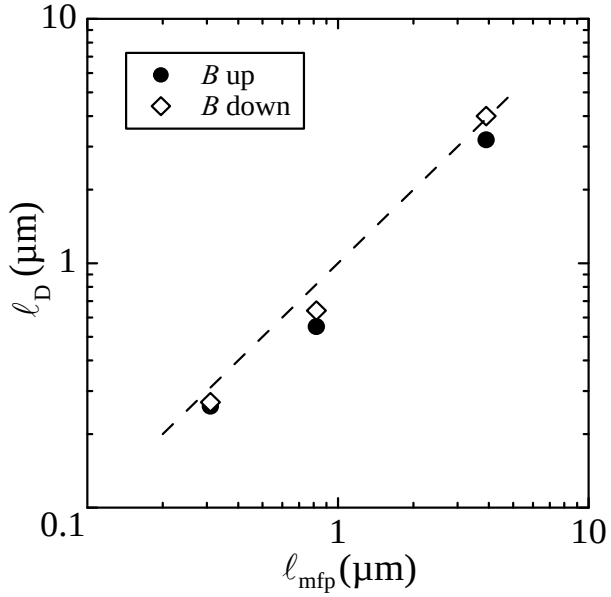

Figure 4.2: Relation between relaxation lengths and mean free paths. Relaxation lengths ℓ_D determined from plots in Fig. 4.1 as a function of the mean free path ℓ_{mfp}, deduced for samples with different mobilities (from 4.0×10^4 to 5.3×10^5 cm^2/Vs). Open and closed symbols: opposite directions of the magnetic field. Dotted line: $\ell_D=\ell_{mfp}$. Data from Kaya *et al.* [83].

From the function $L_0(I)$, the relaxation lengths ℓ_D could be determined. A re-

markable coincidence of the relaxation lengths ℓ_D with the mean free path ℓ_{mfp} was observed for samples with mobilities from 4.0×10^4 to 5.3×10^5 cm^2/Vs (see Fig. 4.2). The mean free path is mainly determined by elastic Coulomb scattering at ionized donors. Consequently, the relation $\ell_D \approx \ell_{mfp}$ indicates that the inelastic scattering (responsible for the dissipation near the QHE breakdown) is also related to Coulomb scattering. This can be attributed to a high scattering probability of electrons, incident from the x direction, into the y direction (parallel to Hall field) by Coulomb scattering, followed by an inelastic scattering event along the Hall field.

Kaya *et al.* determined the energy relaxation time τ_{rel} from the values of the energy relaxation length ℓ_D and the drift velocity v_D. The order of magnitude of the energy relaxation times (0.24-2.6 ns, for the mobilities from 4.0×10^4 to 5.3×10^5 cm^2/Vs) were found to be in good agreement with earlier assumptions, which were explained by phonon assisted dissipation [17]. However, the proportionality between the relaxation time and the Hall mobility means that the inelastic scattering rate in the samples is dominated by the scattering at impurities instead of intrinsic electron-phonon coupling properties of the GaAs bulk.

4.2 Space-resolved excitation measurements

The space-resolved excitation measurements described below aim to obtain quantitative results for the spatial development of the breakdown of the QHE as the current density is increased above the critical value. As shown in Fig. 4.3, the increase of the current density is realized by a reduction of the sample width. The constriction has a funnel shape to avoid sharp corners, which can produce enhancements of current density at the corners and local hot spots. The polarity of the DC current bias is selected such that the electrons drift from the wider part towards the constriction.

As shown in Fig. 4.3, the applied current was adjusted to make the current density j, slightly larger than the critical current density j_c within the constriction. Experiments were performed at T=1.5 K with applied DC currents of $1\mu\text{A}\leq I_{SD}\leq 50\mu\text{A}$. As in the relaxation experiments, for investigating the spatial evolution of the breakdown, 19 pairs of potential probes were attached to the constricted region of the Hall bar. Between adjacent potential probes x_n and x_{n+1} the potential drop is measured, and the longitudinal resistivity is calculated as

$$\rho_{xx}\left(x=\frac{x_{n+1}-x_n}{2}\right)=\frac{V(x_{n+1})-V(x_n)}{x_{n+1}-x_n}\frac{w}{I_{SD}} \tag{4.3}$$

All samples had identical geometries and comparable electron densities from

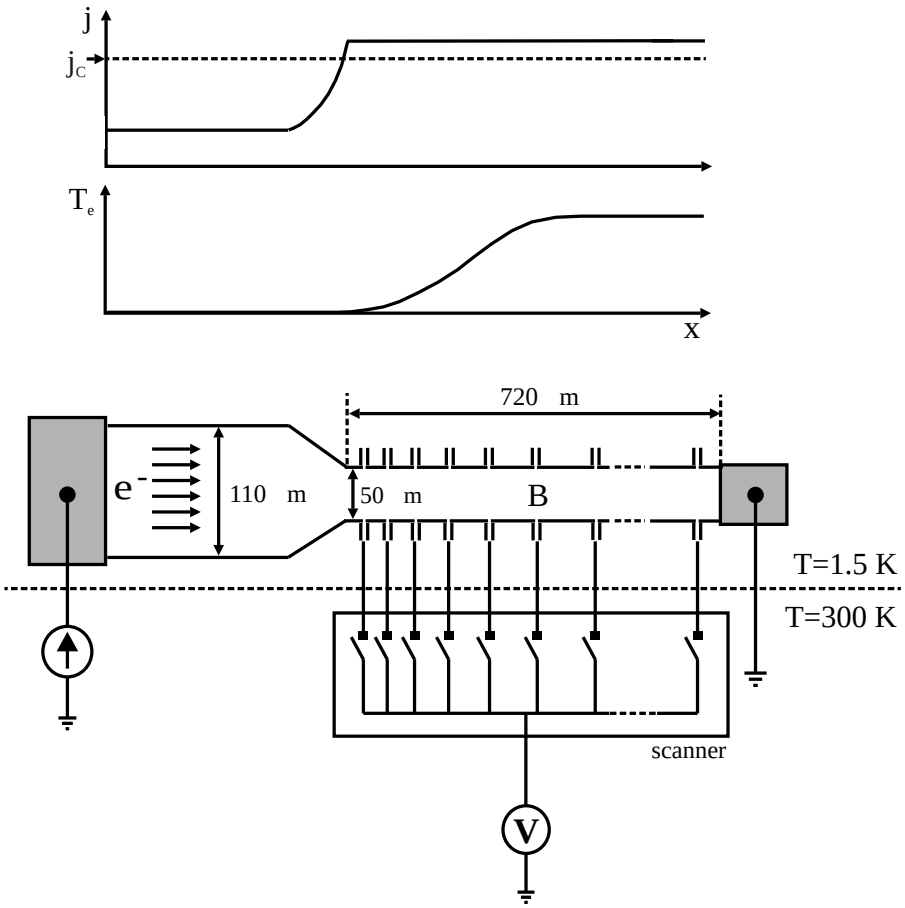

Figure 4.3: Scheme of the measurement configuration for the space-resolved excitation measurements. For investigating the excitation, 19 pairs of potential probes were attached on both sides of the constricted region of the Hall bar, where the electrons are heated. Behind the constriction, current density j and the electron temperature T_e increase.

2 to 3×10^{11} cm^{-2}, but different mobilities in the range from 4.0×10^4 to 5.3×10^5 cm^2/Vs. This allowed us to study systematically the influence of the density of scatterers on the evolution of the QHE breakdown.

In Fig. 4.4, a typical set of curves, showing the spatial evolution of the resistivity minima ${\rho_{xx}}^{min}$ at ν=2 in a constriction (w=50 μm) for various currents is shown. After a smooth growth of ρ_{xx} over rather long distances, the resistivity increases in an avalanche-like manner up to a saturation value. The shape of the $\rho_{xx}(x)$-plots changes drastically within a rather narrow range of currents around the critical value. With increasing current, the position of the sudden resistivity increase moves to smaller x-values. Further, the slope of the $\rho_{xx}(x)$-plots , Γ=dρ_{xx}/dx, changes exponentially with current in the smooth region (see Fig. 4.5). This behavior is common for all samples. However, the range of currents,

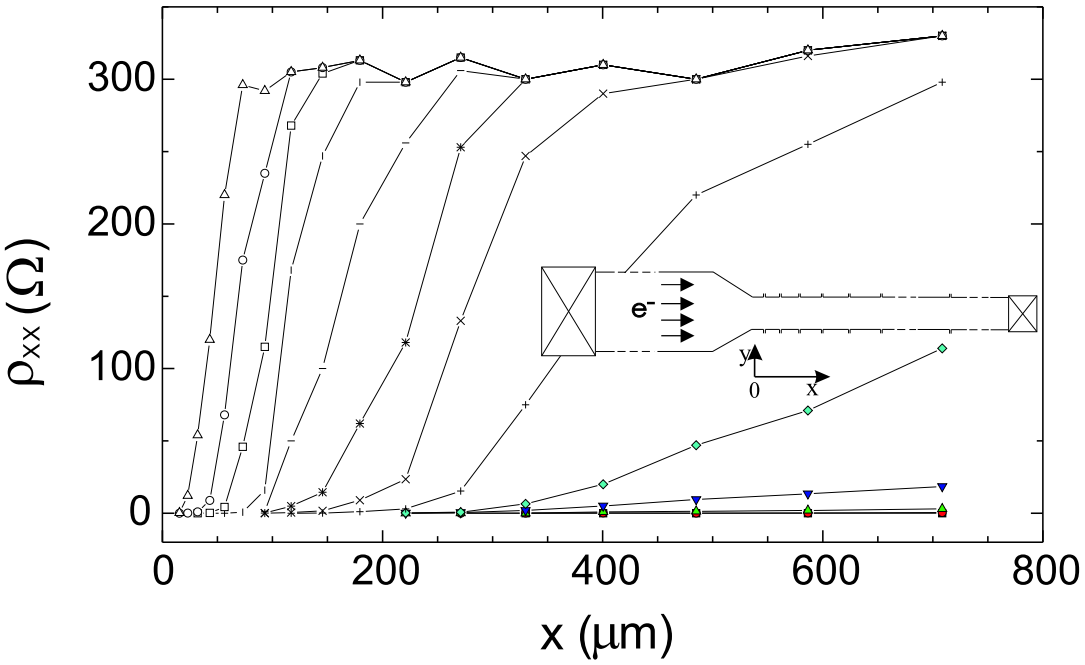

Figure 4.4: A space-resolved excitation measurement (ρ_{xx} as a function of contact position). Dependence of the ρ_{xx} minima (ν=2, B=5.8 T) on the distance x from the constriction (sample: n_s=3.0×10^{11} cm^{-2}, μ_H=1.6×10^5 cm^2/Vs). Current values from I=44.5 μA to 50.5 μA in 0.5 μA steps (lines: guides to eyes). Inset: scheme of the sample geometry.

within which the hot-electron avalanche moves from x≈500 μm to 20 μm, depends strongly on the mobility. From μ_H= 4×10^4 cm^2/Vs to 1.6×10^5 cm^2/Vs, the current range $\Delta I/I_c$, within which the avalanche is observable, increases from 4% to 10%. In other words, the QHE breakdown is more abrupt, when the density of scatterers is higher [82, 83].

The dissipative resistivity is caused by the activated electrons across the gap at the Fermi energy. In Ref. [14], a simplistic model was introduced to describe the smooth part of resistivity profiles $\rho_{xx}(x)$. The measured resistivity between the neighboring potential probes was set proportional to the number, N, of activated electrons per unit area of the sample [14]:

$$\rho_{xx} = \gamma N. \tag{4.4}$$

If a constant generation rate, $1/\tau$, of electrons per unit area to the upper Landau level is assumed, N becomes $N = t/\tau$. The drifting of electrons accumulates activated electrons as they travel in the constriction. From the drift velocity $v_D = x/t$, N can be reformulated as $N = x/v_D\tau$. If we put this in Eq. 4.4, we obtain a linear relation between ρ_{xx} and x:

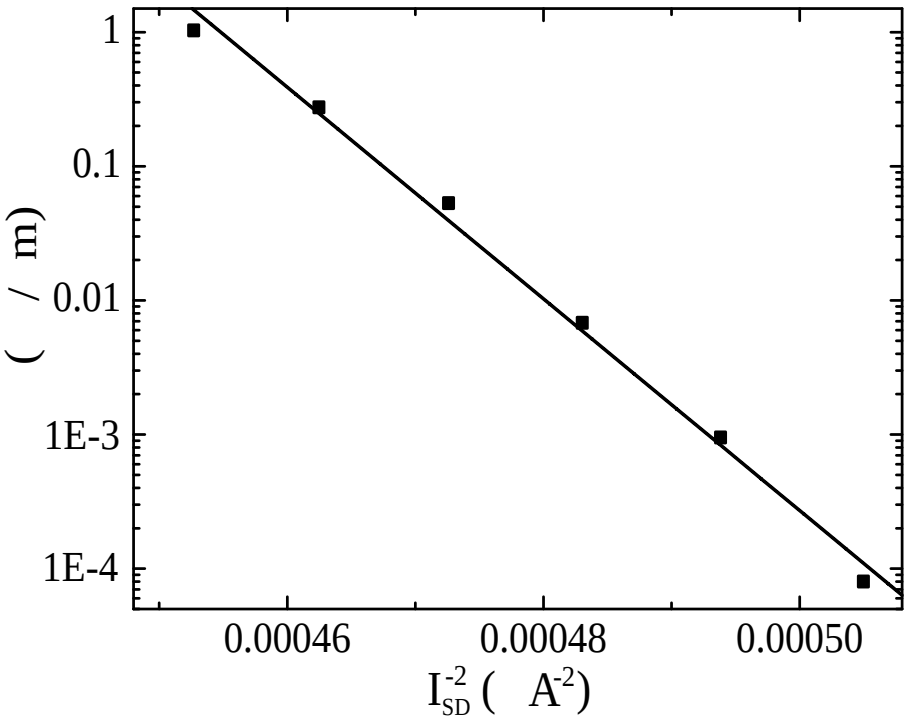

Figure 4.5: Maximum slope Γ of the $\rho_{xx}(x)$ plots with respect to the square of inverse current. Maximum slope Γ of the smooth parts of ρ_{xx} vs. x curves shown in Fig. 4.4 with respect to $1/I_{SD}^2$. Continuous line: fit to the inter-Landau-level tunneling rate $1/\tau \propto \exp(-\alpha \Delta y^2)$ (Δy - effective tunneling distance).

$$\rho_{xx} = \frac{\gamma}{v_D \tau} x, \tag{4.5}$$

providing the measured slopes $\Gamma = \mathrm{d}\rho_{xx}/\mathrm{d}x$:

$$\Gamma = \frac{\gamma}{v_D \tau}. \tag{4.6}$$

In the quasi-elastic inter-Landau-level scattering (QUILLS) model [16] the excitation of electrons to the higher Landau levels due to electric field is addressed. If the separation Δy of the initial and final state of tunneling is estimated, it is found out that $\Delta y \approx 1$ μm. This value is two orders of magnitude bigger than the length of the overlap of the corresponding wave functions, which have an extent of the order of the magnetic length $\ell_B \approx 12$ nm. This overlap is negligibly small, and so is the pure inter-Landau-level tunneling. But a mechanism, which considerably enhances the tunneling rate must be present in the sample. To overcome this discrepancy, local enhancements of electric fields due to the potential fluctuations were suggested [11, 12]. These fluctuations clearly

decrease the average separation between the Landau levels leading to an additional tunneling rate. Another suggestion to explain the QHE breakdown was based on the impurity assisted tunneling, where the electrons tunnel at the impurity states [84, 85]. Since the existence of impurities induces the potential fluctuations, both suggestions are to a certain extent similar. According to the study of Martin and Feng [85] the tunneling rate can be approximated by

$$\frac{1}{\tau} \propto \exp\left[-\frac{\Delta y^2}{4\ell_B^2}\right], \tag{4.7}$$

where $\Delta y{=}(\hbar\omega_c)/(eE_H)$ and $\ell_B{=}\sqrt{\hbar/eB}$ is the magnetic length. Since the Hall field is the Hall potential divided by the width of the sample $E_H = V_H/w$, and the Hall potential is $V_H = (BI_{SD})/(n_s e)$, we can rewrite the previous equation as

$$\frac{1}{\tau} \propto \exp\left[-\left(\frac{\hbar\omega_c n_s w}{2\ell_B B}\right)^2 \frac{1}{I_{SD}^2}\right]. \tag{4.8}$$

For a constant magnetic field B, the factor in brackets in front of the square of the inverse current in the exponential is simply a constant C. Since from Eq. 4.6, Γ is proportional to the tunneling rate, we finally have

$$\Gamma \propto \exp\left[-\frac{C^2}{I_{SD}^2}\right]. \tag{4.9}$$

This proportionality can be seen in Fig. 4.5. Therefore the exponential increase of Γ with the square of inverse current is consistent with inter-Landau level tunneling in the presence of disorder or strong potential fluctuations [14]. The function $\Gamma(I)$ is steeper with decreasing mobility, reflecting again the strong dependence of the hot-electron generation on the density of scatterers. However in these space-resolved excitation experiments it was not possible to extract the excitation times τ_{exc} of the electrons.

Moreover, the influence of the relaxation of electrons, which is simultaneously present with a rate of $1/\tau_{rel}$ was neglected in this approach [14]. The change of the effective tunneling distances along the drift direction of the electrons due to the filling of localized states in the upper Landau levels by excited electrons was also not considered. Therefore, a more sophisticated model was developed by Güven *et al.* [86], which includes these effects and is presented in the following section.

4.3 Two-level model for the excitation and relaxation of hot electrons

To simulate the excitation measurements, we have suggested a semi-empirical phenomenological model [86] that combines the idea of avalanche-like electron heating [13, 17] with the idea of quasi-elastic inter-Landau-level scattering [16] for describing the breakdown of the QHE. For an integer filling factor at T=0 K, the Fermi level is located in the gap between two Landau levels, and the upper level is empty, leading to ρ_{xx}=0. The dissipative resistivity can be ascribed to electrons, which are activated across the gap at the Fermi energy. The microscopic functional relation between the density of activated electrons N and the resistance is not known, but the same proportionality $\rho_{xx} \propto N$ [14, 15] was also assumed here.

Based on this picture, a nonequilibrium model was constructed for the change of population of the upper level by excitation and relaxation processes:

$$dN = dN_{gain} - dN_{loss}. \tag{4.10}$$

Due to energy-loss processes such as electron-phonon scattering or others, the density of electrons in the upper level decays in a characteristic time scale τ_{rel} [15],

$$dN_{loss} = N\frac{dt}{\tau_{rel}}. \tag{4.11}$$

For the excitation of electrons from the lower to the upper Landau level, the QUILLS model [16] was considered, where impurity-mediated tunneling between occupied initial and final states is assumed. This leads to a gain rate of the form

$$dN_{gain} = n_{low}\frac{dt}{\tau}, \qquad \frac{1}{\tau} = \frac{1}{\tau_{exc}}\exp\left[-\frac{\Delta y^2}{4\ell_B^2}\right], \tag{4.12}$$

where n_{low} is the density of available initial states in the lower Landau level. Following this it was assumed that the potential fluctuations lead to compressible and incompressible regions similar to that considered by Tsemekhman *et al.* [44]. At bulk filling factor ν=2 the 2DES consists of a multiply connected incompressible regime of local filling factor ν=2, which carries the dissipationless current and surrounds compressible islands, from which the current is expelled [87]. The compressible islands reduce the effective width of the incompressible regions to a value $w_0 \leq w$, where w is the width of the Hall bar.

Because of the exponential distance dependence of the QUILLS process, the majority of the activated electrons comes from the incompressible regions. Since the electron density in incompressible regions is constant ($n_s = \nu eB/h$), the area

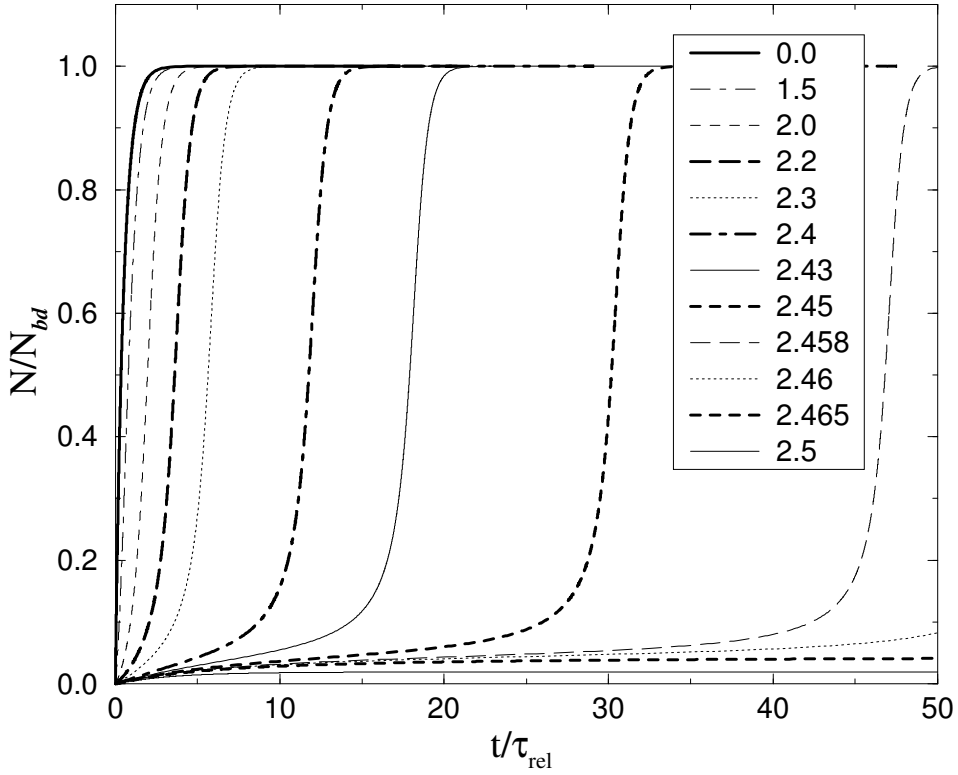

Figure 4.6: Numerical calculation of the number of electrons $N(t)$ in the upper Landau level. N/N_{bd} versus t/τ_{rel} for the values of α indicated in the legend, calculated from Eq. 4.18 with fixed τ_{exc}/τ_{rel}=1. Data from Güven *et al.* [86].

of the incompressible regions decreases, and that of the compressible regions increases linearly with N. Together with the area, also the effective width of the incompressible channels shrinks, until the width becomes too small to carry the dissipationless current. This is the critical point, where the density of excited electrons in the upper level reaches the critical value N_{bd}, at which the QHE breakdown is complete. The effective width can then be formulated as

$$w(N) = w_0 \left[1 - \sqrt{\frac{N}{N_{bd}}}\right], \tag{4.13}$$

for a circular shape of the compressible islands. If we assume a homogeneous current flow in the x direction through the Hall bar at an integer filling factor, the resulting constant Hall field in y direction tilts the Landau levels, and Δy becomes

$$\Delta y = \hbar\omega_c / eE_H, \tag{4.14}$$

where the Hall field is $E_H = V_H/w(N)$. In the gain rate equation in Eq. 4.12 only the remaining incompressible regions can contribute to the excitation process, so that $n_{low} = n_s - N$. If we put all these in Eq. 4.10 we obtain

$$\frac{dN}{dt} = \frac{n_s - N}{\tau_{exc}} \exp\left[-\left[\alpha \left(1 - \sqrt{\frac{N}{N_{bd}}} \right) \right]^2 \right] - \frac{N}{\tau_{rel}}, \tag{4.15}$$

where α is a dimensionless parameter defined as

$$\alpha = \frac{\hbar\omega_c w_0}{eV_H 2\ell_B}. \tag{4.16}$$

The excitation of electrons to the upper level is a heating process, which implies that in the stationary final state the density of electrons in the upper level cannot be larger than that in the lower level. Thus $N \leq n_s$-N and therefore $N \leq n_s/2$ including $N_{bd} \leq n_s/2$. Besides, if the model is to describe the breakdown, $N(t)$=N_{bd} must be a stationary solution. According to Eq. 4.15 this gives the requirement

$$\frac{dN}{dt} = 0 = \frac{n_s - N_{bd}}{\tau_{exc}} - \frac{N_{bd}}{\tau_{rel}} \Rightarrow \frac{\tau_{exc}}{\tau_{rel}} = \frac{n_s}{N_{bd}} - 1 \geq 1. \tag{4.17}$$

Thus, the upper bound of the breakdown density N_{bd} implies a limitation on the excitation time, which cannot be shorter than the relaxation time.

Given the model parameters and a suitable initial condition $N(t_0) = N_0$, this nonlinear differential equation $dN/dt = F(N)$ (Eq. 4.15) was solved numerically by Güven and Gerhardts [86] by inverting the relation into the integral equation:

$$t = t_0 + \int_{N_0}^{N} dN'/F(N'). \tag{4.18}$$

As seen in Fig. 4.6, the authors have calculated $N(t)$ from Eq. 4.18 in a thin slab behind the injection line at x=0, where the initial condition $N(t_0) = N_0$ is applicable. From the numerical analysis they have found a critical point $\alpha_c = 2.465$, above which N/N_{bd} increases with monotonously decreasing slope towards a limiting value smaller than 0.05 (no breakdown). While for all $\alpha > \alpha_c$ N/N_{bd} approaches the breakdown value 1.

Güven *et al.* transformed this time evolution into a stationary spatial evolution by implementing the imposed current, which causes a drift of the electron system. In this transformation, they have assumed that the drift velocity v_D does not depend on N, so that v_D is a constant, which results in

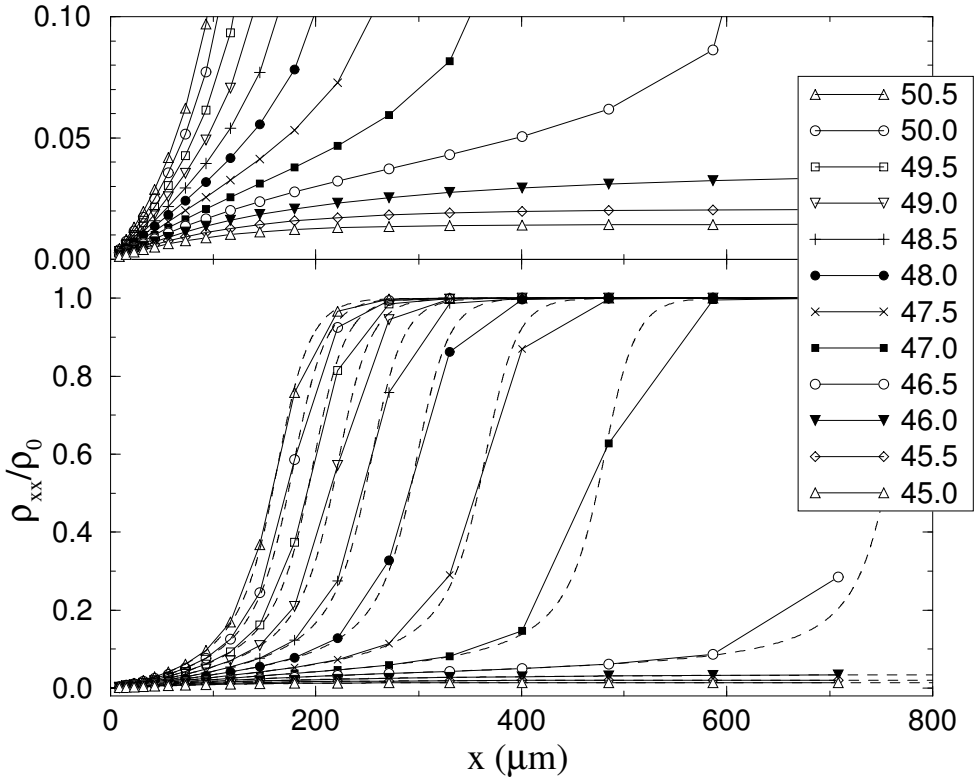

Figure 4.7: Calculated resistivities as a function of contact position. Calculated resistivities versus contact position for the current values (I in μA) are indicated in the legend for I_c=46.05 μA. Besides the direct numerical results (dashed lines) their average values, adapted to the experiment [82, 83] according to Eq. 4.20, are shown as symbols connected by straight solid lines. The upper part of the figure shows the small ρ_{xx} region enlarged. Data from Güven *et al.* [86].

$$x(t) = v_D t = \frac{V_H}{B w_0} t, \tag{4.19}$$

where w_0 is the effective width of the current carrying incompressible regions. From I_c=46 μA and α_c=2.465, this effective width is calculated as w_0=3.1 μm, which is much smaller than the sample width w=50 μm, due to the existence of the compressible puddles. In addition to the numerically calculated $\rho_{xx}(x)/\rho_0$ (dashed lines in Fig. 4.7, the authors have also calculated the average values of these results defined according to

$$\rho_{xx}\left(\frac{x_n + x_{n+1}}{2}\right) = \frac{1}{x_{n+1} - x_n} \int_{x_n}^{x_{n+1}} dx' \rho_{xx}(x'), \tag{4.20}$$

with the contact positions x_n taken from the experiment [82, 83], and plotted

them as symbols connected by straight lines.

As seen in Fig. 4.7, the numerical evaluation of the model gave a remarkably good qualitative agreement with the experimental data in Fig. 4.4. It reproduced the resistivity profile with the pre-breakdown part, the steep, avalanche-like increase and the subsequent saturation quite well. This agreement indicates that the mentioned ideas, which form our model, are relevant for the understanding of the excitation experiments.

However, some quantitative differences remain. In the experiment, ρ_{xx} exhibits for nearly critical currents and small x values, a weak linear increase (with slope $\Gamma{=}d\rho_{xx}/dx$), which is well developed in lower mobility samples [14] but not so well established in higher mobility samples [82, 83]. This slope seems to depend exponentially on the square of the inverse current, so that the logarithm of Γ as a function of I^{-2} can be well approximated by a straight line, as shown in Fig. 4.5. The model shows a similar exponential dependence at $x{=}0$,

$$\Gamma(0) = \frac{d\rho_{xx}}{dx}(0) = \frac{\rho_0}{v_D \tau_{rel}} \left\{ 2 \exp\left[-\left(\frac{\alpha_c I_c}{I} \right)^2 \right] \right\}. \tag{4.21}$$

However the dependence of Γ on I^{-2} is much weaker than that of the experimental results. For $x{>}0$, the model does not show such a well developed linear behavior, and a linear approximation is only possible with a certain ambiguity.

4.4 Summary

In summary, we have demonstrated that the excitation and relaxation of the breakdown of the quantum Hall effect evolve over drifting distances of typically some 100 μm at current densities close to the critical values.

Kaya *et al.* have measured the decay of $\rho_{xx}(x)$ if the current density becomes subcritical after the injection of electrons at $x{=}0$ [15]. The decay of the resistivity corresponds to a cooling of hot electrons via inelastic scattering processes with a characteristic inelastic relaxation length ℓ_D in the range of $0.3\ \mu\text{m}{<}\ell_D{<}4\ \mu\text{m}$ for sample mobilities of $4{\times}10^4{<}\mu_H{<}5.3{\times}10^5\ \text{cm}^2/\text{Vs}$. An unexpected agreement of the energy relaxation length ℓ_D with the elastic mean free path ℓ_{mfp} was found, which is determined by the Coulomb scattering at ionized impurities. Energy relaxation times τ_{rel} were determined from the values of the energy relaxation length ℓ_D and the drift velocity v_D. The order of magnitude of the energy relaxation times (0.24 - 2.6 ns) were found to be in good agreement with earlier assumptions in the literature.

We have also measured the increase of the resistivity $\rho_{xx}(x)$ along the current path at supercritical current densities [14, 82, 83]. The exponential increase of the slope of the resistivity profile $\Gamma{=}\mathrm{d}\rho_{xx}/\mathrm{d}x$, with the square of the inverse

current is consistent with inter-Landau level tunneling in presence of disorder or strong potential fluctuations. The function Γ is steeper with decreasing mobility, reflecting again the strong dependence of the hot-electron generation on the density of scatterers. We attribute the excitation process at supercritical currents to impurity-assisted inter-Landau-level tunneling. However in the excitation experiments it was not possible to extract the excitation times τ_{exc} of the electrons, due to the more complicated interplay between excitation, relaxation and effective width of the current carrying incompressible regions.

To simulate the excitation measurements, we have suggested a semi-empirical phenomenological model [86] that combines the idea of avalanche-like electron heating [13, 17] with the idea of quasi-elastic inter-Landau-level scattering [16] for describing the breakdown of the QHE. Based on this picture, a nonequilibrium model was constructed for the change of population of the upper level by excitation and relaxation processes. Güven and Gerhardts have calculated the time evolution of the excited electrons in a thin slab behind the injection line, and transformed the time evolution into a stationary spatial evolution by implementing the imposed current, which causes a drift of the electron system. The numerical evaluation of the model gave a remarkably good qualitative agreement with the experimental data. This agreement indicates that the mentioned ideas are relevant for the understanding of the excitation experiments. Among all modifications, they have found the closest agreement with the experiment assuming that the effective width of the compressible regions increases with $\sqrt{N}$. From general thermodynamic arguments they have found that the relaxation rate cannot be smaller than the excitation rate to the higher level, which means $\tau_{exc} \geq \tau_{rel}$. Although the dependence of the results on τ_{exc}/τ_{rel} was weak, the best results were obtained for $\tau_{exc}=\tau_{rel}$.

Since a direct deduction of these times (τ_{exc} and τ_{rel}) was not possible from the space-resolved measurements, we performed time-resolved transport measurements near the breakdown of the quantum Hall effect. The corresponding results are presented in the following chapters.

5 Time-Resolved Breakdown Measurements at Hall Bars

The main idea and motivation behind the time-resolved breakdown measurements were originated from the space resolved breakdown measurements [14, 15, 82, 83]. In the spatially resolved relaxation experiments [15], it was possible to estimate the relaxation times τ_{rel} indirectly, however in the excitation experiments [14, 82, 83] no time information about τ_{exc} could be deduced. In order to measure the τ_{exc} and τ_{rel} of the QHE breakdown directly, we have realized the following experimental setup.

5.1 Experimental setup

We have started the time-resolved breakdown measurements first on quantum Hall devices with the Hall bar geometry [88]. The width of the Hall bars and the distance between the potential probes were l=272 μm. We have fabricated the Hall bars from three different wafers, as shown in Table 5.1.

	n_s (cm^{-2})	μ_H (cm^2/Vs)
Wafer W_1	2.0×10^{11}	9×10^5
Wafer W_2	2.0×10^{11}	5×10^5
Wafer W_3	2.7×10^{11}	1×10^5

Table 5.1: Electron density and Hall mobility of the fabricated wafers, from which the Hall bars were fabricated. The parameters were determined from the transport measurements at 1.5 K.

The experimental setup is realized as shown in Fig. 5.1: a coaxial cable from a pulse generator was brought in the immediate vicinity of the QH samples [88, 89]. The impedances of the pulse generators (Hewlett Packard 8131A and 8133A) and the coaxial cables were all Z=50 Ω. In the quantum Hall regime, the resistances of the Hall bar devices are of the order of 10,000 Ω. This impedance difference causes a huge signal loss, if electric pulses are directly applied at the source and drain contacts of the QH device (similar to a signal reflection at an

open end of a wave guide). To minimize the signal loss and for a maximum power transfer, the concept **impedance matching** is widely used [90]. Since the pulse generators and the cables had an impedance of Z=50 Ω, we have attached a 50 Ω resistor in parallel with the QH devices for impedance matching.

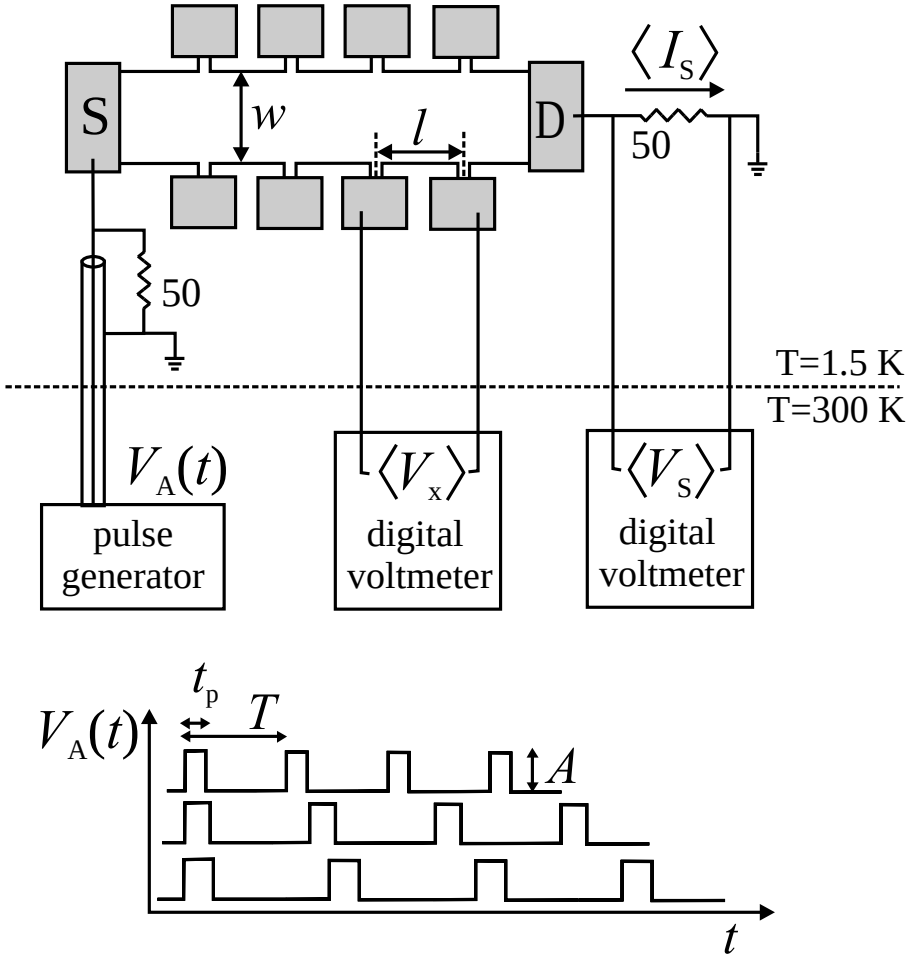

Figure 5.1: Schematic view of the time-resolved experimental setup to measure the pulse-induced breakdown in Hall bar devices. Rectangular pulses with constant duty cycle were applied between the source contact S and the ground. At the Hall bars the average longitudinal resistivity $\langle \rho_{xx} \rangle$ was measured.

Another 50 Ω resistor was attached in series with the devices (between the drain contact D and the ground) in order to measure the average current $\langle I_s \rangle$ passing through the device. The averaging of the time dependent voltages was performed by using a digital voltmeter with an input time constant t_{in} set to $t_{in} \gg t_p, T$, where t_p is the pulse width, and T is the period. Rectangular pulses $V_A(t)$, with amplitude A, were applied between the source contact S, and the ground. The pulse width t_p and the period T were increased simultaneously, keeping the duty cycle $d.c.=t_p/T$ constant for each measurement curve. This

kept the average applied voltage (and therefore the average current within a QH plateau) constant. The setup was carefully calibrated by measurements at ohmic reference resistors with known resistances. All of the experiments were done at 1.5 K, and magnetic fields B up to 12.6 T were applied perpendicular to the 2DES.

At the Hall bar devices the average longitudinal voltage $\langle V_x \rangle$ and the average current passing through the sample $\langle I_s \rangle$ were measured. The average longitudinal resistivity was calculated according to:

$$\langle \rho_{xx} \rangle = \frac{\langle V_x \rangle}{\langle I_s \rangle} \frac{w}{l} \tag{5.1}$$

where w is the width of the sample, and l is the distance between the successive measurement probes. The temporal dependence of the $V_x(t)$ and $I_s(t)$ are implicitly included in the measurement results, such that

$$\langle V_x \rangle = \frac{1}{T} \int_0^T V_x(t) dt, \tag{5.2}$$

$$\langle I_s \rangle = \frac{1}{T} \int_0^T I_s(t) dt. \tag{5.3}$$

Therefore the average longitudinal resistivity $\langle \rho_{xx} \rangle$ is in fact the ratio of the time integrals Eq. 5.2 and 5.3:

$$\langle \rho_{xx} \rangle = \left(\frac{\int_0^T V_x(t) dt}{\int_0^T I_s(t) dt} \right) \left(\frac{w}{l} \right), \tag{5.4}$$

which does not give us the time dependent pulse response of the sample $\rho_{xx}(t)$ but a value related to its integral. With this simple experimental setup, we can not monitor the pulse shape in the 2DES, but we can surprisingly determine the excitation times τ_{exc} of the breakdown of the QHE.

5.2 DC measurements

Before starting the pulse-induced breakdown measurements, we have tested and calibrated the experimental setup, and extracted sample parameters like Hall mobility and electron density by performing DC measurements. In magneto-transport measurements usually a constant current is applied to the Hall bar samples. But due to the existence of the 50 Ω resistor in parallel with the Hall bar (see Fig. 5.1), the current through the Hall bar can not be kept constant, because the resistance of the Hall bar changes continuously with the magnetic field. Thus, for the DC characterization we have applied a constant DC voltage

through the coaxial cable, as seen in Fig. 5.2 (a). Then we have measured separately the longitudinal voltage V_x, the Hall voltage V_{Hall}, and to measure the sample current we have measured the voltage V_s at the serial 50 Ω resistor.

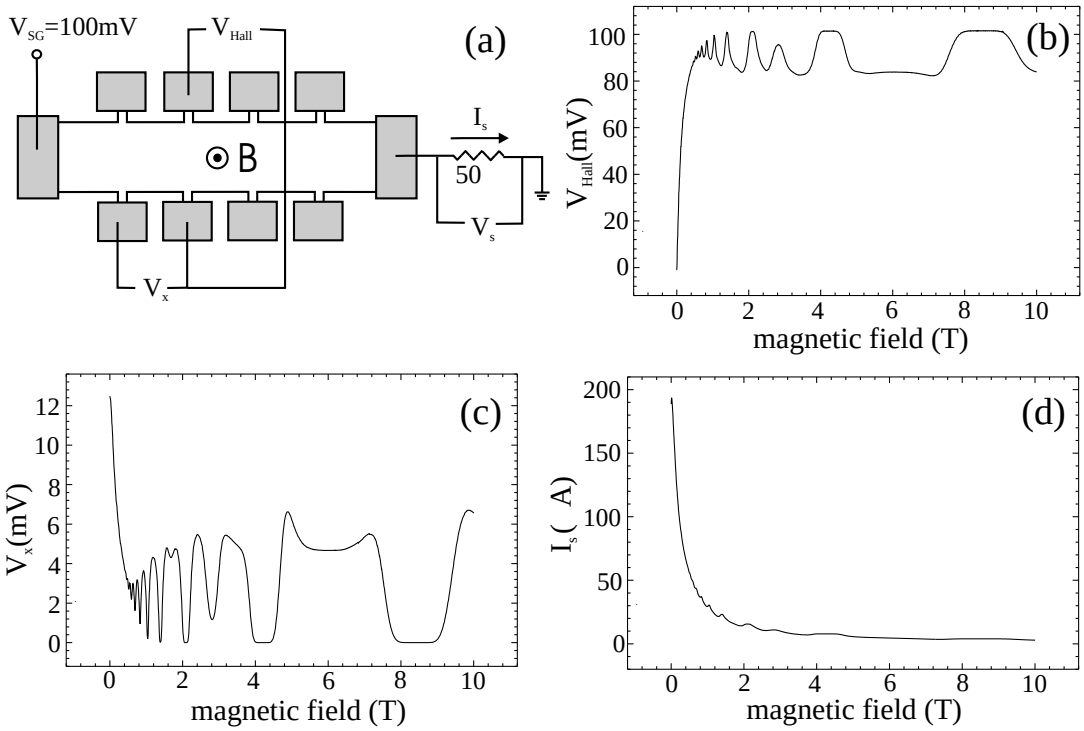

Figure 5.2: A DC measurement at a Hall bar device. (a) For the DC characterization a 100 mV DC voltage was applied through the coaxial cable. The voltages (b) V_{Hall}, (c) V_x and (d) the sample current I_s were measured as a function of the magnetic field. The Hall bar was fabricated from wafer W_2.

In Fig. 5.2 (b) the measured dependence of the Hall voltage as a function of the magnetic field is shown. At zero magnetic field, B=0 T, there is no transversal potential component so that V_{Hall}=0 mV. The Hall voltage increases as the magnetic field is increased. At around B=0.4 T is starts to oscillate, and reaches the maximum value of 100 mV around B=2.1 T. This is the QHE plateau corresponding to filling factor ν=4. The same effect repeats itself at the other QHE plateaus for ν=2 at B=4.2 T and for ν=1 at B=8.4 T. The reason is that in the QHE regime the only potential drop (apart from the current contacts) occurs in the transversal direction, but not in the longitudinal direction. Therefore the entire voltage of 100 mV, drops at the Hall potential probes, and we see the maximum value of 100 mV as the QHE plateaus.

This can be confirmed in Fig. 5.2 (c), where the longitudinal voltage V_x is measured. As it is seen from the plot, in the QHE regime there is no potential drop (V_x=0 mV) at magnetic fields corresponding to the quantum Hall plateaus at

B=2.1 T, B=4.2 T and B=8.4 T. In Fig. 5.2 (d) the magnetic field dependence of the sample current (I_s=V_s/50 Ω) is shown. The current starts with about 200 μA at B=0 T and monotonously decreases till B=0.4 T. This is an expected result, because the voltage is kept constant, and the Hall resistance increases with the magnetic field. At about 0.4 T the current starts to oscillate, and it has local maxima exactly at the QHE plateaus. This is also an expected result, because the total resistance of the Hall bar is R_{tot}=R_{Hall}+R_x, and the total resistance R_{tot} has local minima at the QHE plateaus. This can be clearly seen, when the ρ_{xx}=$(w/l)R_{xx}$ and ρ_{xy}=R_{xy} curves in Fig. 5.3 (a) and (b) are added.

If the data in Fig. 5.2 (b) and (c) are divided by the current in Fig. 5.2 (d), we obtain the ρ_{xx} and ρ_{xy} curves according to

$$\rho_{xx} = \frac{V_x}{I_s},\ \rho_{xy} = \frac{V_{Hall}}{I_s}, \tag{5.5}$$

where the geometry factor for the measured Hall bar is (w/l)=1. These curves are shown in Fig. 5.3, from which the electron density n_s and the Hall mobility μ_H of this QH sample were calculated.

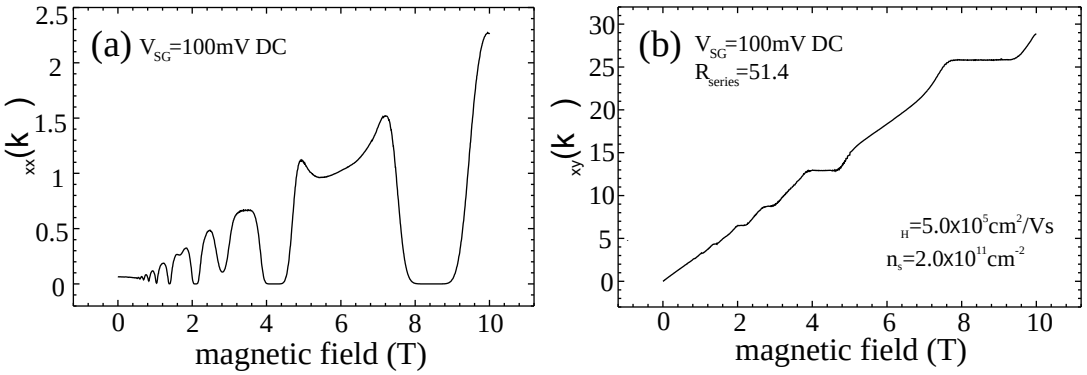

Figure 5.3: (a) ρ_{xx} and (b) ρ_{xy} curves were calculated from the previous curves in Fig. 5.2 according to Eqs. 5.5. From these curves the electron density n_s and Hall mobility μ_H were calculated. From the plateau values of the Hall resistance, the value of the serial resistor was calibrated as R_{series}=51.4 Ω. The Hall bar was fabricated from wafer W_2.

From Eqs. 2.24 and 2.31 the electron density is equal to

$$n_s = \frac{1}{\left(\frac{\rho_{xy}}{B}\right)e} = \frac{1}{me}, \tag{5.6}$$

where m=ρ_{xy}/B is the slope of the Hall curve in Fig. 5.3 (b). From this relation, the electron density of this sample was calculated as n_s=2.0×10^{11} cm^{-2}. To

calculate the Hall mobility μ_H the Eq. 2.29 was used, where ρ_{xx} is the resistivity at B=0 T which can be extracted from Fig. 5.3 (a). Thus according to

$$\mu_H = \frac{1}{\rho_{xx}(B{=}0\text{ T})n_s e}, \tag{5.7}$$

and knowing n_s, we have calculated the mobility as μ_H=5×10^5 cm^2/Vs. In Fig. 5.3 (b) the quantum Hall plateaus should have universal values without any parameter dependence. From these plateau values of the Hall resistance, the value of the serial resistor was calibrated as R_{series}=51.4 Ω (not 50 Ω in reality) and the results were corrected accordingly.

5.3 Tests for pulse measurements at B=0 T

We have first tested the semi-rigid coaxial cables at room temperature by simply connecting one of the coaxial cables to the pulse generator and the other one to the oscilloscope. A thin wire was soldered between the open ends of the inner wires of the coaxial cables. A pulse train was applied from the pulse generator, and the result was monitored at the oscilloscope. For five different lengths (L=1, 2, 4, 7, 11.5 cm) of the soldered wire, we have checked the signal quality and the signal loss. The best result was obtained, as expected, with the shortest wire L=1 cm, which provided the shortest rise and fall times t_{rise}=t_{fall}=80 ps. For L=2 cm these transitions times were around 170 ps, and for L=4 cm around 290 ps.

As it is seen from these test measurements, the connection wires in Fig. 5.1 should be as short as possible. The length of the connection wires, either between the source S and the inner conductor of the semi-rigid cable, or between the drain D and the serial resistor, was around 1 cm. We have repeated the test measurements at 1.5 K, and found a slight improvement in the signal quality. However, we have also discovered a small thermoelectric voltage of about 1.2 mV between the inner and outer conductors of the semi-rigid coaxial cables, caused by the difference between room and helium temperatures. But this background voltage is negligible, if it is compared with the breakdown voltages of the order of 1 V.

The best way to test the pulse transfer is to use the setup in Fig. 5.1 with real Hall bar samples at zero magnetic field. As already explained in the previous sections, we have applied rectangular pulses with amplitude A, and varied the period T of the pulses from 4 ns to 2 ms by keeping the duty cycle constant at 20%. As it is seen in Fig. 5.4 (a) the average longitudinal voltage $\langle V_x \rangle$ is more or less constant for all amplitude and period values. This was expected, because the duty cycle d.c.=t_p/T (and therefore the applied average voltage) was kept constant. This expected constant response also means that the average pulse

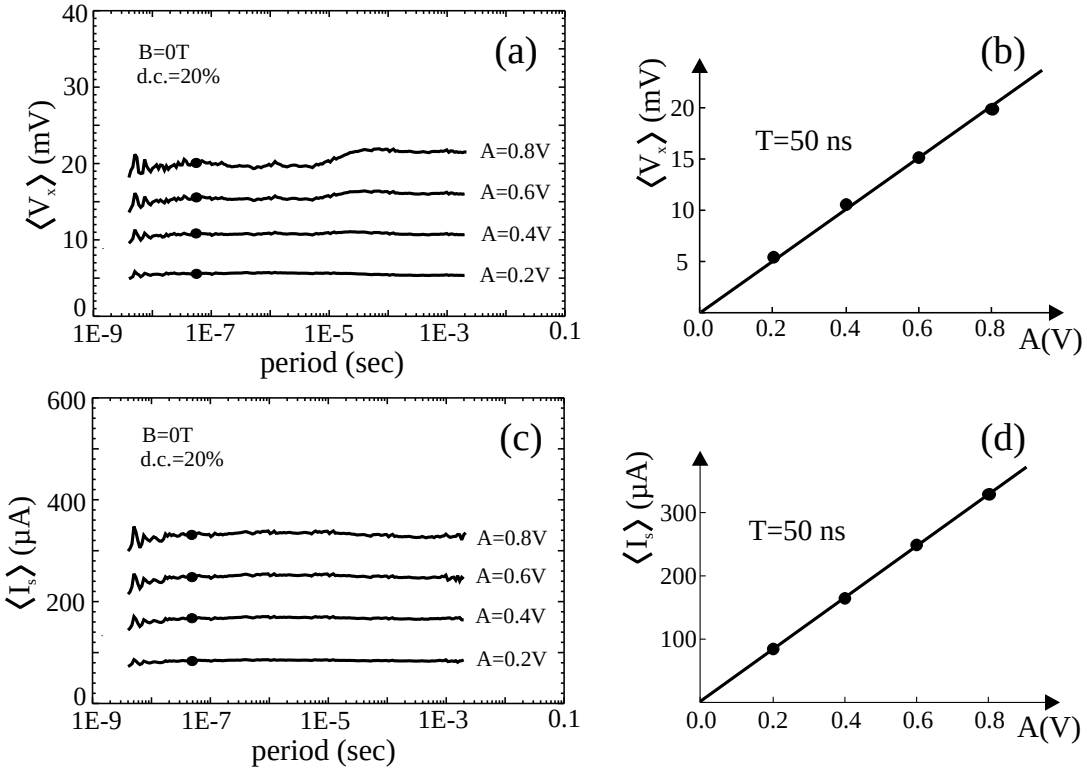

Figure 5.4: Test measurements of pulse transfer - the amplitude dependence. (a) Average longitudinal voltage $\langle V_x \rangle$ versus period T for different pulse amplitudes A at B=0 T. (b) $\langle V_x \rangle$ versus A for T=50 ns. (c) Average sample current $\langle I_s \rangle$ versus period T for different pulse amplitudes A at B=0 T. (d) $\langle I_s \rangle$ versus A for T=50 ns. The Hall bar device was fabricated from wafer W_2.

transfer indeed works quite well, even for very short pulses in the nanosecond regime. But we do not know the real time dependent pulse response of the 2DES. The same behavior can also be observed in the average sample current $\langle I_s \rangle$ in Fig. 5.4 (c). If we choose a period value, for example T=50 ns, and plot the $\langle V_x \rangle$ and $\langle I_s \rangle$ as in Fig. 5.4 (b) and (d), we see that both $\langle V_x \rangle$ and $\langle I_s \rangle$ increase linearly with the pulse amplitude A.

We have performed similar measurements but this time for a constant amplitude A=1 V and for different duty cycles as shown in Fig. 5.5. As it is seen in Fig. 5.5 (a) and (c) the average longitudinal voltage $\langle V_x \rangle$ and the average current $\langle I_s \rangle$ are more or less constant for all duty cycle and period values. In Fig. 5.5 (b) and (d) the linearity with the duty cycle is shown. We can also verify that $\langle \rho_{xx} \rangle \approx \rho_{xx} \approx 65\ \Omega$ if the $\langle V_x \rangle$ values are divided by $\langle I_s \rangle$ in Fig. 5.4 and 5.5, being in agreement with the ρ_{xx} value at B=0 T in Fig. 5.3 (a).

From these measurements we can conclude that the average pulse transfer is realized successfully with the discussed measurement setup, although we can

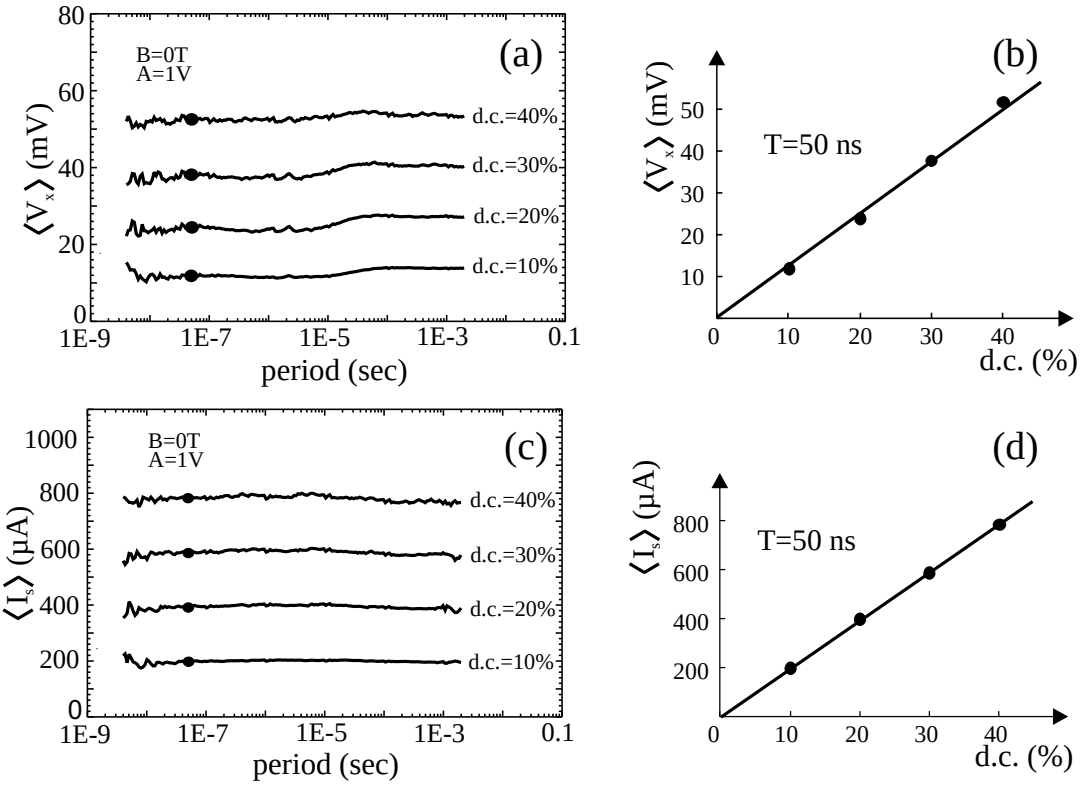

Figure 5.5: Test measurements of pulse transfer - the duty cycle dependence. (a) $\langle V_x \rangle$ versus T for different pulse duty cycles at B=0 T. (b) $\langle V_x \rangle$ versus duty cycle for T=50 ns. (c) $\langle I_s \rangle$ versus T for different duty cycles at B=0 T. (d) $\langle I_s \rangle$ versus duty cycle for T=50 ns. The Hall bar was fabricated from wafer W_2.

not determine the individual pulse shape in the 2DES. For small period values, there are oscillations, which repeat themselves in Fig. 5.4 (a) and (c). This can be explained by a ringing effect in the real time dependent pulse shape in the Hall bar sample. This behavior can also be observed in Fig. 5.5 (a) and (c) if the results are plotted against the pulse width. Also around T=10 μs there is a slight increase in $\langle V_x \rangle$. We attribute this to an effective heating of the 2DES by longer and longer pulse durations.

5.4 Pulse-induced breakdown of the QHE

After the test measurements at B=0 T, we have applied magnetic field, and repeated the measurements at quantum Hall plateaus for different pulse amplitudes and duty cycles [88, 89]. We have determined the magnetic field values of the integer filling factors by manually controlling the magnetic field and the sample current. The integer filling factor is located at the magnetic field value,

at which a maximum of the critical current is observed. We have also measured the dependence of the pulse-induced breakdown on magnetic field and temperature.

5.4.1 Amplitude and duty cycle dependence

Fig. 5.6 (a) and (b) show the typical pulse-induced breakdown curves of Hall bars with the same geometry parameters but fabricated from different wafers at filling factor ν=4. Each curve is measured by applying pulses with a constant amplitude A, and a constant duty cycle of 20%. In Fig. 5.6 (a) both the average resistivity and the average current are plotted as a function of the pulse period.

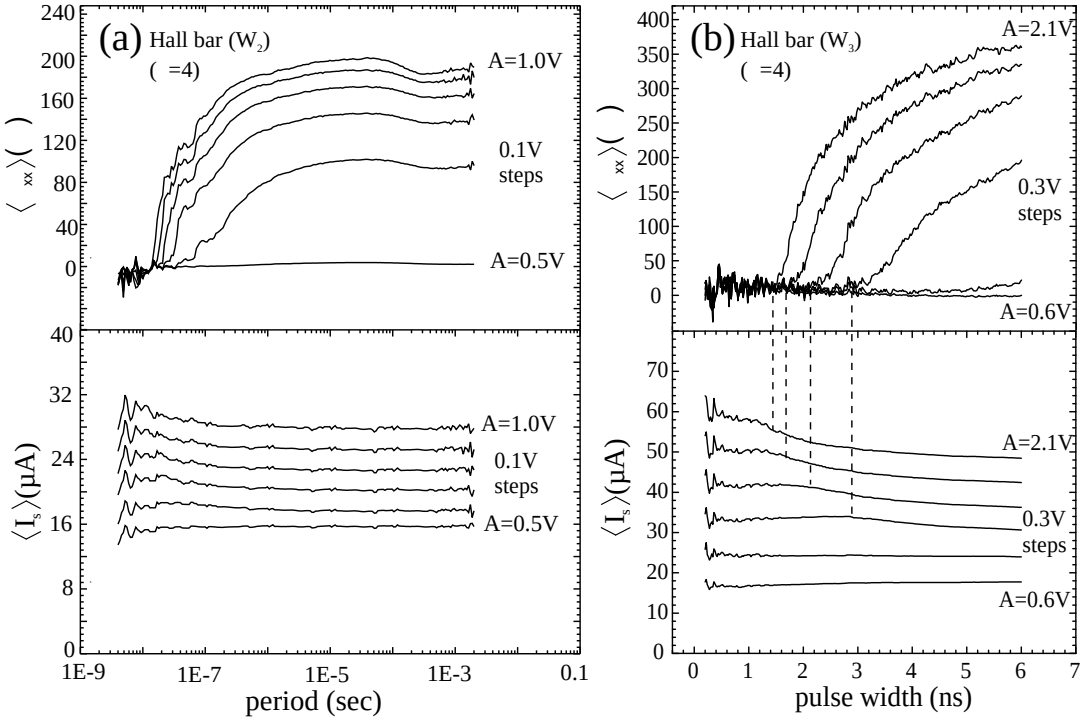

Figure 5.6: Amplitude dependence of the pulse-induced breakdown at Hall bar devices. (a) Average longitudinal resistivity $\langle \rho_{xx} \rangle$ and average current $\langle I_s \rangle$ of a Hall bar (wafer W_2) measured as a function of the pulse period. The amplitude A is varied from 0.5 to 1.0 V with 0.1 V steps. The filling factor is ν=4, and the corresponding DC critical voltage and current values are V_{SD}^c=0.54 V and I_{SD}^c=81 μA respectively. The pulse generator was HP8131A, with which millisecond pulses could be applied. (b) Pulse-induced breakdown measurements at a Hall bar device with a lower mobility (wafer W_3) at filling factor ν=4 (V_{SD}^c=0.73 V, I_{SD}^c=103 μA). The curves are plotted as a function of the pulse width. The pulse generator was HP8133A, with which only nanosecond pulses could be applied.

Before starting the pulse-induced breakdown measurements, we have first determined the DC breakdown conditions for the Hall bar in Fig. 5.6 (a) for filling factor ν=4. The applied DC voltage was increased until the QHE breakdown was detected at the longitudinal voltage V_x. The corresponding current value measured at the serial resistor I_s=V_s/R_{series}=81.5 μA is the critical current of the QHE breakdown I^c_{SD}=I_s. If we divide V^c_{SD}=0.54 V by I^c_{SD}=81.5 μA, we obtain R=6626 Ω. This value is 173 Ω greater than the ρ_{xy} value ρ_{xy}=6453 Ω at ν=4, because we have the 50 Ω resistor and the resistances of the source and drain contacts in series.

Since the critical DC voltage is V^c_{SD}=0.54 V, as expected, there is no breakdown for an amplitude of A=0.5 V, such that $\langle\rho_{xx}\rangle\approx$0, and the average current stays constant for all period values. However, as the amplitude is increased to A=0.6 V, above the critical voltage, the QHE breaks down at a certain critical period in the nanosecond regime (in reality at a critical pulse width t^c_p, which will be discussed in the next paragraphs). The breakdown can be observed in principle on both sets of the graphs in Fig. 5.6 (a) (in Fig. 5.6 (b) this is better visible), with the increase in average longitudinal resistivity $\langle\rho_{xx}\rangle$, and with the decrease in the average current $\langle I_s\rangle$. As the amplitude is further increased, the breakdown occurs at smaller critical periods (in reality critical pulse widths t^c_p).

These experiments were performed in MPI Stuttgart with the pulse generator HP8131A, which was capable to vary the pulse width from the nanosecond to the millisecond range. From these measurements we have seen that the critical times of the QHE breakdown were in the nanosecond range. Therefore the pulse generator HP8133A used at the Technical University of Braunschweig, which could realize only nanosecond pulses, was appropriate for our purposes. We have repeated the previous amplitude measurements with this pulse generator on another Hall bar sample (from wafer W_3) and observed a similar breakdown behavior.

Fig. 5.6 (b) shows the pulse-induced breakdown measurements on this Hall bar device (at ν=4) for different pulse amplitudes. Both the average longitudinal resistivity and the average current are plotted as a function of the pulse width. For this filling factor, the critical DC breakdown voltage and the critical current were V^c_{SD}=0.73 V and I^c_{SD}=103 μA respectively. These values are higher than the values of the previous sample, because this is a lower mobility sample. As it was in the previous case, there is again no breakdown for an amplitude of A=0.6 V, which is smaller than the critical voltage. However, as the amplitude is increased to A=0.9 V, above the critical DC voltage, the QHE breaks down at a certain critical pulse width. This can again be observed on both sets of the graphs in Fig. 5.6 (b), with the increase of $\langle\rho_{xx}\rangle$, and correspondingly with the decrease of the average current. In Fig. 5.6 (b) the breakdown that is observed in the average current curve is more pronounced than it is in Fig. 5.6 (a), because the sample has a lower mobility. The lower mobility samples have

larger ρ_{xx} values, so that the current drop in the QHE breakdown is higher, and therefore the inflexion point can be determined more easily, as it is clearly seen in 5.6 (b). As the amplitude is increased further, the breakdown starts at smaller pulse widths, *i.e.* the higher the amplitude is, the lower is the critical pulse width t_p^c.

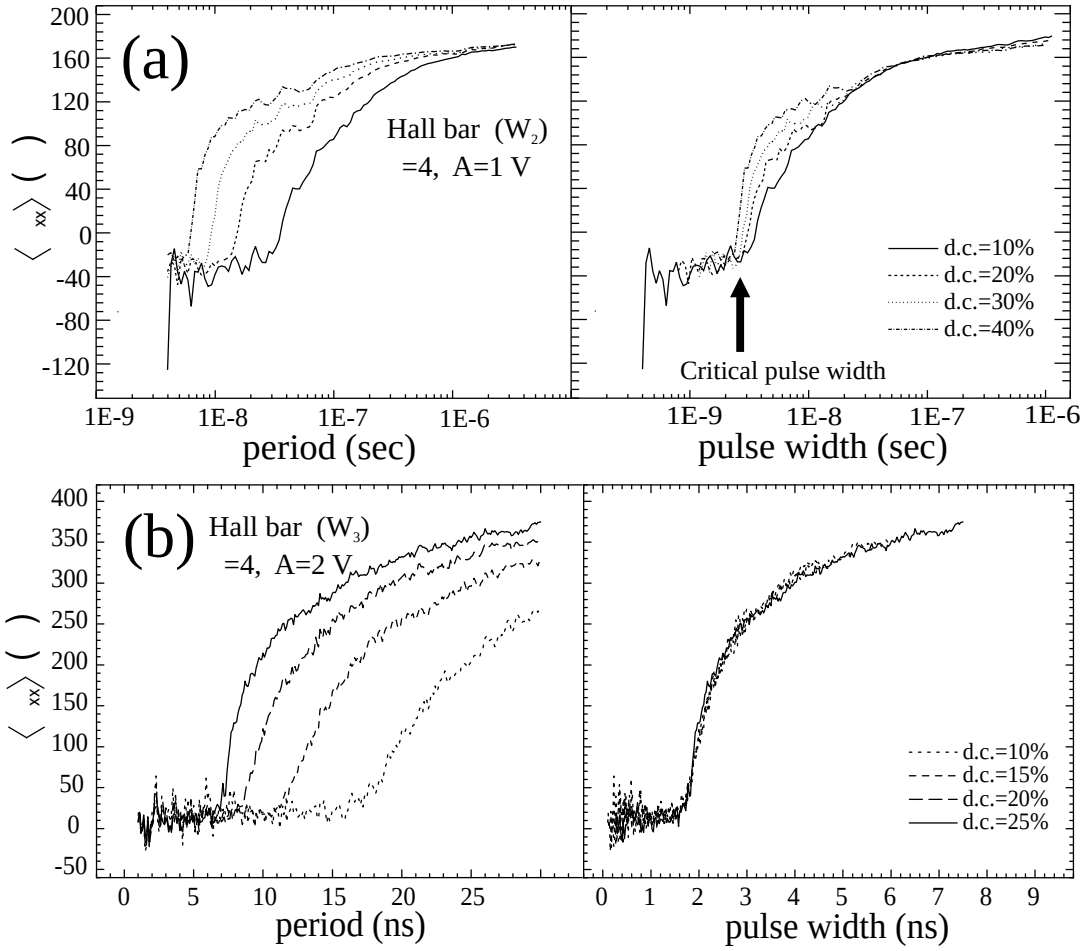

Figure 5.7: Duty cycle dependence of the pulse-induced breakdown at Hall bar devices. (a) For a constant amplitude A=1 V, at ν=4, the breakdown curves are plotted as a function of period and pulse width for different duty cycle values. (b) Same experiment with another sample with lower mobility.

As stated before, these experiments were performed with a constant duty cycle, such that both the pulse width and the pulse period were changed simultaneously. Thus, the occurrence of dissipation for pulse widths $t_p > t_p^c$ is not a consequence of the change of the average source-drain current (as $\langle I_s \rangle \approx$constant holds), but of the process during the pulse duration itself. To prove this, we have studied the breakdown behavior of the Hall bar samples for different pulse-to-pause ratios. Or in other words to determine whether the period or the pulse

width is the essential parameter, we have repeated the breakdown measurements for a constant supercritical amplitude but for different duty cycles (*i.e.* for different average currents). In Fig. 5.7 (a) and (b) the breakdown curves are plotted first as a function of the period T (on the left), and then as a function of the pulse width t_p (on the right) for Hall bar samples with two different mobilities (from wafers W_2 and W_3). The data on the left and on the right are exactly the same data, which have the same temporal breakdown information. The $\langle \rho_{xx} \rangle$ values on the right hand side graph are only scaled with respect to the pulse width for the corresponding duty cycles.

From the left hand side graphs in Figs. 5.7 (a) and (b), it is clearly seen that there does not exist a critical period for a certain constant amplitude. However on the right hand side graphs of Figs. 5.7 (a) and (b), it is clearly seen that the curves almost coincide at a critical pulse width t_p^c. This means that the breakdown starts at the same critical pulse width for different periods (*i.e.* for different average currents and pauses between the pulses).

In the Hall bar sample with lower mobility, it is interesting to observe that the curves exactly overlap for the duty cycle range between 10% and 25%. This indicates the fact that the pause between the pulses has no important relevance. There is no accumulative effect of dissipation as long as the pause between two subsequent pulses is not shorter than the relaxation time. The exact overlap in the lower mobility sample therefore indicates a complete relaxation of the pulse-excited electrons back to the QH state on this time scale. However, for the higher mobility sample, the curves do not overlap exactly, indicating that a complete relaxation does not take place.

5.4.2 Magnetic field dependence

Apart from the integer filling factors, we have also measured the response of the 2DES to the electrical pulses inside and outside the QHE plateaus. As shown in Fig. 5.8 (a), for the off-plateau magnetic field values (B=1.8 T and 2.4 T) the response of the 2DES is totally different than for the in-plateau value (B=2.1 T). In both of the off-plateau curves, the $\langle \rho_{xx} \rangle$ starts as expected from a nonzero value, decreases down and saturates at a more or less constant value. This decrease is due to electron heating caused by the electrical pulses, which will be discussed at the end of this section. The curve at 1.8 T has smaller values than the curve at 2.4 T, because this is the lower flank of the fourth plateau. This can be clearly seen in Fig. 5.8 (b), where the magnetic field values of the curves in Fig. 5.8 (a) are indicated by arrows.

In Fig. 5.8 (c) from the breakdown curve ($\langle \rho_{xx} \rangle$ vs. period) at filling factor ν=4 we have determined three $\langle \rho_{xx} \rangle$ values for three different pulse widths t_p in the QHE, QHE breakdown and complete QHE breakdown regions. We have then repeated this for different magnetic field values at the QHE plateaus ν=2

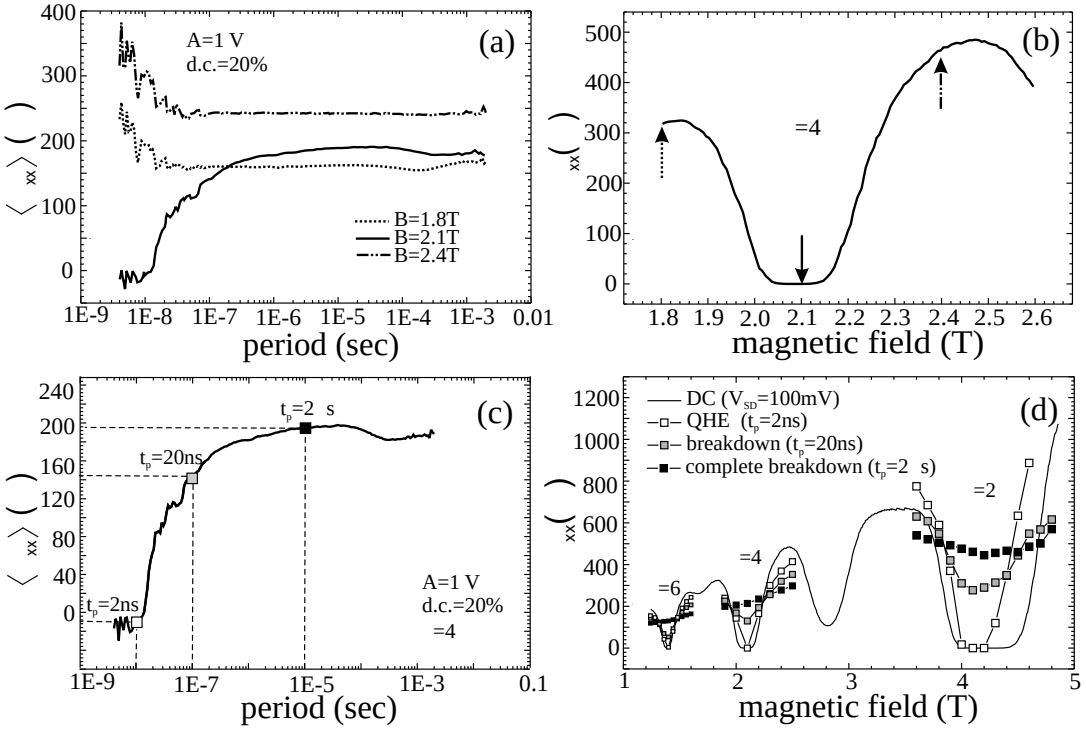

Figure 5.8: Magnetic field dependence of the pulse-induced breakdown at a Hall bar device. (a) The response of the 2DES (wafer W_2) to the electrical pulses inside and outside the QHE plateau. (b) The corresponding SdH curve, where the arrows show the measurement positions. (c) Determination of the average longitudinal resistance values for three different pulse widths at B=2.1 T. (d) The comparison of the DC SdH curve and the pulse width dependent breakdown.

(A=2 V), ν=4 (A=1 V) and ν=6 (A=0.5 V), and plotted the curves in Fig. 5.8 (d). The solid line in Fig. 5.8 (d) is the DC SdH curve, while the white, gray and black squares are the average longitudinal resistivity $\langle \rho_{xx} \rangle$ values at pulse widths t_p=2 ns, 20 ns and 20 μs. For t_p=2 ns, QHE is observed in all of the plateaus, but for t_p=20 ns there is already breakdown. If the pulse width is further increased to t_p=20 μs we observe complete breakdown, so that the minima at the integer filling factors almost disappear. The pulse-induced breakdown behavior around the three different plateaus is qualitatively the same, and it resembles apparently the DC breakdown behavior. This agreement is another evidence for the correctness of our pulse measurement technique. The plateau at ν=2 of the DC measurement (solid line) is a little wider than that of the pulse measurements, because the applied DC voltage is 100 mV, which is half of the average applied voltage for the pulses (1 V $\times$ 20% = 200 mV).

We have already mentioned that in Fig. 5.8 (a) there is a resistivity drop for bigger pulse width values, indicating an electron heating in the 2DES. We have

demonstrated this idea by applying pulses at the Hall bars, by measuring the AC SdH oscillations for different pulse widths (20% duty cycle) at the ambient temperature 1.3 K.

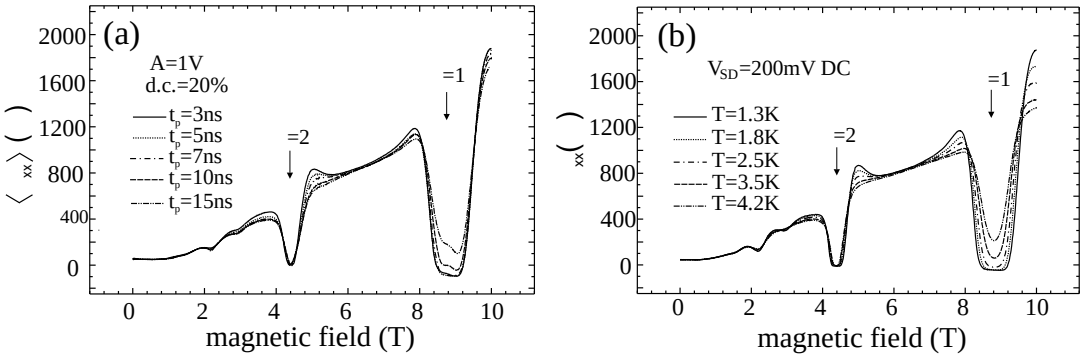

Figure 5.9: Electron heating with electrical pulses (SdH curves with pulses. (a) Short electric pulses with constant duty cycle are applied at a Hall bar device (wafer W_2) at 1.3 K. For each curve the applied average voltage is kept constant (due to the constant duty cycle), but the longer the pulses are, the more is the 2DES heated. (b) The corresponding SdH curves at different ambient temperatures show qualitatively a similar behavior, proving that the temperature of the electron system increases with increasing pulse width.

As seen in Fig. 5.9 (a) for each curve we have applied A=1 V pulses with a duty cycle of 20%. This means that for all curves the applied average voltage is 200 mV. Although the injected energy is almost constant within each plateau, the longer the pulses are, the warmer is the 2DES. This can easily be verified, if the SdH curves are measured for a DC applied voltage of 200 mV at different ambient temperatures. As shown in Fig. 5.9 (b) we have done these measurements for five different ambient temperatures between 1.3 K and 4.2 K. As the temperature is increased the SdH oscillations become smoother, with decreasing maximum and increasing minimum values. A qualitatively similar behavior can be observed also in the pulse measurements. Therefore, as we did in the duty cycle measurements, we can again conclude that the electrons are heated within the pulse, and the pause between the pulses does not play a significant role. As seen in Fig. 5.9, this is observed both within and outside the QH plateaus.

5.4.3 Temperature dependence

In order to confirm that the pulse-induced breakdown is dominated by electronic but not by phononic processes, we have repeated the measurements at different lattice temperatures T=1.5 K and T=4.2 K. The ambient temperature was varied in the variable temperature insert (VTI) by varying the pumping rate of the VTI. The duty cycle was 20%, and the measurements were performed at

ν=2 on a Hall bar sample, which was fabricated from wafer W_2 with a channel width of w=200 μm.

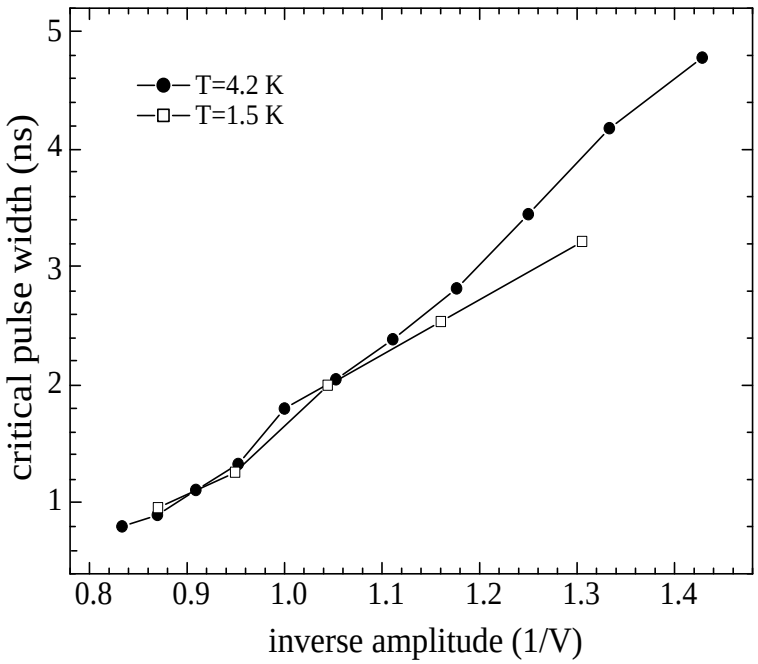

Figure 5.10: Temperature dependence of the pulse-induced breakdown at Hall bar devices. Pulse-induced breakdown measurements are shown at two different temperatures T=1.5 K and T=4.2 K. In this temperature range a clear temperature dependence could not be found. This experiment demonstrates that the phonons do not play a significant role in the pulse-induced breakdown or at least such phononic processes are slower than the electron excitation.

As seen in Fig. 5.10, the critical pulse widths are plotted as a function of the inverse amplitude of the pulses, and the two curves almost coincide. Therefore we can say that there is no significant temperature dependence in this temperature range. This experiment demonstrates that the phonons do not play a significant role in the pulse-induced breakdown or at least such phononic processes are slower than the electron excitation. However, it should be noted that the presence of phonons is inevitable to mediate inelastic electronic transitions between Landau levels along the Hall field direction, according to $|\Delta k|=|\Delta y|/\ell_B^2$ [91].

5.5 A simple drift model and mobility dependence

It is possible to explain the results as described in the previous sections by a simple drift model. In the previous studies of Kaya *et al.* [14, 15], the authors

concluded that the relaxation and excitation of the electrons near the QHE breakdown are due to the inter-Landau-level transitions, which are triggered by Coulomb scattering at impurities. We can consider the case for the Hall bars and assume, that these impurities are distributed homogeneously throughout the Hall bar as pictured in Fig. 5.11 (a).

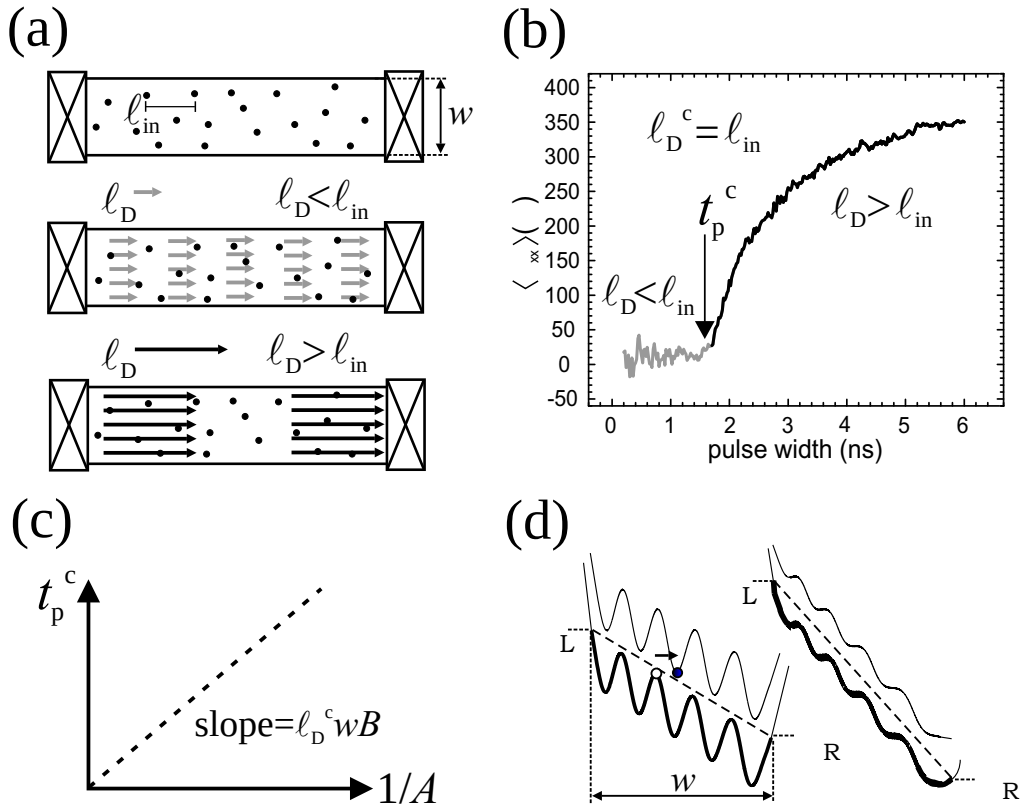

Figure 5.11: A simple drift model. (a) Picture of the drifting distance ℓ_D of electrons. If ℓ_D reaches the average scattering distance ℓ_{in}, the breakdown occurs. (b) The corresponding breakdown curve. (c) The expected linearity between the critical pulse width and the inverse amplitude. The slope should give the critical drift length. (d) Scheme of Landau-levels in the presence of potential fluctuations (Left: low Hall field, right: high Hall field. w: channel width of the Hall bar. μ_L ,μ_R: chemical potentials at the left and the right edge of the Hall bar).

At an integer filling factor the electrons drift with a constant velocity v_D along the Hall bar. Within a pulse width of t_p the drift length is ℓ_D=v_D×t_p. Since the voltage level is set to zero within the interval between the pulses, the drifting of electrons takes place only within a pulse. As long as the pulse amplitude A is kept below the critical DC voltage V_{SD}^c (A<V_{SD}^c) there is no breakdown at all, and the system is always in the QH state, whatever the pulse width is. Even if the pulse amplitude is increased above the critical voltage (A>V_{SD}^c), there is no

breakdown for short pulses (gray arrows in Fig. 5.11 (a) and the gray part of the breakdown curve in Fig. 5.11 (b) when $t_p<t_p^c$ so $\ell_D<\ell_D^c$) up to a critical pulse width t_p^c. This is, because within their drifting distances ℓ_D the electrons do not encounter enough scattering events, which are necessary for the breakdown. If the pulse width is long enough ($t_p=t_p^c$), the drifting distance of electrons can reach the average distance between the scatterers ℓ_{in} ($\ell_D=\ell_D^c=\ell_{in}$), and the electrons encounter enough scattering events and tunnel between Landau-levels, starting the breakdown process. A further increase of the pulse width (black arrows in Fig. 5.11 (a) and the black part of the breakdown curve in Fig. 5.11 (b) when $\ell_D>\ell_D^c=\ell_{in}$) increases the resistivity causing the system to reach the complete breakdown, marked by a saturation of the resistivity $\langle\rho_{xx}\rangle$ at Hall bars as shown in Fig. 5.11 (b).

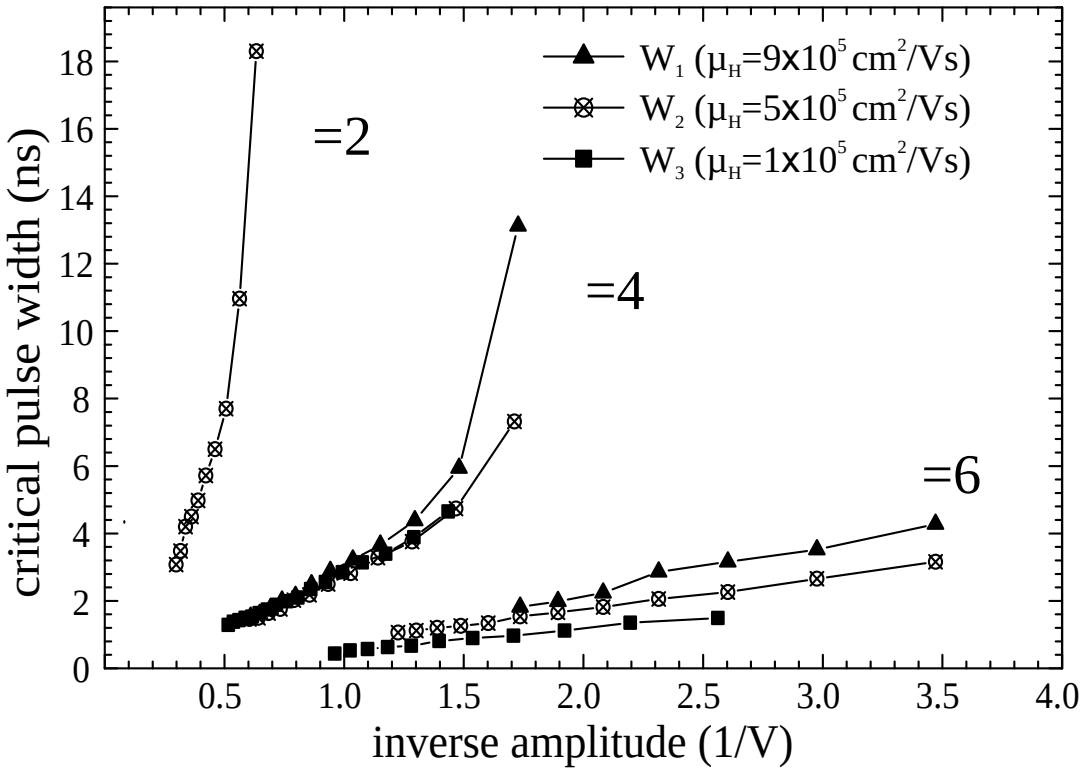

Figure 5.12: Critical pulse width as a function of inverse pulse amplitude. The plots of critical pulse width versus inverse amplitude are shown, which were measured at Hall bar devices with different Hall mobilities (wafers W_1, W_2 and W_3) and at different integer filling factors. The solid lines are just for guiding the eyes.

We can formulate this as follows: within a pulse at integer filling factors, the drift velocity v_D is:

$$v_D = \frac{E_H}{B}, \tag{5.8}$$

where E_H is the Hall field, and B is the magnetic field. Within a critical pulse width t_p^c, the critical drift length ℓ_D^c will be $\ell_D^c = v_D \times t_p^c$. Assuming $E_H = A/w$ for a homogeneous current flow (valid for ρ_{xx}=const$\neq$0, ρ_{xy}=const inside the 2DES, see *e.g.* Ref. [10]), with A being the amplitude, and w being the channel width of the Hall bar, we can formulate the critical pulse width as:

$$t_p^c = \frac{\ell_D^c w B}{A}. \tag{5.9}$$

Therefore we should expect a linear relation between the critical pulse width and the inverse amplitude. In other words, the slope of function t_p^c=f$(1/A)$ should give us the critical drift length ℓ_D^c, as shown in Fig. 5.11 (c).

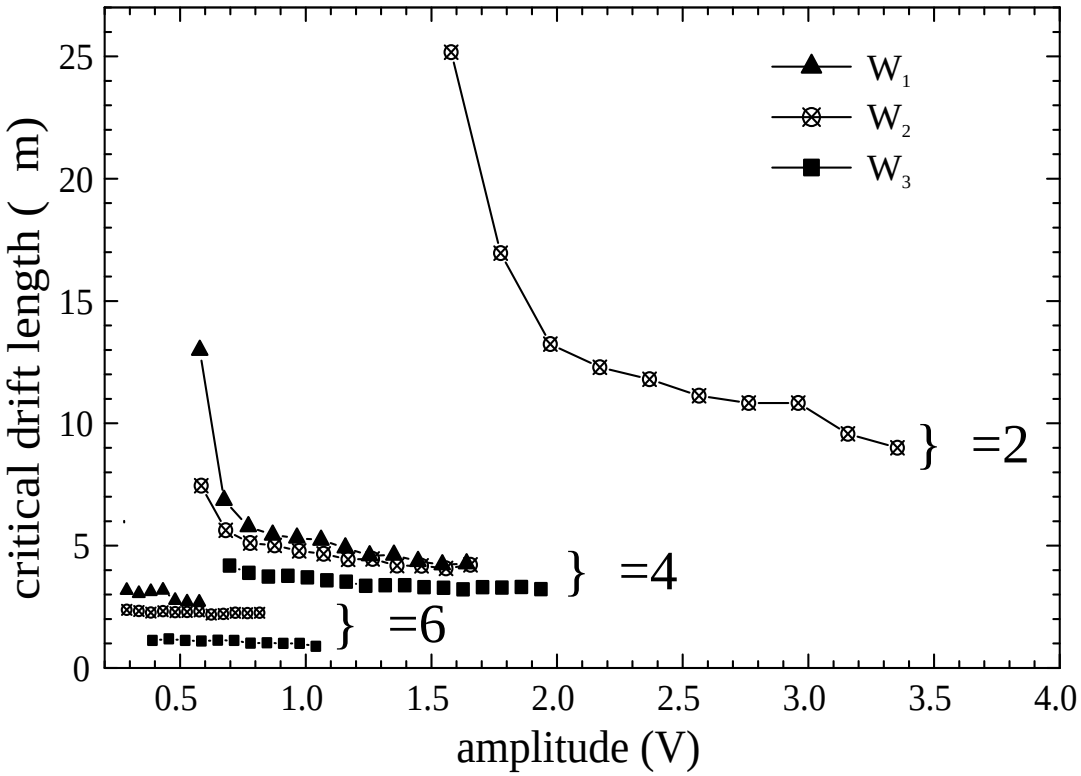

Figure 5.13: Critical drift length as a function of pulse amplitude. The plots of critical drift length versus amplitude are shown, which were measured at Hall bar devices with different Hall mobilities (wafers W_1, W_2 and W_3) and at different integer filling factors. The solid lines are just for guiding the eyes.

This function can be directly obtained from the amplitude dependent pulse-induced breakdown measurements. We have repeated the measurements that are shown in Fig. 5.6 for other integer filling factors and also for wafer W_1. We have determined the critical pulse widths from these measurements and plotted them against the inverse amplitude. Fig. 5.12 shows the critical pulse widths t_p^c,

measured at these Hall bars with different mobilities as a function of the inverse pulse amplitude $1/A$, for filling factors ν=2, 4 and 6. For higher filling factors and for higher amplitudes the expected linearity is almost achieved. Moreover, the lower the mobility is, the closer are the results to this linearity.

The critical pulse width data in Fig. 5.12 can be directly translated into critical drift lengths by using Eq. 5.9. As shown in Fig. 5.13, the critical drift lengths are plotted as a function of amplitude for different filling factors and mobilities. Note that although the curves t_p^c=f$(1/A)$ at ν=4 almost coincide for the samples with mobilities 1×10^5 cm^2/Vs and 5×10^5 cm^2/Vs, the corresponding traces ℓ_D^c=f(A) differ due to the difference in the electron density n_s and the resulting difference in the drift velocity at the QH plateau.

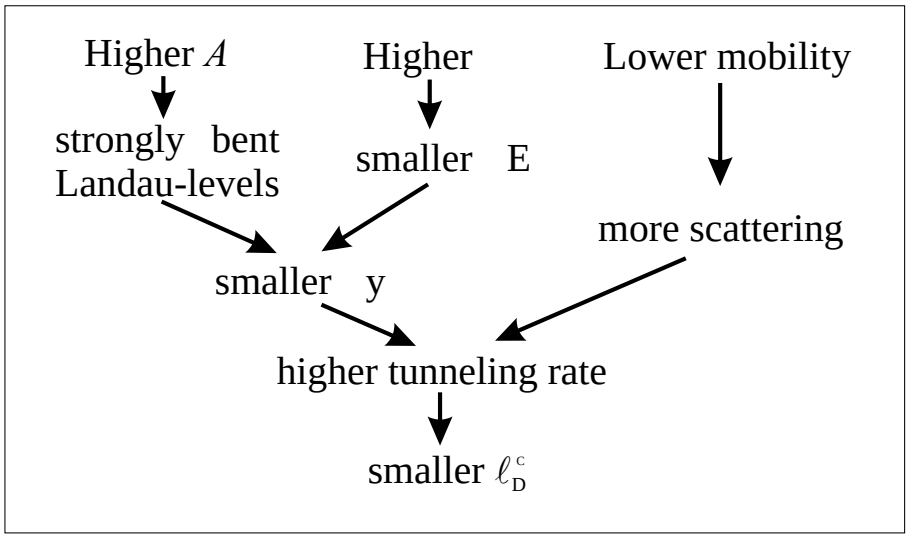

Figure 5.14: Parameters, which decrease the critical drift length ℓ_D^c.

The critical drift lengths are smaller for higher filling factors, because the Landau-level energy gap ΔE=$\hbar\omega_c$-$\Delta E_s \propto B$ ($\hbar\omega_c$ is the cyclotron energy, ΔE_s is the energy of the spin splitting) is smaller at lower magnetic fields, giving rise to a higher tunneling rate $1/\tau_t$ according to Ref. [85]:

$$\frac{1}{\tau_t} \propto \exp\left[-\frac{\Delta y^2}{4\ell_B^2}\right] = \exp\left[-\frac{1}{4\ell_B^2}\left(\frac{\Delta E \cdot w}{eA}\right)^2\right] \tag{5.10}$$

with ℓ_B as the magnetic length. Thus, the breakdown occurs in shorter drifting distances. Similarly, higher amplitudes A, bend the Landau-levels more and decrease the spatial separation Δy between them, causing a higher tunneling rate and a reduction of the role of impurity induced fluctuations, as shown in Fig. 5.11 (d). Lower mobility samples have more scattering centers, so that the tunneling rate between Landau-levels is higher and therefore the critical drift lengths for these samples are shorter. As seen in Fig. 5.13 (b), the mobility

dependence is more pronounced for smaller amplitudes, when the Landau-levels are less bent. All of these discussions are summarized in the diagram in Fig. 5.14.

As the real drift velocities, which depend on the current distribution and the resulting effective width of the current path, $w_{eff} \leq w$, are unknown, the values of ℓ_D^c mark the lower limit for the critical drift distances. However, the parameter dependencies remain valid, as discussed above.

5.6 Discussion

Because of the Coulomb interaction between charge carriers in metallic systems, charge density oscillations (plasmons) can appear. An initial disturbance of the charge density produces an electric field, which causes current to recover the electrical neutrality. Because of the inertia the charge carriers move beyond their equilibrium positions, from which a collective excitation of the system occurs [92]. The properties of plasma oscillations in solid state systems depend on band structure, dimensionality of the system, existence of boundaries and magnetic field (for a review see [93]).

The dispersion relation of plasmons in a 2DES is affected by the dielectric properties of the surrounding medium. In a uniform dielectric medium, the dispersion relation is $\omega_p = \omega_p(k)$ [94]:

$$\omega_p^2 = \frac{n_s e^2}{2\epsilon_r \epsilon_0 m^*} k + \frac{3}{4} v_F^2 k^2, \tag{5.11}$$

where ω_p is the plasmon frequency, k the wave vector, v_F the Fermi velocity, ϵ_0 the permittivity of free space, and ϵ_r is the relative permittivity. In the limit for small k vectors the quadratic term can be neglected, and in a magnetic field the square of the cyclotron frequency should be added [95, 96]:

$$\omega_p^2 = \frac{n_s e^2}{2\epsilon_r \epsilon_0 m^*} k + \left(\frac{eB}{m^*}\right)^2. \tag{5.12}$$

The group velocity of the magnetoplasmons is the derivative of the dispersion relation with respect to the k vector. For small k this becomes

$$v_p = \frac{\delta \omega_p}{\delta k} = \frac{n_s e}{4\epsilon_r \epsilon_0 B}. \tag{5.13}$$

Unlike the drift velocity, the magnetoplasmon velocity in Eq. 5.13 does not depend on the electric field or pulse amplitude. This was also observed in the time-resolved measurements of transport in edge channels, in which the authors have measured the propagation of edge magnetoplasmons by the help of

a box car technique [97, 98]. From a dual pulse generator they have applied a long pulse at a potential probe, which propagated to a second gated potential probe. A large negative bias was applied to this gate, and additionally very short positive pulses were supplied from the dual channel of the same pulse generator. During these short time intervals, the 2DES underneath the gate became conductive, and the integrating capacitance was charged up to the potential existing at the edge of the sample. By varying the delay time between the two pulses, they have measured the arriving time of the edge magnetoplasmons at the second potential probe. The measured time scale was in the range of a few nanoseconds and it depended mostly on the magnetic field B, as it is also seen in the estimation in Eq. 5.13, but not on the pulse amplitude A. However, in our measurements there is a strong dependence of the critical times on the pulse amplitude, which indicates the role of the drift of electrons.

From Eq. 5.13 the velocity of the edge magnetoplasmons can be estimated for the Hall bar fabricated from wafer W_2. The electron density is n_s=2×10^{15} m^{-2}, ϵ_0=$10^7/4\pi c^2$, ϵ_r=13.4 for GaAs, e=1.6×10^{-19} C, and for filling factor ν=2 the magnetic field is 4.2 T. From these the velocity of the magnetoplasmons can be estimated as v_p≈1.6×10^5 m/s, which is about two orders of magnitude bigger than the drift velocity v_D. The distance between the potential probes were 272 μm, so that the time delay t_{del} of a pulse between the two probes becomes t_{del}=272 μm/v_p≈1.7 ns independent of the pulse amplitude. But from Fig. 5.12 the critical pulse widths are between 3 ns and 18 ns, and they do depend on the pulse amplitude.

Another important point is the magnitude of the applied pulses. In the edge magnetoplasmon measurements, the authors applied pulses in the range from -20 mV to 20 mV. These values were about two orders of magnitude smaller than the critical DC values of the QHE breakdown. In our measurements we detected a signal only when the pulses were supercritical. It should be noted that the two setups (ours and the one for magnetplasmon detection) are totally different from each other. In the magnetoplasmon measurements it is possible to detect the pulse by varying the delay times of the gate pulse, with respect to the main pulse. However, in our measurement setup we apply only the main pulse, and measure the average DC signal across the potential probes.

In our pulse-induced breakdown experiments, the subcritical pulses in the QHE plateau (pulses below the critical voltage), which cause the drift of electrons, should also create edge magnetoplasmons. However, neither the drift of electrons nor the edge magnetoplasmons can be detected, because an equal number of pulses (about 10^8) arrive at the potential probes in the measurement time (about 1 second) of the digital voltmeter. Since the voltmeter measures the average potential difference between the potential probes, and since there is no dissipation for subcritical pulses, the signal is zero V_x=0 V. There is a nonzero signal in the QHE plateau, only when supercritical pulses (pulses above the

critical voltage and longer than the critical pulse width) are applied, and this is only because of the dissipation. Because of the same reason mentioned above, the edge magnetoplasmons can not be detected in this case too.

From all these arguments we can conclude that the edge magnetoplasmons can not be detected with our measurement setup, and that the QHE breakdown is mainly dominated by the drift of electrons.

5.7 Summary

To summarize, we have investigated the time scale of the excitation of electrons in 2DES of GaAs/AlGaAs heterostructures at the QHE breakdown. The time-resolved measurements were performed by applying electric pulses to the QH devices with a Hall bar geometry, having different electron mobilities ($1\times10^5\text{cm}^2/\text{Vs}\leq\mu_H\leq9\times10^5\text{cm}^2/\text{Vs}$) and at integer filling factors ν=2, ν=4 and ν=6. The duty cycle of the pulses was held constant, so that the applied average source-drain voltage was also constant. The pulse width and the period of the electrical pulses were simultaneously varied from the nanosecond to the millisecond range.

We have observed that the breakdown starts only after a certain critical pulse width, if the amplitude of the pulses is higher than the critical DC voltage value. These critical times are of the order of nanoseconds, and they depend on the pulse amplitude, magnetic field, and electron mobility. With repeating the measurements for different duty cycles, we have found that the pulse width is the critical parameter but not the period. This means that the pause between the pulses does not play a significant role, at least up to a certain duty cycle value.

The time scale of excitation (0.4-18 ns) is in agreement with an estimation from a previous work by Kawaguchi *et al.* [12]. The authors introduced the concept of a switching time T_s for the electron system to transit from the QHE regime to the dissipative breakdown regime, and estimated that it should be of the order of 10 ns.

From a simple model, which assumes a homogeneous distribution of scatterers and a homogeneous current flow throughout the sample, we obtained the lower limit for the critical drift lengths varying from about 1 μm to 25 μm. We interpret the critical pulse widths as the average drifting times of the electrons between inelastic scattering events causing tunneling between the Landau-levels, and the critical lengths as the average drifting distances related to the inelastic scattering lengths ℓ_{in} of the electrons. Characteristic dependences of these critical drift lengths on the amplitude, filling factor and the mobility have been observed and can be attributed to impurity-assisted inter-Landau-level tunneling.

With our measurement setup it was not possible to detect the edge magnetoplasmons, and because of the strong amplitude dependence of the critical times, we concluded that the QHE breakdown is mainly dominated by the drift of electrons.

6 Time-Resolved Breakdown Measurements at Corbino Devices

The main motivation to repeat the time-resolved breakdown measurements on Corbino devices was to investigate the possible existence of the edge effects at the QHE breakdown. In the Hall bars it is known that the edge can play a dominant role in carrying current in the QHE regime [45, 99], but there is only limited knowledge about the occurrence of edge states in Corbino devices [100, 101, 102]. These states can be different from those of Hall bars, depending on the contact material, due to the fact that the edge states in Hall bars are determined by the depletion zone near the etched boundaries of the sample, whereas in Corbino devices they are defined by the work function of the contact metal. In this chapter time-resolved breakdown measurements on Corbino devices are introduced, and their similarities and differences with Hall bar devices are discussed. At the end there is a section on pulse-induced relaxation measurements on Corbino devices.

6.1 Experimental setup

The Corbino devices discussed in this chapter were fabricated from three different wafers W_3, W_4 and W_5 (see Table 6.1), with different channel widths w=200, 100 and 50 μm (r_1=100 μm, r_2=300, 200 and 150 μm).

	n_s (cm^{-2})	μ_H (cm^2/Vs)
Wafer W_3	2.7×10^{11}	1×10^5
Wafer W_4	2.75×10^{11}	1.3×10^5
Wafer W_5	2.1×10^{11}	2.4×10^5

Table 6.1: Electron density and Hall mobility of the fabricated wafers, from which the Corbino devices were fabricated. The parameters were determined from the transport measurements at 1.5 K.

The experimental setup for the Corbino devices was very similar to the one for Hall bars as shown in Fig. 6.1 [103]. The coaxial cable with the 50 Ω impedance matching resistor was connected in the immediate vicinity of the samples, and rectangular pulses $V_A(t)$, with amplitude A, were applied between the source contact S, and the ground. The pulse width t_p, and the period T, were increased simultaneously, keeping the duty cycle $d.c.=t_p/T$ constant for each measurement curve. This keeps the average applied voltage (and therefore the average ring current within a QH plateau) constant. Since there are no side contacts of Corbino devices, we have only measured the average sample current between source and drain $\langle I_s \rangle$, with another 50 Ω resistor attached in series with the devices (between the drain contact D and the ground). The averaging of the time dependent voltages was performed by using the same kind of digital voltmeters as in the measurements with the Hall bars, with an input time constant t_{in} set to $t_{in} \gg t_p, T$.

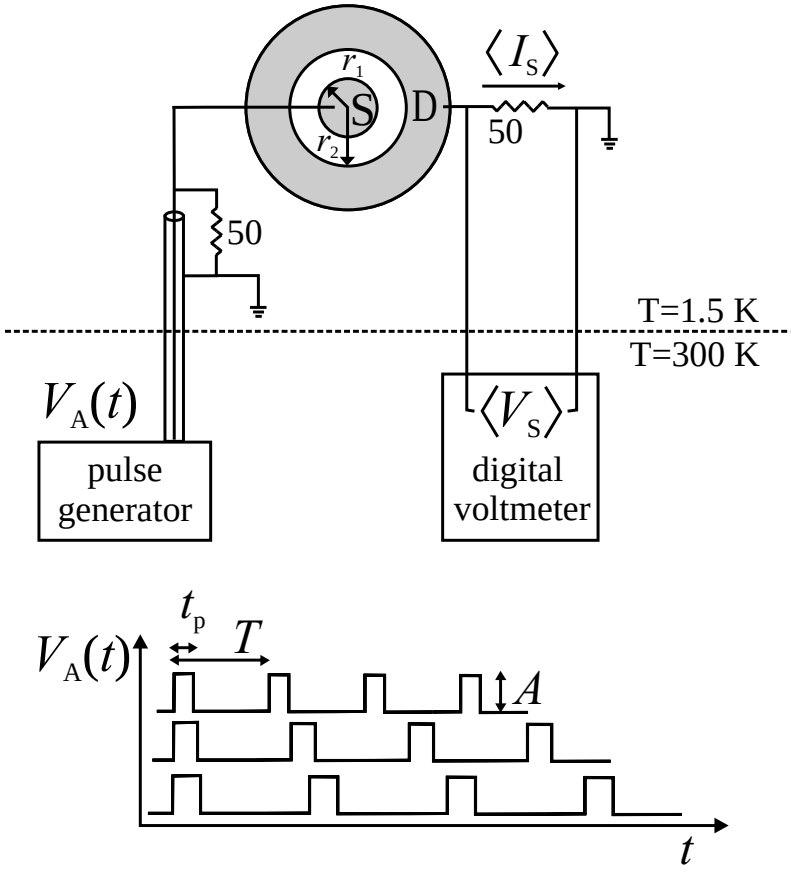

Figure 6.1: Schematic view of the experimental setup to measure the time-resolved pulse-induced breakdown in Corbino devices. Rectangular pulses with constant duty cycle were applied between the source contact S and the ground, and the average longitudinal conductivity $\langle \sigma_{xx} \rangle$ was measured.

At the Corbino devices, the average current passing through the samples $\langle I_s \rangle$ was measured, and the average longitudinal conductance was calculated as:

$$\langle \sigma_{xx} \rangle = \frac{\langle I_s \rangle}{\langle V_{SD} \rangle} \frac{\ln(r_2/r_1)}{2\pi}, \tag{6.1}$$

where $\langle V_{SD} \rangle$ is the average applied voltage between the source and drain contacts, and r_2, r_1 are the outer and inner radii of the Corbino device. The temporal dependence of the time dependent current pulse $I_s(t)$ is implicitly included in the measurements, such that

$$\langle I_s \rangle = \frac{1}{T} \int_0^T I_s(t) dt. \tag{6.2}$$

Therefore the average longitudinal conductivity $\langle \sigma_{xx} \rangle$ is

$$\langle \sigma_{xx} \rangle = \left(\frac{\frac{1}{T} \int_0^T I_s(t) dt}{\langle V_{SD} \rangle} \right) \left(\frac{\ln(r_2/r_1)}{2\pi} \right), \tag{6.3}$$

which does not give us the time dependent pulse response of the sample $\sigma_{xx}(t)$, but a value related to its integral. With this simple experimental setup, we can not monitor the pulse shape in the 2DES, but we can determine the excitation times τ_{exc}. Since we have already performed the test measurements with Hall bars, test measurements on Corbino devices will not be considered here.

6.2 DC measurements

In order to characterize the Corbino devices, we measured the source-drain current I_s as a function of magnetic field B, for fixed DC values of the source-drain voltage V_{SD}. By using these data and the formula Eq. 6.1 we calculated the SdH traces for σ_{xx} of the Corbino devices, from which we determined the electron concentrations n_s and the Hall mobilities μ_H. Fig. 6.2 shows two exemplary traces for σ_{xx} of a Corbino device and for ρ_{xx} of a Hall bar, which were fabricated from the same wafer W_3. Thus, both of the QH devices have the same plateau values of the magnetic field. The SdH signal of the Corbino device has the tendency to decrease with magnetic field B, while the one of the Hall bar has the tendency to increase. The Hall bar data is implemented here for comparison and to show that the measurement setup works equally well for Hall bar and Corbino devices.

Further, it was necessary to determine the breakdown conditions at the integer filling factors, where the critical source-drain voltage V_{SD}^c of the breakdown reaches its maximum value. Several current-voltage (I-V) traces at different magnetic fields were obtained in order to determine the integer filling factor

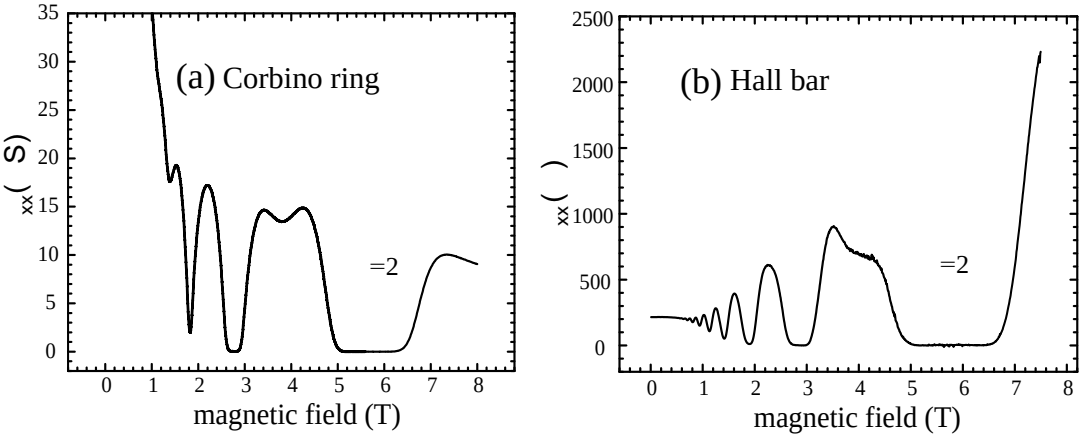

Figure 6.2: Comparison of SdH oscillations between a Corbino device and a Hall bar. Two exemplary SdH traces (a) for σ_{xx} of a Corbino device (w=100 μm) and (b) for ρ_{xx} of a Hall bar (w=272 μm), which were both fabricated from wafer W_3.

positions and the corresponding critical DC voltages V_{SD}^c. Fig. 6.3 (a) shows such an I-V curve of a Corbino device (w=200 μm) fabricated from wafer W_3 at filling factor ν=4. The critical DC voltage is V_{SD}^c=0.57 V for the up-sweep and V_{SD}^c=0.53 V for the down-sweep. At filling factor ν=2 on the other hand, the critical voltages are V_{SD}^c=2.14 V for the up-sweep and V_{SD}^c=1.44 V for the down-sweep, as shown in Fig. 6.3 (c). The occurrence of such a hysteresis in the I-V curves of the QHE breakdown [9, 17] is rather typical and usually attributed to thermal instabilities of the electronic system near the critical point.

6.3 Pulse-induced breakdown of the QHE

In the pulse-induced breakdown measurements on Corbino devices, we have repeated the type of measurements that we have performed on Hall bar samples. In the following subsections the dependences on amplitude, duty cycle, magnetic field, channel width and mobility are shown.

6.3.1 Amplitude and duty cycle dependence

Fig. 6.3 (b) shows the pulse-induced breakdown curves of the Corbino device (DC breakdown shown in Fig. 6.3 (a)) at filling factor ν=4. In case the applied pulses have amplitudes lower than the critical voltages, *e.g.* for the amplitude A=0.5 V, no breakdown is observed. But as the amplitude is increased from 0.5 V to 0.6 V, above the critical voltage, the QHE breakdown is suppressed below a certain critical pulse width, at which the average longitudinal conductivity $\langle\sigma_{xx}\rangle$ starts deviating from its initial $\langle\sigma_{xx}\rangle\approx$0 value. If the amplitude is

increased to higher values, the suppressed breakdown region gets smaller, such that the QHE breaks down at smaller critical pulse widths. For $t_p < t_p^c$ there is a region of the supercritical non-dissipative pulses [104]. As seen from Fig. 6.3 (b) the pulse amplitudes can exceed 1.6 times, and in Fig. 6.3 (d) 1.9 times of the average of the critical voltages, without causing dissipation.

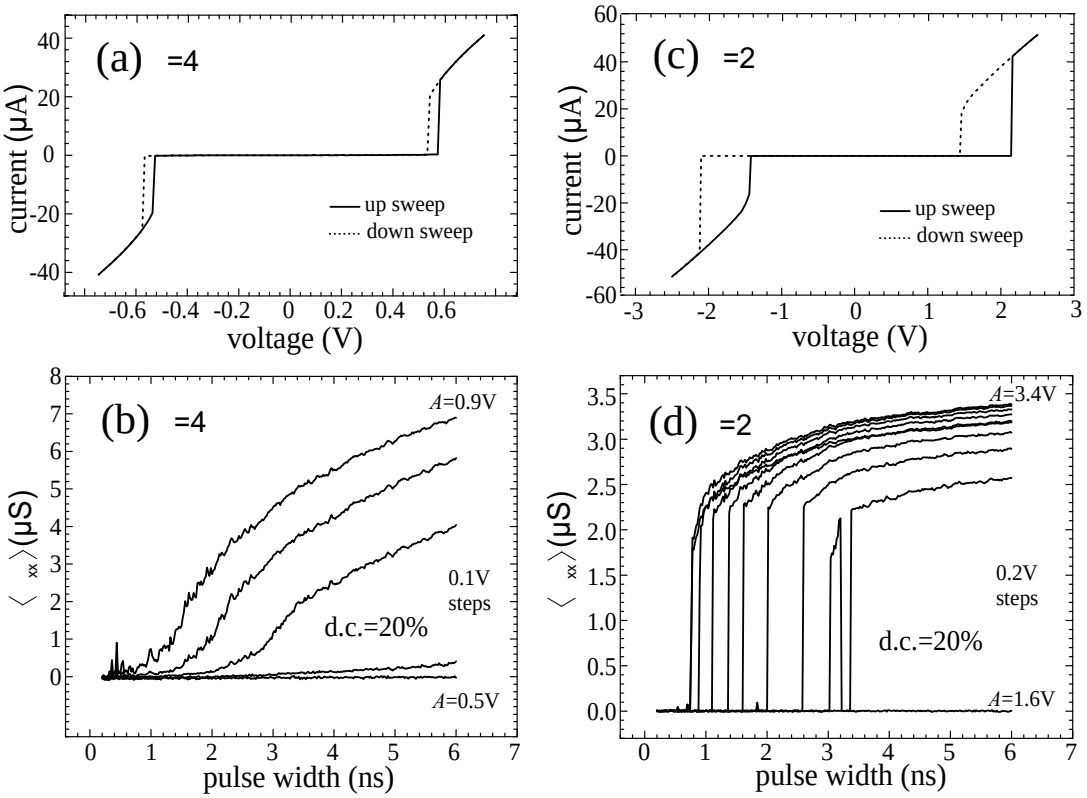

Figure 6.3: I-V curves and amplitude dependent breakdown at a Corbino device. (a) I-V curves at filling factor ν=4. (b) Average longitudinal conductivity $\langle \sigma_{xx} \rangle$ measured as a function of pulse width and pulse amplitude at filling factor ν=4. The breakdown starts when the pulse amplitude A exceeds the critical voltages V_{SD}^c for up and down-sweeps. (c) and (d) are the corresponding curves for ν=2 (Corbino device was fabricated from wafer W_3 with a channel width w=200 μm).

Figs. 6.3 (c) and (d) show the corresponding curves for filling factor ν=2. On the positive voltage side of the I-V curves in Fig. 6.3 (c) the critical voltages are V_{SD}^c=2.14 V for the up-sweep and V_{SD}^c=1.44 V for the down-sweep. But in Fig. 6.3 (d) the QHE breaks down at an amplitude of A=1.8 V, slightly above the average value of these critical voltage values, as if there is no hysteresis. As the same behavior was confirmed at another Corbino device (Fig. 6.12), we have concluded in our publications that the applied pulses average out the hysteresis in the I-V characteristics. But in the later experiments, where we measured

the AC behavior of the hysteresis, we have found evidence that the hysteresis grows with the applied frequency (up to 100 kHz). With the corresponding experimental setup we could not reach the GHz regime, so it is still unclear what happens to the hysteresis when we apply nanosecond pulses.

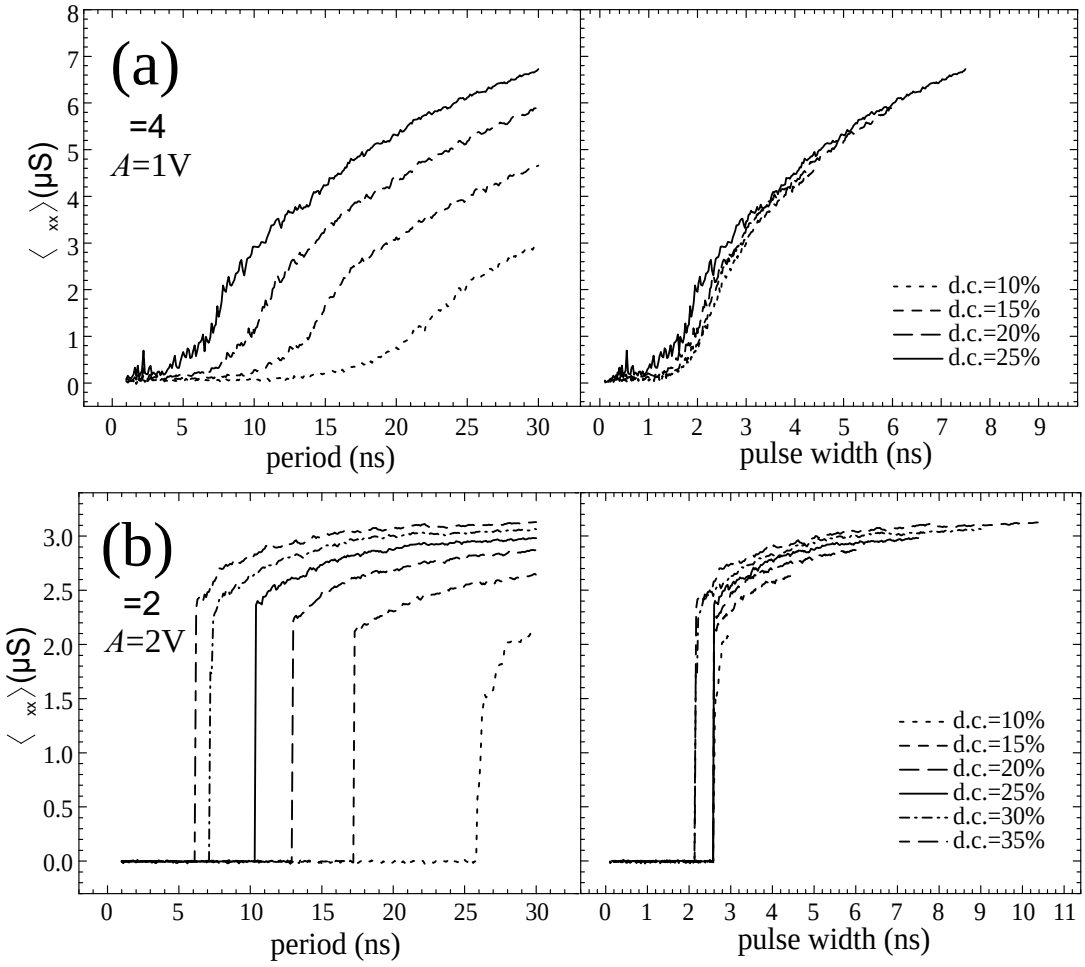

Figure 6.4: Duty cycle dependence of the pulse-induced breakdown at a Corbino device. The QHE breakdown curves plotted as a function of period (on the left) and of the pulse width (on the right) for a constant amplitude with different duty cycles. Both (a) for ν=4 and (b) for ν=2 the breakdown curves almost coincide if they are plotted against the pulse width. This means that the pause between the pulses does not play a significant role (Corbino device was fabricated from wafer W_3 with a channel width w=200 μm).

A possible explanation for this strange behavior may be the ringing in the applied pulses. We do not know (and can not know with our experimental setup) the real pulse shape, which is applied to the QH devices. A possible ringing in the pulse may cause huge potential peaks, which do not cause the QHE breakdown due to their short durations, but which may alternatively reach

the upper critical voltage and then the lower critical voltage. As we can only detect a time-averaged signal, this may lead to an effective averaging of the I-V hysteresis. However, it is unknown how far the hysteresis itself is influenced by the high frequency components of the excitation.

These experiments were performed with a constant duty cycle of 20% (pulse width and pulse period changed simultaneously), so that the average applied voltage $\langle V_A \rangle = A/5$ is much smaller than V_{SD}^c. Therefore the amplitude is the critical parameter for the breakdown but not the average voltage. Moreover, the occurrence of dissipation for pulse widths $t_p > t_p^c$ is not a consequence of the change of the average source-drain voltage (as $\langle V_{SD} \rangle$=constant holds), but of the process during the pulse duration itself. To prove this, we have studied the behavior of the samples for different pulse-to-pause ratios.

Figs. 6.4 (a) and (b) show typical measurements at filling factors $\nu=4$ and $\nu=2$ for different duty cycles (*i.e.* for different average currents). For both filling factors the same breakdown data is plotted as a function of period T and as a function of pulse width t_p. The breakdown curves almost coincide if they are plotted against the pulse width, such that the breakdown starts at the same critical pulse width for different periods (*i.e.* for different average currents and pauses between the pulses). This clearly indicates that the pause between the pulses has no important relevance for duty cycles at least up to 25%. There is no accumulative effect of dissipation as long as the pause between two subsequent pulses is not shorter than a few nanoseconds, indicating a complete relaxation of the pulse-excited electrons back to the QH state on this time scale. Thus, the QHE breakdown is dominated by the excitation process during the pulse only.

In Fig. 6.4 (b) the curves group precisely at certain critical pulse widths t_p^c (for duty cycles 10%-25% at t_p^c=2.58 ns, for 30% and 35% at t_p^c=2.13 ns). Each group of traces may correspond to a certain number and configuration of dissipative current filaments between central and outer electrode, as observed directly by space-resolved photoluminescence measurements in thin-film Corbino devices [107, 108]. The evolution of these few filaments gives rise to a more pronounced dependence of the current distribution on small variations of the boundary conditions. The drift model [103] applies also here, assuming a homogeneous distribution of scatterers and a homogeneous current flow. The critical pulse widths are the average drifting times of the electrons between inelastic scattering events causing tunneling between the Landau-levels. As it was in the Hall bars, the time scale of the excitation (up to a few nanoseconds) is in agreement with the estimation of Kawaguchi *et al.* [12].

6.3.2 Magnetic field dependence

The magnetic field dependences of the $\langle \rho_{xx} \rangle$ vs. t_p and $\langle \sigma_{xx} \rangle$ vs. t_p curves are similar in Hall bar and Corbino devices. If the magnetic field is varied from

its filling factor ν=2 position to higher or to lower values, the QHE breakdown occurs in shorter times and more smoothly. As seen in Fig. 6.5, the closer to the integer filling factor (the dashed line with gray scale) the bigger is the critical pulse width and the more abrupt is the QHE breakdown. This resembles the typical current voltage characteristics of the QHE breakdown, in which the critical current density reaches its maximum value and the breakdown is more abrupt at integer filling factors [9].

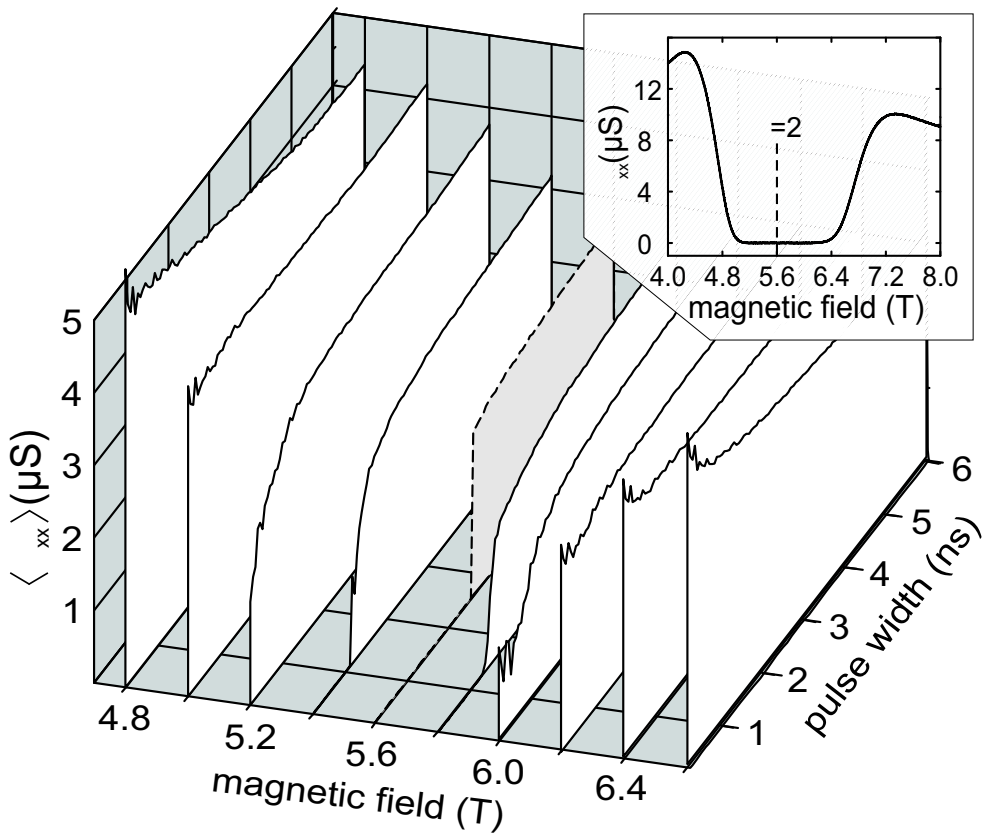

Figure 6.5: The magnetic field dependence of the pulse-induced QHE breakdown at a Corbino device at ν=2. The closer to the integer filling factor (the dashed line with gray scale) the bigger is the critical pulse width and the more abrupt is the breakdown. The inset shows the σ_{xx} around filling factor ν=2 (w=100 μm, wafer W_3).

The behavior in the off-plateau regions is similar as it was in the Hall bar devices. As shown in Fig. 6.5, for the off-plateau values of the magnetic field (B=4.8 T, 6.4 T and 6.6 T) the response of the 2DES is totally different from the in-plateau values (B=5.4 T, 5.6 T and 5.8 T). In the off-plateau curves, the $\langle\sigma_{xx}\rangle$ starts as expected from a nonzero value, decreases down and saturates at a more or less constant value. This decrease is due to electron heating caused by the electrical pulses, which is already discussed in the previous chapter on Hall bar devices.

6.3.3 Channel width dependence

To investigate the width dependence of the pulse-induced QHE breakdown, we have fabricated the Corbino devices with different channel widths w=200, 100 and 50 μm (r_1=100 μm, r_2=300, 200 and 150 μm). All of the three Corbino devices in Fig. 6.6 (a), (b) and (c) were fabricated on the same wafer piece (wafer W_3). The three plots show the measurements which were performed at filling factor ν=2. As it is seen from Fig. 6.6 (a) and (b), the amplitudes have the tendency to scale with the channel width. In Fig. 6.6 (a) the QHE breaks down at 3 ns for A=1.8 V. When the channel width is halved to w=100 μm the breakdown amplitude is also halved. As seen in Fig. 6.6 (b) the QHE breaks down at 3 ns for A=0.9 V.

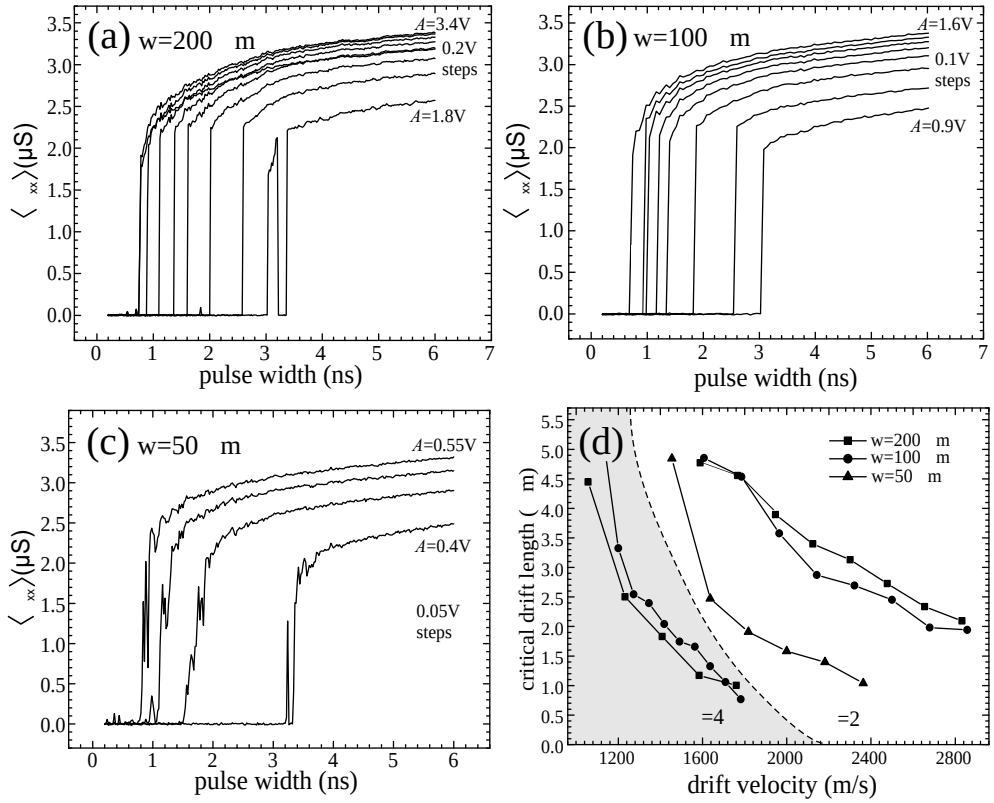

Figure 6.6: Channel width dependence of the pulse-induced breakdown at Corbino devices. Amplitude dependent (d.c.=20%) QHE breakdown at ν=2 on Corbino devices (from wafer W_3) are shown with channel widths of (a) w=200 μm, (b) w=100 μm and (c) w=50 μm. (d) The corresponding critical drift lengths versus drift velocity for different channel widths and filling factors. The curves for w=200 μm and w=100 μm almost coincide supporting our simple drift model. The regions of ν=2 and ν=4 are separated with the dashed line. The data for w=50 μm is missing for ν=4, because QHE was not observed at ν=4.

According to our drift model this is expected, because the Corbino devices were fabricated on the same wafer piece. The impurity properties of the devices, for example the average distance between the impurities ℓ_{in} are the same. Therefore the critical drift lengths ℓ_D^c should also coincide. This implies that the the drift velocities $v_D{=}\ell_D^c/t_p^c{=}A/wB$ (see next paragraph) should be equal to each other, because the critical pulse widths are ($t_p^c{=}3$ ns) the same, and the magnetic field is constant. This explains the scaling of amplitude A with the channel width w. The behavior of the Corbino device with $w{=}50$ μm is qualitatively the same, but it does not scale well enough with the sample width, especially for higher amplitudes. We do not know the main reason for this behavior, but it should be noted that the role of inhomogeneities induced by the impurities (potential fluctuations) should increase for smaller channel widths.

We have repeated the same experiments for filling factor $\nu{=}4$ and obtained the critical times from these measurements. Using the same drift model that we have used for the Hall bars, the critical drift lengths were calculated and plotted as a function of the drift velocity, as seen in Fig. 6.6 (d). The choice of drift velocity as the x-axis instead of amplitude, is because of the scaling of the amplitude with the channel width. We have assumed a linear potential drop from the inner electrode to the outer electrode, so that the equation $v_D{=}A/wB$ holds. This assumption is supported by the potential distribution measurements on Corbino devices by Ahlswede *et al.* [101, 102]. By using a scanning force microscope technique, the authors have measured the Hall potential distribution of two-dimensional electron systems across the channel width for different filling factors. The measurements on Corbino devices have shown that, when the filling factor is a little bigger than the integer values (for example $\nu{=}2.2$) the potential drops mainly at the edges [101, 102]. But at the integer filling factors (at $\nu{=}2$) the potential drop is almost linear from one edge to the other [102].

As seen in Fig. 6.6 (d), the curves for $w{=}100$ μm and $w{=}200$ μm almost coincide for filling factors $\nu{=}2$ and $\nu{=}4$, supporting our drift model. From this coincidence we can also argue that the potential distribution is approximately linear, because the drift lengths scale with the width of the channel. For small amplitudes of $w{=}50$ μm the curve also has the tendency to coincide with the other two curves, but for higher amplitudes there is a considerable difference from the other two curves. As it is already mentioned, this may be because of the increasing role of inhomogeneities for smaller channel widths. The data for $w{=}50$ μm is missing for $\nu{=}4$, because QHE was not observed at $\nu{=}4$.

In Fig. 6.6 (d) for $\nu{=}4$ the critical drift length values vary between 0.7 μm and 5 μm. When we compare these values with the corresponding Hall bar in Fig. 5.13, we see that for wafer W_3 they are between 3 μm and 5 μm for $\nu{=}4$ (for $\nu{=}2$ we do not have the corresponding data in Fig. 5.13). The behavior is qualitatively the same, such that the values of the critical drift length decrease with increasing amplitude (or with increasing drift velocity) and approach a

constant value. But the constant asymptotic values are not so clearly visible in the Corbino measurements as they are in the Hall bar measurements.

6.3.4 Mobility dependence

We have repeated the same pulse-induced breakdown experiments on Corbino devices with the same channel width (w=200 μm), but for different mobilities (wafers W_3, W_4 and W_5) and filling factors (ν=2 and ν=4). The critical pulse widths were extracted from the breakdown curves. By using the same model that we have used for the Hall bars, the critical drift lengths were calculated and plotted as a function of the drift velocity, as seen in Fig. 6.7. Here we have again assumed a linear potential drop from the inner (source) to the outer contact (drain), so that the equation v_D=A/wB holds. In the experiments, the duty cycle was kept constant at d.c.=20%.

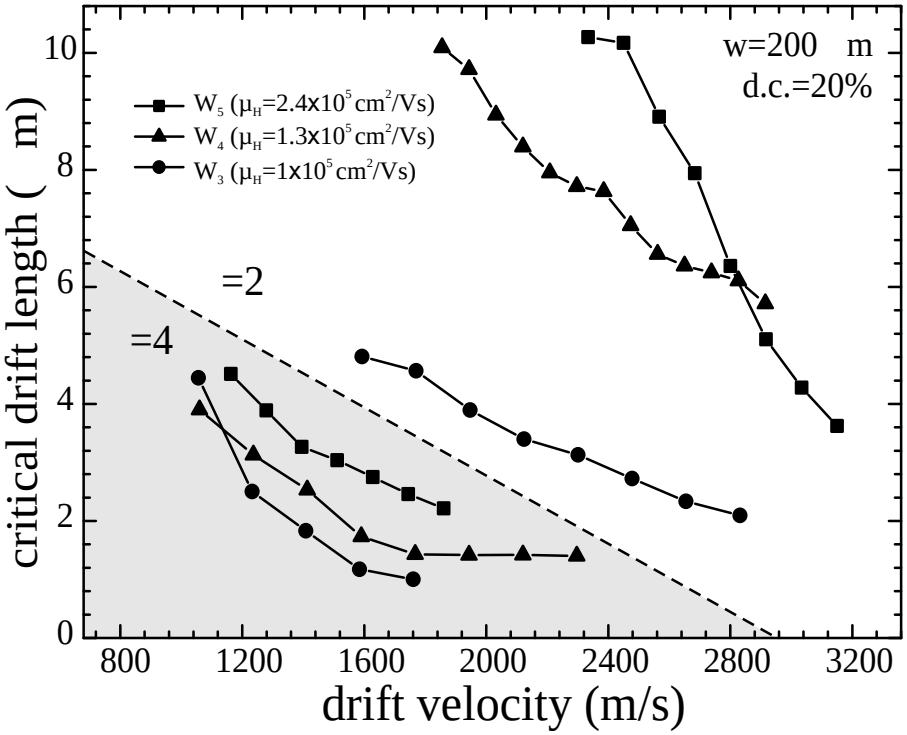

Figure 6.7: Mobility dependence of the pulse-induced breakdown at Corbino devices. The critical drift lengths versus drift velocity are plotted for different mobilities and filling factors. The regions ν=2 and ν=4 are seperated with the dashed line. Channel width (w=200 μm) and the duty cycle (d.c.=20%) are the same for all mobilities.

From Fig. 6.7 it is clearly seen that there is a qualitatively similar mobility dependence as it was found in the Hall bar devices. The critical drift lengths decrease with decreasing mobility. Lower mobility samples have more scattering

centers, so that the tunneling rate between Landau-levels is higher, and therefore the electrons need shorter critical drift lengths necessary for the breakdown.

6.4 Enforced reappearance of QHE (relaxation)

The first relaxation measurements at the breakdown of the quantum Hall effect were performed by Kaya *et al.* [15], as we have already discussed in chapter 4. The authors have arranged the current density in such a way that it was above the critical value in a constriction and was below this value, when the electrons left the constriction and arrived a wider channel. As they monitored the longitudinal resistivity along the drift path of electrons in the wider region, they have observed that the resistivity fell almost exponentially from a saturation value and the QHE was recovered. The supercritical current in the constriction brought the 2DES in the breakdown state, and the subcritical current in the wider region allowed the electrons to relax and brought them in the QHE state. The microscopic mechanism behind the relaxation was the inelastic Coulomb scattering at the impurities. We imitated these space-resolved relaxation measurements by the help of our time-resolved experimental setup [105]. The analog of the constriction was the supercritical pulses and the analog of the wider region was the subcritical background DC level.

We first applied supercritical breakdown pulses to bring the 2DES in the breakdown state. As seen from the plots in Fig. 6.4 (b), the pulse parameters that we chose with A=2 V and t_p=2.6 ns were slightly supercritical ($t_p \geq t_p^c$, $A \geq V_{SD}^c$). We then varied the pause between the pulses for different background DC levels V_{DC}. As seen in Fig. 6.8 (a) there is a monotonous reduction of the conductivity with increasing pause for V_{DC}=0 V. This is expected, because the pulse is kept constant and the pause is increased, so that the average current decreases. Whether there is a complete relaxation (reappearance of QHE) for zero background level, is not known, since pauses longer than 30 ns could not be applied by our pulse generator HP8133A.

But as the background DC level V_{DC} is set to finite, subcritical values ($0 < V_{DC} < V_{SD}^c$), the average conductivity drops abruptly back to $\langle \sigma_{xx} \rangle \approx 0$, such that the QHE appears again. Surprisingly, with increasing background level V_{DC}, the QHE appears at shorter times of the pulse pause, despite the fact that the average current increases with increasing V_{DC}. As in the case of excitation we can also explain this by the scattering rate, which is enhanced by the enforced drift of the hot electrons during the pulse pause. The higher the subcritical V_{DC}, the higher is the drift velocity and therefore the more inelastic scattering events the electrons encounter during the pulse pause, which is necessary for their relaxation. This confirms our interpretation of the excitation [14] and relaxation [15] in QH systems on the basis of the drift model, explaining both processes by impurity-induced inter-Landau-level transitions.

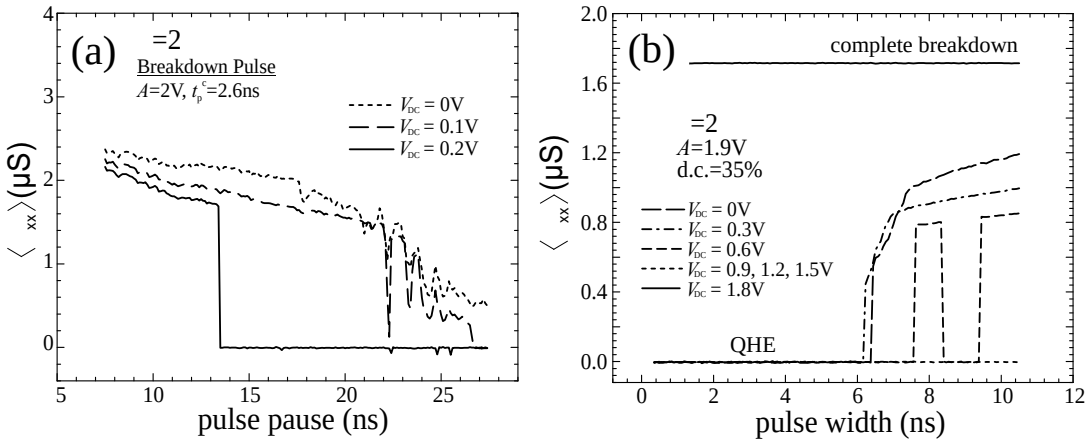

Figure 6.8: The relaxation of the 2DES from the dissipative to the quantum Hall state. (a) The relaxation of the 2DES from the dissipative to the QH state is observed by varying the pause between the pulses, and the background DC level V_{DC}. (b) The relaxation of the 2DES from the dissipative to the QH state by keeping the duty cycle constant, and varying the background DC level V_{DC}. As the background DC level V_{DC} is increased to 0.9 V, the breakdown of the QHE disappears, at least for the specified time window (device was fabricated from wafer W_4).

Since the pulse width was kept constant in these measurements and the pulse pause was increased, the average source and drain voltage $\langle V_{SD} \rangle$ decreases for each curve in Fig. 6.8 (a). Therefore, one can argue that this decrease in average applied voltage $\langle V_{SD} \rangle$ causes the reappearance of the QHE. To verify this point we performed a control experiment, in which we kept the average applied source-drain voltage constant and varied the background DC level as we did previously. Fig. 6.8 (b) shows the results of this experiment, where the duty cycle (d.c.=35%) and the amplitude (A=1.9 V) are constant for each measurement curve, just like the previous excitation experiments but with the variation of the V_{DC} value.

The curve for V_{DC}=0 V is the usual pulse-induced breakdown curve, with its QHE, abrupt breakdown and saturation regions. But as V_{DC} is increased from 0 V to 0.3 V the conductivity of the saturation region decreases. When the background DC level is 0.6 V the 2DES becomes unstable with abrupt jumps between the dissipative and the QH states, and the conductivity of the saturation region decreases further. However as the background DC level V_{DC} is increased to 0.9 V, the breakdown of the QHE disappears, at least for the specified time window. This is very interesting, because the reappearance of the QHE occurs, as we increase the average applied voltage by increasing the background DC level. This is another evidence that the average current is not the critical parameter for the QHE breakdown. Similarly for V_{DC}=1.2 V and

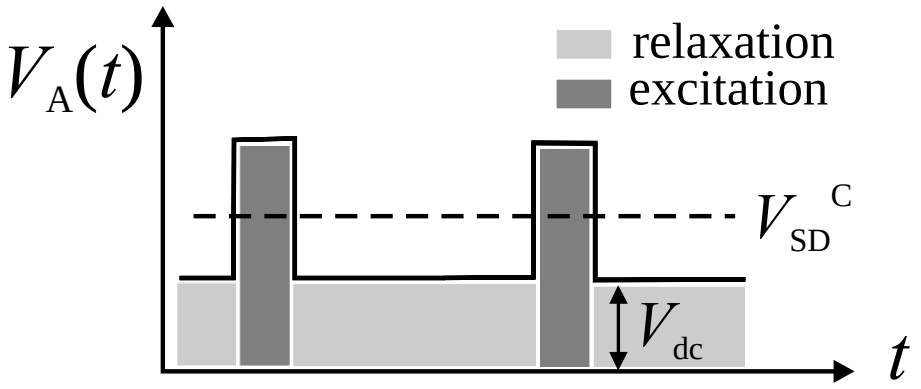

Figure 6.9: The supercritical pulses for (excitation) and the subcritical DC voltage (relaxation). As long as the average source-drain voltage is smaller than the critical voltage, the supercritical pulse causes the excitation and the subcritical DC voltage causes the relaxation for the electrons. Depending on the competition between these two processes and the density of scatterers, the two-dimensional electron system is either in the quantum Hall or in the dissipative state.

1.5 V the electron system stays in the QH state, but a further increase of the background level to 1.8 V results in complete breakdown, since this value is above the critical voltage.

From these experiments in Fig. 6.8 (b), it is confirmed that the decrease in the average applied voltage $\langle V_{SD} \rangle$ can not be the only reason for the relaxation and the reappearance of the QHE in Fig. 6.8 (a). It is clear that the impurities again play the essential role here as it was shown in the space-resolved relaxation measurements [15]. As long as $\langle V_{SD} \rangle < V_{SD}^c$, the supercritical pulse causes the excitation and the subcritical DC voltage causes the relaxation for the electrons (see Fig. 6.9). Depending on the competition between these two processes and the density of impurities, the two-dimensional electron system is either in the quantum Hall or in the dissipative state.

In experiments with Corbino devices we also investigated the relation between the excitation times τ_{exc} and relaxation times τ_{rel} of the breakdown of the quantum Hall effect with zero background voltage level at filling factor ν=2. First we repeated the pulse-induced breakdown measurements on a Corbino device fabricated from wafer W_3 with a channel width of w=200 μm. As we already discussed in the previous chapters, the increase of the duty cycle up to 35% did not affect the breakdown conditions, and the QHE persisted. It is clear that if the duty cycle is further increased, so that the duration of the pause between the pulses becomes shorter and shorter, at some point no QHE should be observed (complete breakdown), because the electrons can not have the necessary time to relax. The duty cycle value at this complete breakdown condition should then give us the relation between the excitation time τ_{exc} and the relaxation time τ_{rel}.

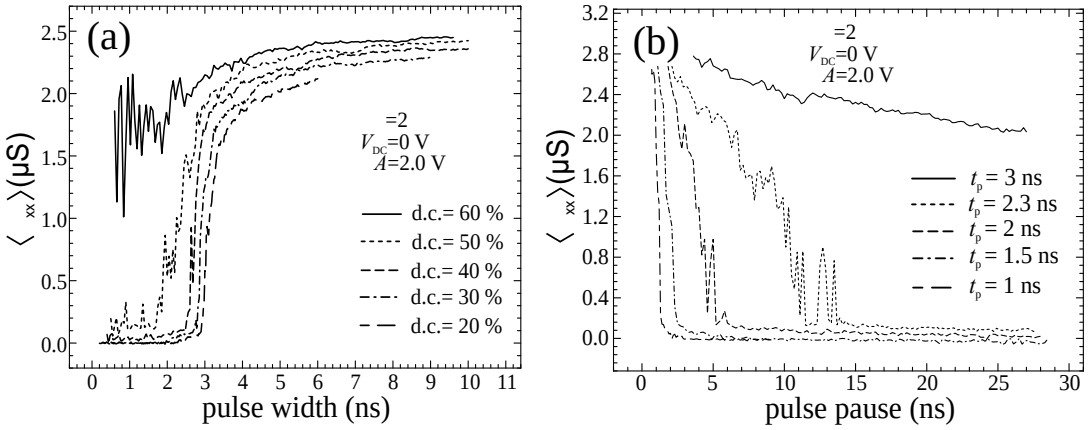

Figure 6.10: The relaxation times of the breakdown of the quantum Hall effect. (a) Pulse-induced breakdown measurements on a Corbino device by varying the duty cycle. The duty cycle value, at which complete breakdown occurs, gives the relation between τ_{exc} and τ_{rel}. (b) Supercritical pulses with different pulse widths are applied and the pulse pause is varied (w=200 μm, wafer W_3).

As shown in Fig. 6.10 (a), we increased the the duty cycle and found that up to d.c.=40% the critical pulse width t_p^c decreases slightly. At d.c.=50% the critical pulse width is still noticeable but at d.c.=60% there is complete breakdown. Since at d.c.=50% there is no complete breakdown, we conclude that the values for τ_{exc} and τ_{rel} are very close to each other ($\tau_{exc} \approx \tau_{rel}$).

In another experiment we applied supercritical pulses with different pulse widths, which were smaller and bigger than the critical pulse width t_p^c=2.1 ns. We then varied the pause of the pulses starting from the smallest value, which could be applied by the pulse generator. This brought the 2DES in the breakdown state, because the starting value of the pause was very short, and the amplitude was supercritical. As we increased the pulse pause (by increasing the period and keeping the pulse width constant), we monitored the relaxation of the longitudinal conductivity. As seen in Fig. 6.10 (b), for the pulse width t_p=3 ns, there is no QHE for the specified range of the pulse pause.

For t_p=2.3 ns the system relaxes at around the pulse pause t_{pau}=12 ns. As t_p is decreased to t_p=2 ns, t_{pau} becomes t_{pau}=6 ns, and for t_p=1.5 ns it becomes t_{pau}=2.5 ns. Finally for t_p=1 ns t_{pau} is slightly larger than 1 ns approaching the limit t_p=t_{pau}. We interpret t_p and t_{pau} as τ_{exc} and τ_{rel} respectively. Therefore from these experimental findings we conclude that $\tau_{exc} \leq \tau_{rel}$. However, as it was discussed in chapter 4, Güven *et al.* have found from general thermodynamic arguments that the relaxation rate cannot be smaller than the excitation rate to the higher level, which means $\tau_{exc} \geq \tau_{rel}$. But they have obtained the best results for τ_{exc}=τ_{rel}. Therefore this is the only condition that fits to our experimental findings and is thermodinamically allowed.

6.5 Discussion

From the time-resolved breakdown measurements, we have found that the breakdown behavior of the Hall bars and the Corbino devices were qualitatively similar at filling factor ν=4, but the Corbino devices with low mobilities revealed interesting differences at ν=2. As already seen in Fig. 6.4 (b) the breakdown for the Corbino device is very abrupt at filling factor ν=2, and the QHE region is very stable (almost without any noise in the σ_{xx} signal), unlike the Hall bar and Corbino devices at filling factor ν=4. This difference may be caused by the edge effects [45, 99] in the QH devices. The knowledge about the occurrence of edge states in Corbino devices [100, 101, 102] is limited. However the edge states in Corbino devices can be different from those of Hall bars. Because the edge states in Corbino devices are defined by the work function of the contact metal, whereas in Hall bars they are determined by the depletion zone near the etched boundaries of the sample. Depending on the work function of the metal with respect to the 2DES, different boundary zones between 2DES and metal, ranging from depletion to accumulation zones, are possible.

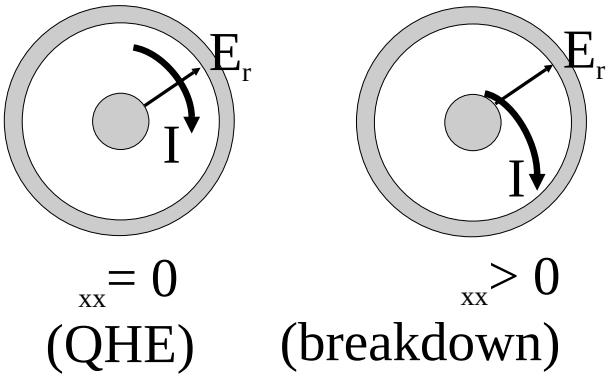

Figure 6.11: Current filament formation in Corbino devices at the pulse-induced breakdown. Local fluctuations of the edge potential [101, 106] could serve as the starting point for dissipative current filaments (see *e.g.* [107, 108]).

A finite value of either ρ_{xx} in the Hall bar or of σ_{xx} in the Corbino device near the breakdown corresponds to an exchange of charges between the edges (or contacts) via the 2D bulk. At higher filling factors (lower magnetic fields), this process seems to be rather similar in Hall bars and Corbino devices, due to smaller Landau energy gaps and correspondingly higher tunneling probabilities for inter-Landau-level transitions. At smaller filling factors (higher magnetic fields) this tunneling probability decreases, and the breakdown may be stronger depending on the local properties of the sample edge. Local fluctuations of the edge potential [101, 106] could serve as the starting point for dissipative current filaments as shown in Fig. 6.11 (see *e.g.* [107, 108]). The evolution of such filaments is a highly nonlinear phenomenon, *i.e.* small variations of the bound-

ary conditions lead to drastic changes of the resulting current distribution. The corresponding difference of the breakdown behavior of Hall bars and Corbino devices is however not completely understood yet.

Another difference was observed in the duty cycle dependence of the Corbino devices at ν=2. In Fig. 6.12 the breakdown curves are plotted as a function of the period (on the left) and as a function of the pulse width (on the right). These curves also almost coincide if they are plotted against the pulse width, but in a different manner. Some curves coincide exactly at certain critical pulse widths t_p^c. For example, the curves with duty cycles 25% and 30% coincide exactly at t_p^c=2.1 ns, while the curves with 10% and 20% coincide at t_p^c=2.55 ns. The curve with 15% duty cycle on the other hand breaks down at t_p^c=2.4 ns (see also Fig. 6.4 (b) for a wider sample from the same wafer). These jump-like changes of the critical pulse widths are one of the nonlinear effects, which we observed at Corbino devices at filling factor ν=2.

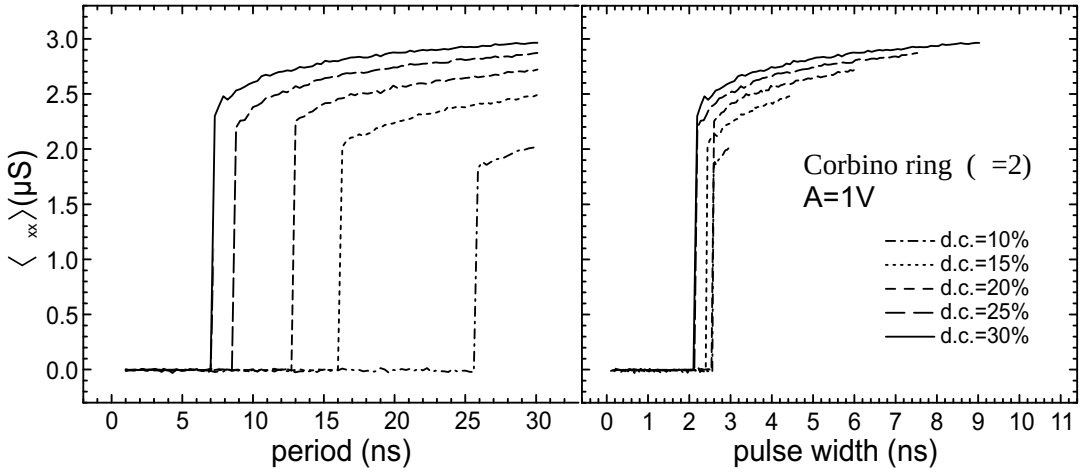

Figure 6.12: Pulse-induced breakdown measurements at Corbino devices at filling factor ν=2. The QHE breakdown curves are plotted as a function of the period (on the left) and of the pulse width (on the right) for a constant amplitude with different duty cycles (w=100 μm, wafer W_3).

The observed hysteresis in the I-V curves is more pronounced for ν=2 in comparison to ν=4. We attribute this to the higher energy gap between the Landau levels, giving rise to a reduced tunneling probability and a reduced number of dissipative current filaments. The evolution of these few filaments gives rise to a stronger pronounced dependence of the current distribution on small variations of the boundary conditions, which can also depend on the polarity of the electric field between the current contacts. Thus, the topology of the filaments cannot be assumed to be identical for both bias polarities. At lower magnetic fields (higher filling factors), more dense networks of current paths are developed, leading to smoother I-V curves and less hysteresis or asymmetry.

The critical pulse widths in Corbino devices, show in comparison with Hall bars, in general a similar behavior on the parameters as pulse amplitude and filling factor. However, a discussion of these parameter dependences cannot be based on similarly simplistic assumptions as in the case of Hall bar devices. This is, because even in the simplest case of a homogeneous 2DES (σ_{xx}, σ_{xy} constant throughout the system), the potential distribution is nonlinear. The electric field is highest near the inner electrode, giving rise to the highest local drift velocities. This should lead to an onset of dissipation near the inner electrode. When the breakdown of the QHE occurs, one or more current-carrying filaments may propagate from the inner to the outer electrode, leading to a nonzero source-drain current. A similar behavior has been observed in thin-film Corbino devices, prepared on n-doped GaAs [107, 108]. There are some indications of the formation of filaments at the breakdown of the QHE in our Corbino devices:

1. If the evolution of $\langle\sigma_{xx}\rangle$ is plotted as a function of the pulse width, a distinct difference in the behavior compared to Hall bars is observed. At ν=2, the $\langle\sigma_{xx}\rangle$(t)- curves of the Corbino devices do not exactly coincide for different duty cycles t_p/T, but group in certain intervals of t_p/T. Within one group of traces, t_p^c is precisely identical, and the transition from QH to dissipative conduction is abrupt, in contrast to Hall bars. Thus, each group of traces may correspond to a certain number and configuration of dissipative current filaments between central and outer electrode, as observed directly by space-resolved photoluminescence in thin-film Corbino devices [107, 108]. The small values of $\langle\sigma_{xx}\rangle\approx$0 before the breakdown and the steepness of the transition at ν=2 indicate that the Corbino device is a very effective insulator in the QH state until a very sudden onset of dissipation. The origin of this behavior is not yet completely understood.

2. Some of the $\langle\sigma_{xx}\rangle$(t) - traces show more than one switching point: not only for subsequent increase and decrease of the pulse width (hysteresis), but also within single traces, subsequent switching from the QH to the dissipative state and back were observed when changing the pulse width t_p. This may reflect the instability of the dissipative current filaments, due to the strong nonlinearity of the QH breakdown. However, at smaller magnetic fields (i.e. at ν=4), the above mentioned effects disappear, and the overall behavior of both Corbino and Hall bar devices tends to be very similar (both $\langle\sigma_{xx}\rangle$ and $\langle\rho_{xx}\rangle$ have small, but nonzero values even for small excitation).

6.6 Summary

To summarize, we have investigated the suppressed breakdown and the reappearance of the QHE in 2DES of GaAs/AlGaAs heterostructures in Corbino devices. The measurements were performed by applying short electric pulses with either constant duty cycle or constant pulse width, but with different background voltage levels. The QHE breakdown is suppressed below a certain critical pulse width, although the amplitude of the pulses is higher than the critical DC voltage. In this region of the supercritical nondissipative pulses, the pulse amplitudes can be larger than the double amount of the average of the critical voltages, without causing dissipation. The critical times are of the order of a few nanoseconds in agreement with the previous estimations. We interpret these critical pulse widths as the average drifting times of the electrons between inelastic scattering events causing tunneling between the Landau-levels.

No general differences of the response to short electric pulses have been found between Hall bars and Corbino devices. The only deviations were observed in the behavior of the Corbino devices at filling factor ν=2 with their almost perfect QHE conditions and abrupt breakdown profiles, and with the jumps and bunching effects in the critical pulse widths. We believe that these effects are due to the different kind of edge states in the Corbino devices, in comparison to Hall bars.

Setting simultaneously the pulse width to $t_p \geq t_p^c$ and the pulse amplitude to $A \geq V_{SD}^c$, we studied the relaxation of the 2DES from the dissipative to the QH state by varying the pause between the pulses, and the background DC level V_{DC}. A monotonous reduction of the conductivity with increasing pause was found for V_{DC}=0 V. This behavior changes drastically, if V_{DC} is set to finite, subcritical values of $0 < V_{DC} < V_{SD}^c$. In this case, the average conductivity drops abruptly back to $\langle \sigma_{xx} \rangle \approx 0$ (reappearance of the QHE) at markedly reduced relaxation times, which decrease with increasing V_{DC}. In a similar experiment we kept the duty cycle and the supercritical amplitude constant and varied the background DC level. As V_{DC} was set in between a certain subcritical DC voltage range, the pulse-induced breakdown totally disappeared, at least for the specified time window. We attribute all these observations to a scattering rate, which is enhanced by the enforced drift of the hot electrons during the pulse pause. The higher the subcritical V_{DC}, the higher is the drift velocity and therefore the more inelastic scattering events the electrons encounter during the pulse pause. This confirms our interpretation of the excitation and relaxation in QH systems on the basis of a drift model, explaining both processes by impurity-induced inter-Landau-level transitions.

Repeating the pulse-induced breakdown measurements on a Corbino device for duty cycles up to 60%, we investigated the relation between the excitation times τ_{exc} and relaxation times τ_{rel} of the breakdown of the quantum Hall effect. At

d.c.=50% the QHE was still observed, but at d.c.=60% there was complete breakdown, indicating that the values for τ_{exc} and τ_{rel} are very close to each other ($\tau_{exc} \approx \tau_{rel}$). In another experiment we applied pulses with supercritical amplitudes with pulse widths either smaller or bigger than the critical pulse width. By keeping the pulse width t_p constant we increased the duration of the pulse pause t_{pau} and monitored the transition from the breakdown to the QH state. From the experimental findings we found that $t_p < t_{pau}$, but as t_p was made smaller the limit $t_p = t_{pau}$ was approached. We interpreted the pulse width t_p as the excitation time τ_{exc} and the pulse pause t_{pau} as the relaxation time τ_{rel}. Güven *et al.* have found from general thermodynamic arguments that $\tau_{exc} \geq \tau_{rel}$. They obtained the best results for $\tau_{exc} = \tau_{rel}$, which was the only condition that fitted to our experimental findings and was thermodinamically allowed.

7 Relaxation Oscillator Based on a Bistable Corbino Device

In this chapter a simple relaxation oscillator based on a quantum-Hall device with Corbino geometry near the breakdown of the quantum Hall effect is presented. In the hysteresis region of the breakdown, the quantum Hall device behaves bistable. If a resistance is connected in series and a capacitor in parallel to the quantum Hall device, the bistable switching leads to subsequent charging and discharging of the capacitor, detectable as relaxation oscillations. We explain the observed oscillations by solving Kirchhoff's equations and obtain a good quantitative description of the experiment. From this, we deduce some dynamical parameters of the Corbino device and discuss the performance limits of the oscillator.

Various nonlinear electronic devices have been applied for the generation of anharmonic electrical oscillations for a long time, for example the use of discharge tubes by Van der Pol and Van der Mark in 1927 [109]. The study of such systems is interesting not only from a fundamental point of view [110] (for the understanding of nonlinear phenomena, anharmonic oscillators and chaos), but also because of applicative aspects. In particular, high-frequency signal generation and processing is of increasing importance with the development of communication technologies, data processing and optoelectronics. The essential feature of a nonlinear electronic device used for the generation of anharmonic oscillations is its negative differential resistance (a typical example is the resonant tunneling diode, see for example Ref. [111]). Similarly, the instable behavior of devices showing the quantum Hall effect near the breakdown of the QHE was suggested to be used to generate anharmonic oscillations [112].

7.1 Experimental setup and function principle

In this chapter, we present a relaxation oscillator based on the bistable switching of a QH-device with Corbino geometry [113]. Such a device shows an almost ideal insulating behavior in the QH regime until a certain, critical value V_{max} of the source-drain voltage V_{SD}. At V_{max}, a sudden onset of the source-drain current I_{SD} occurs. A subsequent reduction of V_{SD} leads to sudden interrupt

of I_{SD} at another critical voltage V_{min} (V_{min}<V_{max}). In the hysteresis region V_{min}<V_{SD}<V_{max}, the QH device behaves bistable. If a resistance is connected in series and a capacitor as accumulating device in parallel to the QH device, the bistable switching leads to subsequent charging and discharging of the capacitor, detectable as relaxation oscillations. To explain the observed oscillations, Kirchhoff's equations of the circuitry were solved, and a good quantitative agreement with the experiment was obtained. The model allows to calculate the dependence of the oscillation frequency on the driving voltage and the circuit parameters. From this, we are able to deduce dynamical parameters of the Corbino device and to discuss the possible limits (for example the frequency limit) of the oscillator.

We have patterned the Corbino devices from wafer W_3 (channel width w=200 μm) with an electron density of n_s=2.7 $\times$ 10^{11} cm^{-2} and a Hall mobility of μ_H=1$\times$$10^5$ cm^2/Vs. The sample properties n_s and μ_H were deduced from Shubnikov-de Haas-oscillations (Fig. 7.1) and the QHE-breakdown properties from the I-V characteristics (source-drain current I_{SD} versus source-drain voltage V_{SD}, see inset of Fig. 7.1). From the inset of Fig. 7.1, the hysteresis of the QHE-breakdown with respect to the critical source-drain voltage is clearly visible. The corresponding bistable region of the I-V curve is exploited for our oscillator.

The scheme of the oscillator circuit and the function principle are sketched in Fig. 7.2 (a) and (b). The total capacitance (capacitor C_T) is charged via the serial resistor R_V, until the breakdown voltage V_{max} (up sweep) is reached. During this process, the Corbino device is insulating and acts like an open switch. The voltage V_{max} closes the switch, and C_T starts to discharge via the Corbino device, which has now a finite resistance R_{CB}. This process endures until the voltage falls to V_{min}, at which the Corbino device becomes insulating again. Thus, the oscillation amplitude ΔV is determined by the hysteresis, ΔV=V_{max}-V_{min}. From Fig. 7.2 (b), it can be seen that there is a certain range for the choice of the driving voltage V_0 and the serial resistor R_V to keep the oscillator inside the working regime.

For the operation of the relaxation oscillator, there are two main conditions:

(a) the current through R_V for the Corbino device being at V_{min} must not exceed the limit I_c^{min}=V_{min}/R_{CB} (for V_0-$V_{min}$$\geq$$R_V \times I_c^{min}$, a stable solution exists on the resistive branch of the I-V curve of the QH-device, corresponding to a stationary state without oscillations),

(b) the driving voltage must be V_0>V_{max}.

From the conditions (a) and (b), it can be concluded that the lower limit for the serial resistance value is R_V>$\Delta V/I_c^{min}$. Once R_V is chosen, the choice determines the operational range for the driving voltage V_0 according to condition (a):

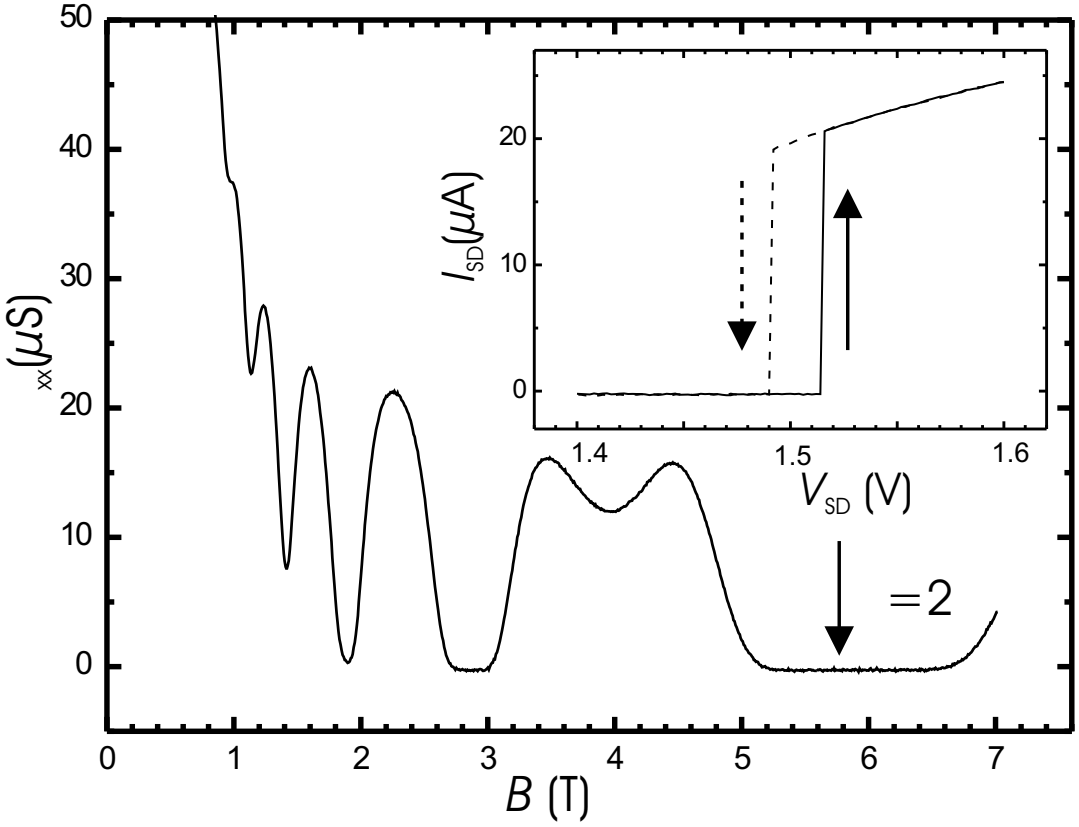

Figure 7.1: Shubnikov-de Haas oscillations and I-V curves of the Corbino oscillator. Shubnikov-de Haas oscillations (DC-measurement of $\sigma_{xx}(B)$ at V_{SD}=100 mV) of the Corbino device is plotted. Inset: Current-voltage characteristics of the Corbino sample (wafer W_3, w=200 μm) at B=5.7 T (ν=2).

$$\frac{V_0 - V_{min}}{R_V} < \frac{V_{min}}{R_{CB}}, \tag{7.1}$$

thus

$$V_{max} < V_0 < V_{min}\frac{R_{CB} + R_V}{R_{CB}} \tag{7.2}$$

The time constants τ_{up} and τ_{down}, as well as the voltage V_{SD} at the Corbino device, for the charging and discharging processes can be determined from the solutions of Kirchhoff's equations with an open switch and R_{CB}, respectively [113]. This yields (akin to the results for relaxation oscillators based on tunnel diode circuits [114]):

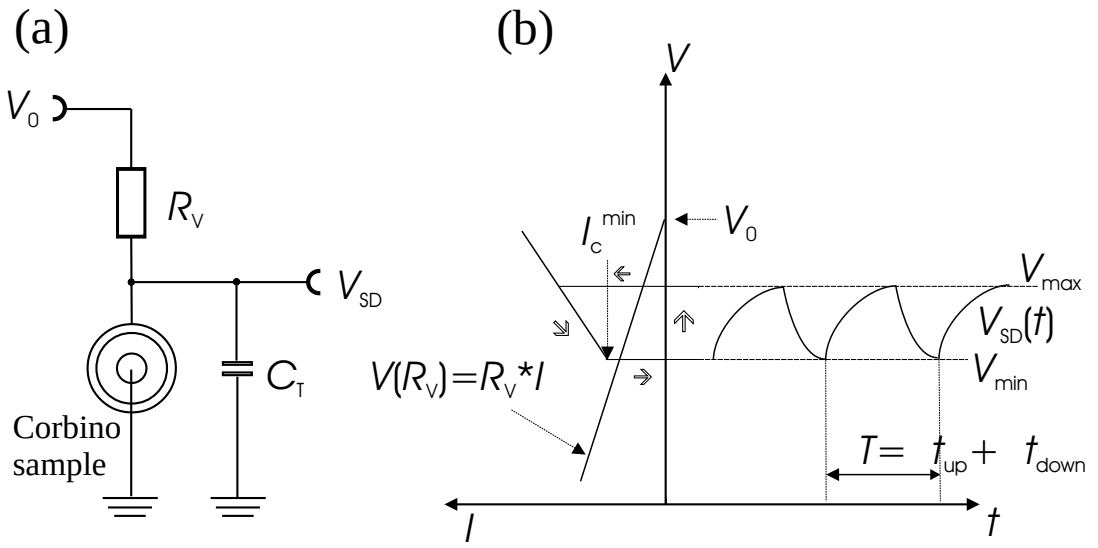

Figure 7.2: Experimental setup and function principle of an oscillator based on a Corbino device. (a) Scheme of the oscillator circuit. R_V is the serial resistance, C_T is the total capacitance of the circuit. (b) Function principle of the oscillator. For an appropriate choice of R_V and the driving voltage V_0, oscillations of the voltage V_{SD} at the Corbino device occur between the dynamical hysteresis limits V_{min} and V_{max}.

$$V_{SD}(t) = V_0 - (V_0 - V_{min}) \exp\left(-\frac{t}{\tau_{up}}\right), \tag{7.3}$$

with τ_{up}=$R_V C_T$ for the charging, and

$$V_{SD}(t) = V_{max} \exp\left(-\frac{t}{\tau_{down}}\right) + V_0 \frac{R_{CB}}{R_{CB} + R_V} \left[1 - \exp\left(-\frac{t}{\tau_{down}}\right)\right], \tag{7.4}$$

with τ_{down}=$\frac{R_{CB}R_V}{R_{CB}+R_V} C_T$ for the discharging, where R_V and R_{CB} act as parallel resistors. The oscillation period T=Δt_{up}+Δt_{down} is not only determined by t_{up} and t_{down}, but also by the hysteresis limits V_{max} and V_{min}, and by the driving voltage V_0:

$$T = \tau_{up} \ln\left(\frac{V_0 - V_{min}}{V_0 - V_{max}}\right) + \tau_{down} \ln\left(\frac{V_{max} - \Theta V_0}{V_{min} - \Theta V_0}\right), \tag{7.5}$$

$$\Theta = \frac{R_{CB}}{R_{CB} + R_V}. \tag{7.6}$$

With increasing driving voltage V_0, the charging time Δt_{up} decreases and the discharging time Δt_{down} increases (for V_0 in the operation interval as given in

Eq. 7.2). The oscillation frequency f as a function of V_0 has a maximum value at:

$$V_0(f_{max}) = \frac{V_{min}V_{max}}{V_{min}+V_{max}}\left(2+\frac{R_V}{R_{CB}}\right). \tag{7.7}$$

At $V_0(f_{max})$, the oscillator frequency can exceed the value $f=(\tau_{up}+\tau_{down})^{-1}$ considerably, depending on the dynamical hysteresis limits V_{min} and V_{max}.

7.2 Relaxation oscillations

Fig. 7.3 shows a set of measured oscillation curves $V_{SD}(t)$ for various values of the driving voltage V_0. To ensure the working regime of the oscillator, we have chosen a serial resistor R_V=46 kΩ of comparable size with the dissipative Corbino resistance R_{CB}=76 kΩ. From the I-V curve (inset of Fig. 7.1) and Eq. 7.1, this would yield an operation interval for V_0 from 1.52 V to 2.39 V. As seen from Fig. 7.3, the oscillator works within about 1.65 V$<V_0<$2.25 V, an interval which is distinctively narrower than the one deduced from the DC-measured hysteresis of the I-V curve. In turn, the amplitude is larger than ΔV taken from Fig. 7.1. Both discrepancies can be resolved simultaneously taking into account a wider dynamical hysteresis at the oscillator frequencies of some kHz in comparison to the quasistationary one.

Therefore, we have supplemented the DC-measurement of the hysteresis by AC data in the frequency range from $0<f\leq$10 kHz. We observed a drastic increase of the hysteresis at low frequencies (from 25 mV at DC to 0.4 V at 27 Hz) and a saturation at higher frequencies (0.3 V-0.4 V for f from 100 Hz to 1 kHz). The occurrence of a hysteresis in the I-V characteristics of QH samples near the breakdown is commonly explained on the basis of an electron heating model (see, for example Refs. [9, 67]). The hysteresis is mainly determined by the contribution of hopping processes to the conduction [67]. Applying this model to our sample, a suppression of the hopping contribution from $\sigma_{hop}=1.3\times10^{-3}\sigma_{xy}$ at DC to $\sigma_{hop}=4.5\times10^{-4}\sigma_{xy}$ at f=27 Hz can explain the increase of the hysteresis as observed. A reduction of the hopping conductivity corresponds to a shrinking of the localization length [115]. An experiment that displays the frequency dependent hysteresis is included at the end of this section.

The measured oscillation amplitude is therefore a direct measure of the dynamical hysteresis of the QHE breakdown at the oscillation frequency. The amplitude of the oscillations remained almost unchanged with V_0 in the working regime (180 mV to 250 mV, close to the operation limits of the oscillator the amplitudes tend to vary). The measured charging and discharging times show a pronounced V_0-dependence, which we used to estimate the total capacitance C_T of the circuit. To reach higher frequencies, no separate capacitor was attached,

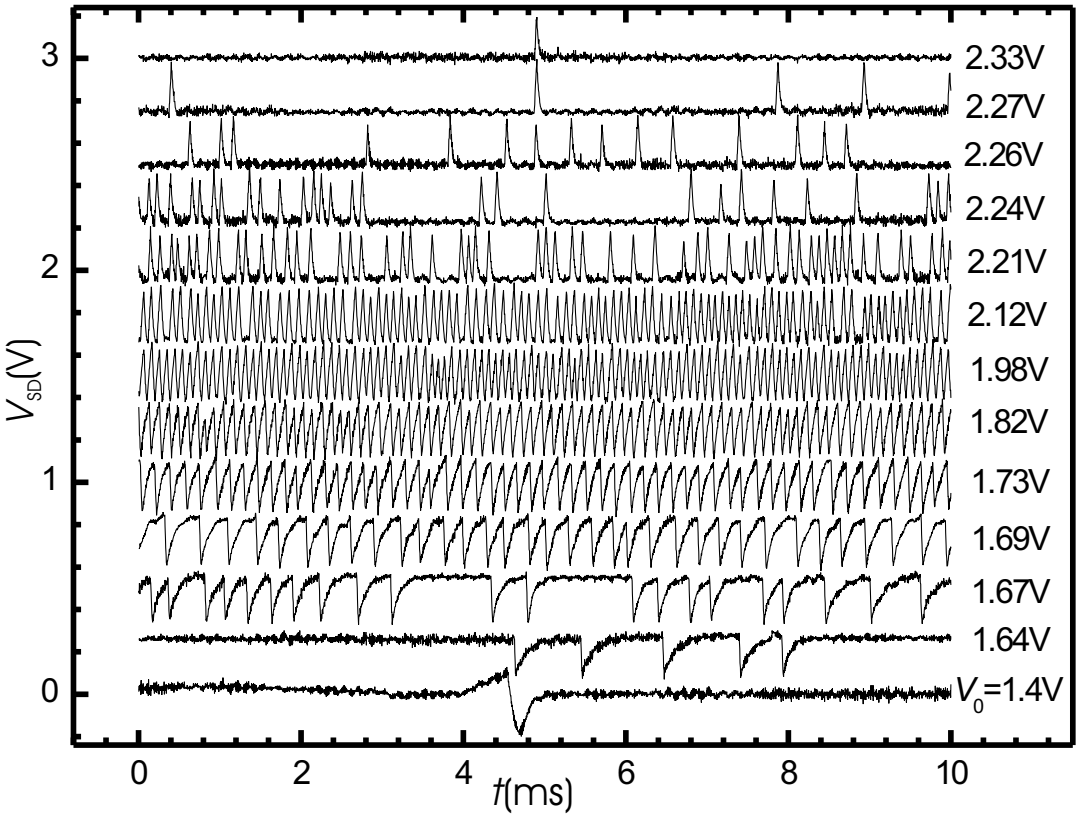

Figure 7.3: Relaxation oscillations of the Corbino oscillator at different driving voltages V_0. The oscillator operates at V_0 between 1.65 V and 2.25 V (curves are shifted for clarity). Whereas the oscillation amplitude is almost constant within this range, the frequency changes and has a maximum at $V_0 \approx 2$ V.

so that C_T is dominated by the capacitance of cables and connectors (for C_T, the capacitances of the Corbino device (<0.1 pF) and of the input of the oscilloscope (20 pF) can be neglected). From the measured values of Δt_{up}, Δt_{down} as a function of V_0, the best fit applying Eq. 7.5 was obtained with C_T=2.1 nF.

Fig. 7.4 presents the corresponding data in comparison to the calculated dependencies. The measured dependencies of Δt_{up}, Δt_{down} on V_0 are reproduced quite well, including the operation range of the oscillator. The calculations yield a maximum oscillation frequency of 11.9 kHz at V_0=2.02 V, which is in reasonable agreement with the experimental value of f_{max}=11.2 kHz at V_0=2.1 V (see inset of Fig. 7.4). The upper frequency of the oscillator is mainly determined by the capacitance C_T and the serial resistance R_V. The dissipative resistance of the Corbino device R_{CB} is of less importance, as it acts only as a parallel shunt to R_V for the discharging process.

Consequently, to reach higher frequencies the values of C_T and R_V should be reduced. Smaller R_V values require, according to $R_V^{min}=\Delta V/I_c^{min}$, a reduced

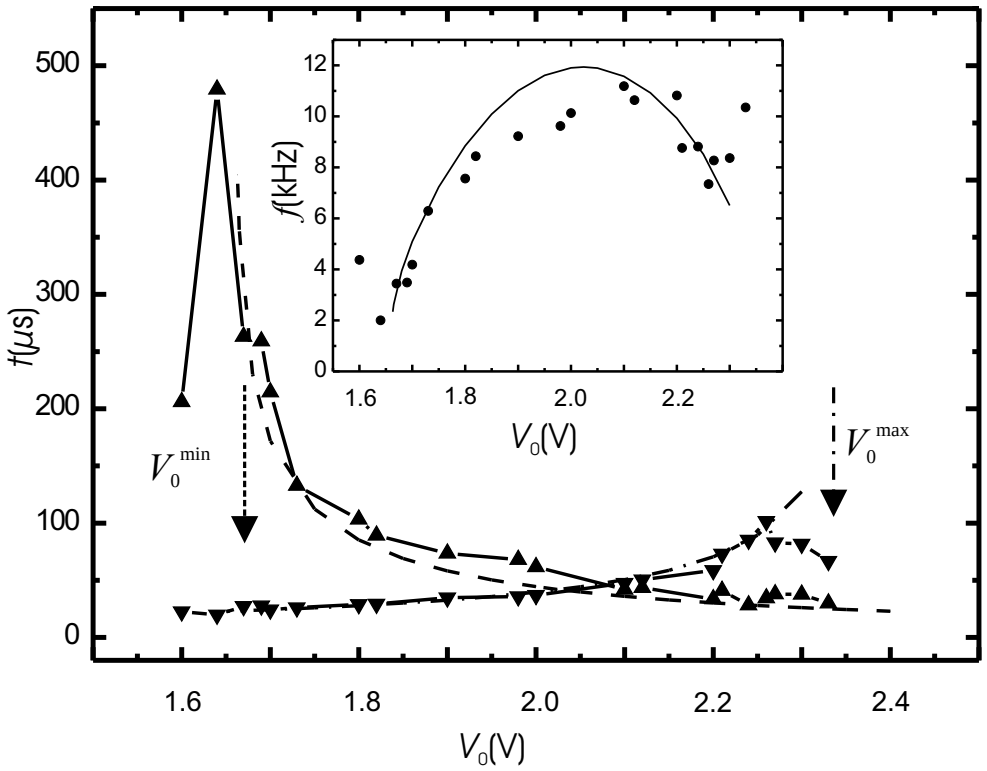

Figure 7.4: Charging and discharging times of the Corbino oscillator. Measured charging times Δt_{up} (up triangle) and discharging times Δt_{down} (down triangle) are plotted as a function of the driving voltage V_0, in comparison to the calculated values (dashed line: charging, dash-dotted line: discharging) with the parameters τ_{up}=96 μs, τ_{down}=60 μs, V_{min}=1.46 V, V_{max}=1.66 V. The limits of the working regime as calculated from the model are depicted by arrows. Inset: Oscillator frequency f as a function of the driving voltage V_0 (circles: measured values, solid line: model).

hysteresis. Thus, higher frequencies can be realized only by a simultaneous reduction of the oscillation amplitude. The physical limits of the oscillation frequency are given by the switching times of the Corbino device, which we have found to be rather short (a few nanoseconds in low-mobility samples, see Chapter 6). With this, upper frequencies in the GHz range are potentially accessible. Of course, there are simpler solutions to generate GHz oscillations like for example resonant tunneling devices [111]. However, the oscillator as described above provides additional insight into the dynamical properties of the breakdown of the QHE (dynamical hysteresis).

To display the frequency dependent hysteresis, we have used the setup for the time-resolved measurement for Corbino devices, as shown in Fig. 6.1. We have applied sinusoidal and triangular waves to another Corbino device, which was

fabricated from the same wafer W_3 but with a channel width of w=100 μm. We have connected another coaxial cable to the ends of the serial 50 Ω resistor to read the response signal at an oscilloscope. The Corbino device acted like a rectifying circuit, which rectified the applied waves according to the lower and higher values of the critical voltages V_{min} and V_{max}. We have recorded the difference V_{max}-V_{min} as the hysteresis size as a function of the frequency of the applied waves. As seen in Fig. 7.5 the hysteresis increases for both sinusoidal and triangular waves with increasing frequency, confirming our prediction from the relaxation oscillator measurements.

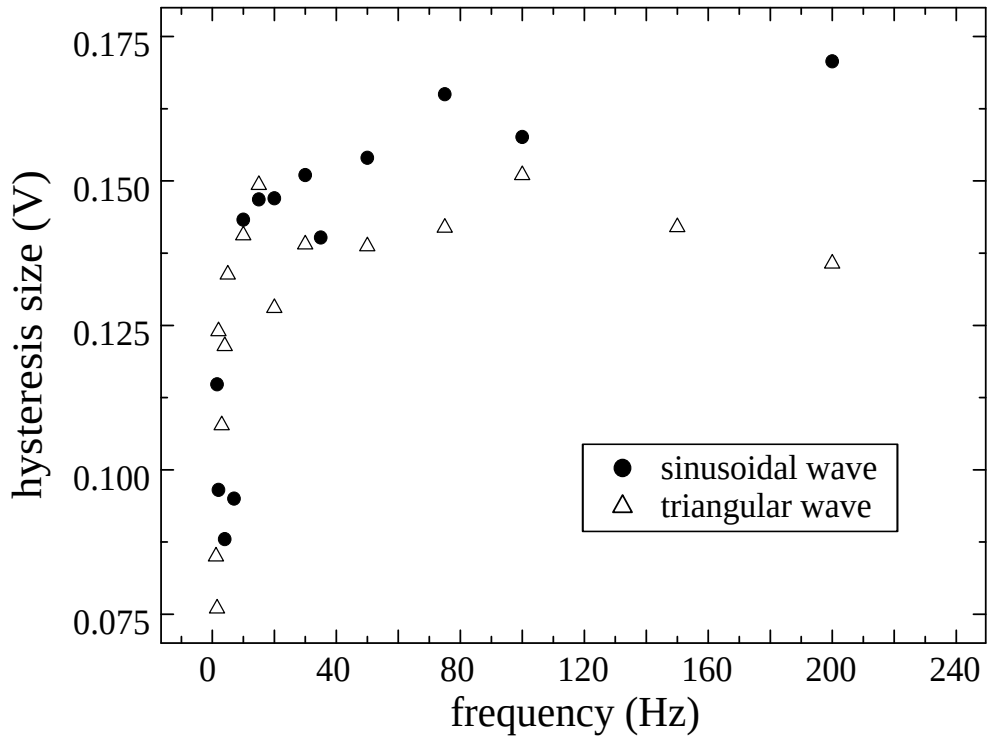

Figure 7.5: Frequency dependent hysteresis of a Corbino device. Using the setup in Fig. 6.1, when sinusoidal and triangular waves are applied, the circuit behaves like a rectifier. The rectification occurs at the lower and higher values of the critical voltages V_{min} and V_{max}, and their difference (hysteresis size) increases with increasing frequency.

7.3 Summary

To summarize, we have generated relaxation oscillations by using a quantum Hall Corbino device as a bistable switching element. The oscillation amplitude is determined by the dynamical hysteresis of the QH device. The frequency of oscillations depends on the resistances and capacitances of the circuit, but

also on the dynamical hysteresis of the Corbino device. This hysteresis is determined by the dynamical breakdown properties of the device and can be directly deduced from the measurements. It was found that the hysteresis increases tremendously at low frequencies, which was also confirmed in another experiment by directly measuring the AC hysteresis of a Corbino device. This is explainable within the electron heating model by a decreasing hopping conductivity at low frequencies. The oscillator operates within a certain range of the driving voltage, within which the oscillation frequency has a distinct maximum. With knowledge of the limiting voltages of the dynamical hysteresis and of the resistances and capacitances of the circuit, the properties of the oscillator, as for example the frequency as a function of the driving voltage, can be modelled in good agreement with the experiment. The highest frequencies can be achieved by the application of QH devices with a small, but stable dynamical hysteresis in the I-V characteristics of the breakdown.

8 Conclusion

In this work we have performed space and time-resolved measurements at the breakdown of the quantum Hall effect (QHE). The QHE measurements are generally done with Hall bar devices, where the longitudinal ρ_{xx} and transversal resistivities ρ_{xy} of a two-dimensional electron system (2DES) can be simultaneously measured at liquid helium temperatures. At high magnetic fields ρ_{xx} vanishes, and ρ_{xy} exhibits quantum Hall plateaus with quantized values (ρ_{xy}=h/ie^2), when a whole number of Landau levels are fully occupied. The quantization of ρ_{xy}, the dependence of the quantized values only on natural constants and the dissipationless current flow are the most remarkable features of the QHE. However, above a critical sample current value the quantum Hall plateaus disappear, and the longitudinal resistivity increases by several orders of magnitude, corresponding to a dissipation in the current flow. This is the breakdown of the QHE, for which many mechanisms and models were proposed so far. But since a complete conclusive theory is still missing, further work was needed especially for the detailed understanding of the microscopic processes of the QHE breakdown. This inspired the investigations presented in this thesis.

For this purpose we have fabricated quantum Hall devices from MBE grown modulation doped GaAs/AlGaAs wafers, where the 2DES was realized at the GaAs/AlGaAs heterojunctions having electron mobilities in the range $1{\times}10^5$ cm^2/Vs $\leq \mu_H \leq 9{\times}10^5$ cm^2/Vs. By the help of the photolithography technique, the mesa structures of the Hall bar and Corbino devices were defined, and the ohmic contacts were produced. When the device fabrication was finished, the quantum Hall devices were placed on special chip carriers and then mounted into sample holders for the magneto-cryoststats, where we performed our breakdown experiments.

The first space-resolved relaxation measurements at the breakdown of the QHE were done by Kaya *et al.*, where they measured the decay of ρ_{xx} in a constricted Hall bar as a function of distance [15]. The decay of the longitudinal resistivity corresponds to a cooling of hot electrons by inelastic scattering processes. Characteristic inelastic relaxation lengths ℓ_D in the range of 0.3 μm$<\ell_D<$4 μm for sample mobilities of $4{\times}10^4$ cm^2/Vs $\leq \mu_H \leq 5.3{\times}10^5$ cm^2/Vs, were found to match one to one the elastic mean free paths ℓ_{mfp}, which are determined by the Coulomb scattering at ionized impurities. Energy relaxation times τ_{rel} were determined by dividing the values of the energy relaxation lengths ℓ_D to the

drift velocities v_D, and their order of magnitude (0.24 - 2.6 ns) were found to be in good agreement with the earlier assumptions in the literature.

The reverse experiments of the excitation of electrons from the QH state to the dissipative state also showed a clear correlation between the mobility (or the scattering density) and the spatial evolution of the QHE breakdown along a constriction in the current path [14, 82, 83]. The exponential increase of the slope of the resistivity profile $\rho_{xx}(x)$, $\Gamma = \mathrm{d}\rho_{xx}/\mathrm{d}x$ as a function of the square of the inverse current is found to be consistent with inter-Landau level tunneling in presence of disorder or strong potential fluctuations. Therefore we attributed the excitation process at supercritical currents to impurity-assisted inter-Landau-level tunneling. The function Γ became steeper along the drift direction with decreasing mobility. This reflects again the strong dependence of the hot-electron generation on the density of scatterers. However in the space-resolved excitation measurements it was not possible to extract the excitation times τ_{exc} of the electrons, due to the more complicated interplay between excitation, relaxation and the effective width of the current carrying incompressible regions.

By applying a phenomenological model for the transitions between the two Landau-levels above and below the Fermi level, the space-resolved excitation measurements could be simulated [86]. This model is based on the well established assumption of the presence of potential fluctuations mainly due to charged impurities. These fluctuations provide localization centers for electrons and holes in the Landau levels and lead to locally enhanced electric fields. On the basis of these assumptions, the breakdown of the QHE was explained by the field-dependent evolution of compressible islands, which merge to macroscopic areas connecting the sample edges at the breakdown of the QHE. Involving the evolution of these compressible islands in time by inter-Landau-level transitions, it was possible to obtain the length scale of the breakdown along the drift direction of the electrons. Excitation times τ_{exc} (average drifting times of the electrons between inelastic scattering events) of the order of the relaxation times τ_{rel} could be deduced. From general thermodynamic arguments they have found that the relaxation rate cannot be smaller than the excitation rate to the higher level, which means $\tau_{exc} \geq \tau_{rel}$. Although the dependence of the results on τ_{exc}/τ_{rel} was weak, the best results were obtained for $\tau_{exc} = \tau_{rel}$. However, these values of τ_{exc} and τ_{rel} have been estimated by assuming a homogeneous current flow over the width of the sample, an assumption which is still a subject of discussion.

In order to measure the time scale of excitation τ_{exc} directly, we applied rectangular pulses to the 2DES of the Hall bar devices with pulse widths t_p in the range 0.3 ns $\leq t_p \leq$ 0.4 ms. We have performed the measurements on different Hall bar devices having different electron mobilities 1×10^5 cm^2/Vs $\leq \mu_H \leq 9\times10^5$ cm^2/Vs, and at integer filling factors ν=2, ν=4

and ν=6. In order to keep the average applied voltage constant, we varied the pulse width and the period of the electrical pulses simultaneously, keeping the duty cycle constant. We observed that the breakdown starts only after a certain critical time, if the amplitude of the pulses is higher than the critical DC voltage value [88, 89]. These critical times were of the order of nanoseconds and depended on pulse amplitude, magnetic field and electron mobility. We repeated the measurements for different duty cycle values and found that the pulse width is the critical parameter but not the period. This means that the pause between the pulses does not play a significant role, at least up to a certain duty cycle value. The range of the critical pulse widths was between 0.4 ns and 18 ns, being in agreement with earlier estimations. We interpreted the critical pulse widths as the average drifting times of the electrons between inelastic scattering events causing tunneling between the Landau-levels and the dissipation. From a simple drift model, which assumes a homogeneous distribution of scatterers and a homogeneous current flow throughout the sample, we obtained the lower limit for the critical drift lengths varying from about 1 μm to 25 μm by multiplying the critical times with the drift velocity. We interpreted these critical lengths as the average drifting distances related to the inelastic scattering lengths ℓ_{in} of the electrons, and their characteristic dependences on the amplitude, filling factor and the mobility could also be attributed to impurity-assisted inter-Landau-level tunneling.

We repeated the time-resolved breakdown measurements also on Corbino devices to investigate the possible existence of edge effects at the QHE breakdown [103, 104, 105]. The measurements were performed by applying short electric pulses with either constant duty cycle or with constant pulse width, but for different background voltage levels. As in the Hall bar devices, the QHE breakdown was found to be suppressed below a certain critical pulse width, although the amplitude of the pulses is higher than the critical DC voltage. In this region of the supercritical nondissipative pulses, the pulse amplitudes could be larger than the double amount of the average of the critical voltages, without causing any dissipation. The critical times were of the order of a few nanoseconds being in agreement with the results of Hall bar measurements. Between Hall bars and Corbino devices, no general differences of the response to short electric pulses were found. The only deviations were observed in the behavior of the Corbino devices at filling factor ν=2, with their almost perfect QHE conditions and abrupt breakdown profiles, and with the jumps and bunching effects in the critical pulse widths. We believe that these effects are due to the different kind of edge states in the Corbino devices, in comparison to Hall bars. We also studied the relaxation of the 2DES in Corbino devices, from the dissipative to the QH state by setting simultaneously the pulse width to $t_p \geq t_p^c$ and the pulse amplitude to $A \geq V_{SD}^c$, and varying the pause between the pulses, and the background DC level V_{DC}. A monotonous decrease of the conductivity with increasing pause was found for V_{DC}=0 V. But when V_{DC} was set to finite, subcritical values of

$0<V_{DC}<V_{SD}^{c}$, the average conductivity dropped abruptly back to $\langle\sigma_{xx}\rangle\approx 0$ (reappearance of the QHE) at markedly reduced relaxation times, which decreased with increasing V_{DC}. In a similar experiment we kept the duty cycle and the supercritical amplitude constant and varied the background DC level. As V_{DC} was kept within a certain subcritical DC voltage range, the QHE was recovered. We attributed all these observations to a scattering rate, which is enhanced by the drift of the hot electrons during the subcritical pulse pause. The higher the subcritical V_{DC}, the higher is the drift velocity and therefore the more inelastic scattering events the electrons encounter during the pulse pause. This confirms our interpretation of the excitation and relaxation in QH systems on the basis of a drift model, explaining both processes by impurity-induced inter-Landau-level transitions. Further experiments for investigating the relation between the excitation times τ_{exc} and relaxation times τ_{rel} of the breakdown of the QHE have shown that the values for τ_{exc} and τ_{rel} are comparable ($\tau_{exc}\approx\tau_{rel}$).

Finally, we have generated relaxation oscillations by using a quantum Hall Corbino device as a bistable switching element [113]. The dynamical hysteresis of the QH device determined the oscillation amplitude. The frequency of the oscillation depended on the resistance and capacitance values of the circuit, and also on the dynamical hysteresis of the Corbino device. The size of the dynamical hysteresis corresponding to the oscillation amplitude, was found to be greater than the DC hysteresis and was attributed to the suppression of the hopping conductivity. The increasing hysteresis with increasing frequency was confirmed in another experiment by directly measuring the AC hysteresis of a Corbino device. The relaxation oscillators operated within a certain range of the driving voltage, within which the oscillation frequency had a distinct maximum. Knowing the limiting voltages of the dynamical hysteresis and the resistance and capacitance values of the circuit, the properties of the oscillator could be modelled in good agreement with the experiment.

Bibliography

[1] K. von Klitzing, G. Dorda, M. Pepper, Phys. Rev. Lett. **45**, 494 (1980).

[2] K. von Klitzing, Rev. Mod. Phys. **58**, 519 (1986).

[3] D.C. Tsui, H.L. Störmer, A.C. Gossard, Phys. Rev. Lett. **48**, 1559 (1982).

[4] R.B. Laughlin, Phys. Rev. Lett. **50**, 1395 (1983).

[5] R.B. Laughlin, Rev. Mod. Phys. **71**, 863 (1999).

[6] H.L. Störmer, Rev. Mod. Phys. **71**, 875 (1999).

[7] D.C. Tsui, Rev. Mod. Phys. **71**, 891 (1999).

[8] K. Yoshihiro, J. Kinoshita, K. Inagaki, C. Yamanouchi, J. Moriyama, S. Kawaji, Surf. Sci. **113**, 16 (1982).

[9] G. Ebert, K. von Klitzing, K. Ploog, G. Weimann, J. Phys. C. **16**, 5441 (1983).

[10] G. Nachtwei, Physica E **4**, 79 (1999).

[11] S. Kawaji, H. Hirakawa, M. Nagata, T. Okamoto, T. Fukase, T. Gotoh, J. Phys. Soc. Jpn. **63**, 2303 (1994).

[12] Y. Kawaguchi, F. Hayashi, S. Komiyama, T. Osada, Y. Shiraki, R. Itoh, Jpn. J. Appl. Phys. **34**, 4309 (1995).

[13] S. Komiyama, Y. Kawaguchi, T. Osada, Y. Shiraki, Phys. Rev. Lett. **77**, 558 (1996).

[14] I.I. Kaya, G. Nachtwei, K. von Klitzing, K. Eberl, Europhys. Lett. **46**, 62 (1999).

[15] I.I. Kaya, G. Nachtwei, K. von Klitzing, K. Eberl, Phys. Rev. B, **58**, R7536 (1998).

[16] L. Eaves, F.W. Sheard, Semicond. Sci. Technol. **1**, 346 (1986).

[17] S. Komiyama, T. Takamasu, S. Hiyamizu, S. Sasa, Solid State Commun. **54**, 479 (1985).

[18] E. Mooser, *Physics and Chemistry of Materials with Layered Structures*, Reidel Dordrecht, (1976).

[19] F.L. Vogel, A. Hérold, eds., *Proceedings of the Franco American Conference on Intercalation Compounds of Graphite, La Napoule* (Mater. Sci. Engin. **31**, 1)(1977).

[20] M.S. Erukhimov, B.A. Tavger, Zh. Eksp. Teor. Fiz. **53**, 926 (1967).

[21] M.W. Cole, Rev. Mod. Phys. **46**, 451 (1974).

[22] S.M. Sze, *Physics of Semiconductor Devices*, Wiley (1969).

[23] D.C. Tsui, R.A. Logan, Appl. Phys. Lett. **35**, 99 (1979).

[24] T. Ando, A.B. Fowler, F. Stern, Rev. Mod. Phys. **54**, 437 (1982).

[25] E. Braun, *The Quantum Hall Effect*, Proc. of the Int. School of Physics "Enrico Fermi", Metrology at the Frontiers of Physics and Technology, 211 (1992).

[26] J.H. Davies, *The Physics of Low Dimensional Semiconductors*, Cambridge University Press (1998).

[27] C. Kittel, *Introduction to Solid State Physics*, John Wiley & Sons (1986).

[28] G. Nachtwei, *Quanteneffekte in niederdimensionalen Systemen*, Skriptum zur Vorlesung (2002).

[29] V. Fock, Zeitschrift für Physik **47**, 446 (1928).

[30] L.D. Landau, Zeitschrift für Physik **64**, 629 (1930).

[31] P. Drude, Annalen der Physik **1**, 566 (1900).

[32] E. Hall, Amer. Jour. Math. **2**, 287 (1879).

[33] L. Shubnikov, W.J. de Haas, Leiden Comm. 207a, 210a, (1930).

[34] J. Singleton, *Band Theory and Electronic Properties of Solids*, Oxford University Press (2001).

[35] T. Okuno, S. Kawaji, T. Ohrui, T. Okamoto, Y. Kurata, J. Sakai, J. Phys. Soc. Jpn. **64**, 1881 (1995).

[36] U. Klaß, W. Dietsche, K. von Klitzing, K. Ploog, Z. Phys. B-Cond. Matter **82**, 351 (1991).

[37] M.E. Cage, R.F. Dziuba, B.F. Field, E.R. Williams, S.M. Girvin, A.C. Gossard, D.C. Tsui, R.J. Wagner, Phys. Rev. Lett. **51**, 1374 (1983).

[38] L. Bliek, E. Braun, G. Hein, V. Kose, J. Niemeyer, G. Weimann, W. Schlapp, Semicond. Sci. Technol. **1**, 110 (1986).

[39] F. Kuchar, G. Bauer, G. Weimann, H. Burkhard, Surf. Sci. **142**, 196 (1984).

[40] H.L Störmer, A.M. Chang, D.C. Tsui, J.C.M. Hwang, in *Proc. 17th Int. Conf. on the Physics of Semiconductors, San Francisco, 1984*, (Springer, Berlin), 267 (1985).

[41] T. Takamasu, S. Komiyama, S. Hiyamizu, S. Sasa, Surf. Sci. **170**, 202 (1986).

[42] S.A. Trugman, Phys. Rev. B **27**, 7539 (1983).

[43] P. Středa, K. von Klitzing, J. Phys. C. **17**, L483 (1984).

[44] V. Tsemekhman, K. Tsemekhman, C. Wexler, J.H. Han, D.J. Thouless, Phys. Rev. B **55**, R10201 (1997).

[45] M. Büttiker, Phys. Rev. B **38**, 9375 (1988).

[46] R. Landauer, Z. Phys. B-Cond. Matter **68**, 217 (1987).

[47] R. Landauer, IBM J. Res. Dev. **1**, 223 (1957).

[48] B.I. Halperin, Phys. Rev. B **25**, 2185 (1982).

[49] P. Středa, L. Smrčka, J. Phys. C **16**, L895 (1983).

[50] O. Heinonen, P.L. Taylor, Phys. Rev. B **28**, 6119 (1983).

[51] J.R. Kirtley, Z. Schlesinger, T.N. Theis, F.P. Milliken, S.L. Wright, L.F. Palmateer, Phys. Rev. B **34**, 1384 (1986).

[52] M.E. Cage, G. Marullo Reedtz, D.Y. Yu, C.T. Van Degrift, Semicond. Sci. Technol. **5**, 351 (1990).

[53] M.E. Cage, J. Res. Natl. Inst. Stand. Technol. **98**, 361 (1993).

[54] G. Ebert, K. von Klitzing, G. Weimann, J. Phys. C. **18**, L257 (1985).

[55] H.Z. Zheng, D.C. Tsui, A.M. Chang, Phys. Rev. B **32**, 5506 (1985).

[56] P.F. Fontein , P. Hendriks, J.H. Wolter, Surf. Sci. **229**, 47 (1990).

[57] R. Knott, W. Dietsche, K. von Klitzing, K. Eberl, K. Ploog, Semicond. Sci. Technol. **10**, 117 (1995).

[58] B. Jeanneret, B.D. Hall, H.J. Bühlmann, R. Houdré, M. Illegems, B. Jeckelmann, U. Feller, Phys. Rev. B **51**, 9752 (1995).

[59] E. Yahel, D. Orgad, A. Palevski, H. Shriktman, Phys. Rev. Lett. **76**, 2149 (1996).

[60] A. Yacoby, H.F. Hess, T.A. Fulton, L.N. Pfeiffer, K.W. West, Solid State Commun. **1**, 111 (1999).

[61] K.L. McCormick, M.T. Woodside, M. Huang, M. Wu, P.L. McEuen, C. Duruoz, J.S. Harris, Phys. Rev. B **59**, 464 (1999).

[62] P. Weitz, E. Ahlswede, J. Weis, K. von Klitzing, K. Eberl, Physica E **6**, 247 (2000).

[63] S. Kawaji, K. Hirakawa, M. Nagata, Physica B **184**, 17 (1993).

[64] S. Kawaji, K. Hirakawa, M. Nagata, T. Okamoto, T. Fukase, T. Goto, Surf. Sci. **305**, 161 (1994).

[65] A. Boisen, P. Bøggild, A. Kristensen, P.E. Lindelof, Phys. Rev. B **50**, 1957 (1994).

[66] G. Nachtwei, G. Lütjering, D. Weiss, Z.H. Liu, K. von Klitzing, C.T. Foxon, Phys. Rev. B **55**, 6731 (1997).

[67] G. Nachtwei, Z.H. Liu, G. Lütjering, R.R. Gerhardts, D. Weiss, K. von Klitzing, K. Eberl, Phys. Rev. B **57**, 9937 (1998).

[68] R.J. Haug, K. von Klitzing, K. Ploog, Springer Ser. Solid. State Sci. **87**, 185 (1989).

[69] N.Q. Balaban, U. Meriav, H. Shtrikman, Y. Levinson, Phys. Rev. Lett. **71**, 1443 (1993)

[70] C. Simon, B.B. Goldberg, F.F. Fang, M.K. Thomas, S. Wright, Phys. Rev. B **33**, 1190 (1986).

[71] Y. Kawaguchi, S. Komiyama, T. Osada, Y. Shiraki, Physica B **227**, 183 (1996).

[72] Y. Suematsu, and A.R. Adams, *Handbook of Semiconductor Lasers and Photonic Integrated Circuits*, Chapman and Hall (1994).

[73] T.C. Shen, G.B. Gao, H. Morkoç, J. Vac. Sci. Technol. B **10**, 2113 (1992).

[74] V.L. Rideout, Solid State Electron. **18**, 541 (1975).

[75] A. Piotrowska, A. Guivarch, G. Pelous, Solid State Electron. **26**, 179 (1983).

[76] J.M. Woodall, J.L. Freeouf, J. Vac. Sci. Technol. **19**, 794 (1981).

[77] N. Braslau, J. Vac. Sci. Technol. A **4**, 3085 (1986).

[78] A.C. Adams, B.R. Pruniax, J. Electrochem. Soc. **120**, 408 (1973).

[79] *Operator's Handbook*, Oxford Instruments (UK) Ltd. (1994).

[80] *Getting Started with LabVIEW*, National Instruments (2000).

[81] S. Kawaji, K. Hirakawa, M. Nagata, T. Okamoto, T. Fukase, T. Gotoh, Surf. Sci. **305**, 161 (1994).

[82] G. Nachtwei, I.I. Kaya, B.E. Sağol, K. von Klitzing, K. Eberl, Physica B **272**, 127 (1999).

[83] I.I. Kaya, G. Nachtwei, B.E. Sağol, K. von Klitzing, K. Eberl, Physica E **6**, 128 (2000).

[84] V.L. Pokrovsky, L.P. Pryadko, A.L. Talapov, J. Phys.: Condens. Matter **2**, 1583 (1990).

[85] T. Martin, S. Feng, Phys. Rev. Lett. **64**, 1971 (1990).

[86] K. Güven, R.R. Gerhardts, I.I. Kaya, B.E. Sağol, G. Nachtwei, Phys. Rev. B **65**, 155316 (2002).

[87] R.R. Gerhardts, J. Groß, Phys. Rev. B **60**, 2561 (1999).

[88] B.E. Sağol, G. Nachtwei, I.I. Kaya, K. von Klitzing, K. Eberl, in *Proceedings of the 25th International Conference on the Physics of Semiconductors, Osaka-2000*, edited by N. Miura and T. Ando, Springer Proceedings in Physics (Springer, New York), **87** Pt. II, 959 (2001).

[89] B.E. Sağol, G. Nachtwei, K. von Klitzing, K. Eberl, Physica B **314**, 268 (2002).

[90] R.J. Smith, *Circuits, Devices and Systems*, John Wiley & Sons (1984).

[91] G. Nachtwei, S. Heide, C. Breitlow, P. Svoboda, M. Cukr, Phys. Rev. B **50**, 8488 (1994).

[92] G. Ernst, *Zeitaufgelöste Transportmessungen zum Quanten-Hall-Effekt*, Ph.D. Dissertation, Max-Planck-Institut für Festkörperforschung, Stuttgart (1997).

[93] V.A. Volkov, S.A. Mikhailov, in *Landau Level Spectroscopy*, Editors: G. Landwehr, E.I. Rashba, chapter 15, Elsevier Science Publishers, Amsterdam (1991).

[94] F. Stern, Phys. Rev. Lett. **18**, 546 (1967).

[95] A.V. Chaplik, Sov. Phys. JETP **35**, 395 (1972).

[96] T.N. Theis, Surf. Sci. **98**, 515 (1980).

[97] N.B. Zhitenev, R.J. Haug, K. von Klitzing, K. Eberl, Phys. Rev. Lett. **71**, 2292 (1993).

[98] G. Ernst, N.B. Zhitenev, R.J. Haug, K. von Klitzing, K. Eberl, Surf. Sci. **361/362**, 102 (1996).

[99] R.J. Haug, Semicond. Sci. Technol. **8**, 131 (1993).

[100] R.J. Haug, K. von Klitzing, K. Ploog, in *High Magnetic Fields in Semicondoctor Physics II*, edited by G. Landwehr, Springer Series in Solid State Physics (Springer-Verlag Berlin, Heidelberg) **87**, 185 (1989).

[101] E. Ahlswede, J. Weis, K. von Klitzing, K. Eberl, Physica E **12**, 165 (2002).

[102] E. Ahlswede, *Potential- und Stromverteilung beim Quanten-Hall-Effekt bestimmt mittels Rasterkraftmikroskopie*, Ph.D. Dissertation, Max-Planck-Institut für Festkörperforschung, Stuttgart (2002).

[103] B.E. Sağol, G. Nachtwei, K. von Klitzing, G. Hein, K. Eberl, Phys. Rev. B **66**, 075305 (2002).

[104] B.E. Sağol, G. Nachtwei, N.G. Kalugin, G. Hein, K. Eberl, 26th International Conference on the Physics of Semiconductors (ICPS-26) in Edinburgh, Scotland (2002).

[105] B.E. Sağol, G.Nachtwei, N.G. Kalugin, G. Hein, K. Eberl, 15th International Conference on High Magnetic Fields in Semiconductor Physics (SemiMag-15) in Oxford, England (2002).

[106] R.P. Taylor, R. Newbury, A.S. Sachrajda, Y. Feng, P.T. Coleridge, M. Davies, J.P. McCaffrey, Superlatt. Microstruct. **24**, 337 (1998).

[107] W. Eberle, J. Hirschinger, U. Margull, W. Prettl, V. Novak, H. Kostial, Appl. Phys. Lett. **68**, 3329 (1996).

[108] K. Aoki, S. Fukui, Physica B **272**, 274 (1999).

[109] B. Van der Pol, J. Van der Mark, Nature **120**, 363 (1927).

[110] A.A. Andronov, A.A. Vitt, S.E. Khaikin, *Theory of Oscillators*, Pergamon Press (1966).

[111] E.R. Brown, J.R. Söderström, C.D. Parker, L.J. Mahoney, K.M. Molvar, T.C. McGill, Appl. Phys. Lett. **58**, 2291 (1991).

[112] The application of a Corbino device near the breakdown of the QHE for generating oscillations was proposed by N.G. Kalugin (unpublished, 2002).

[113] G. Nachtwei, N.G. Kalugin, B.E. Sağol, C. Stellmach, G. Hein, Appl. Phys. Lett. **82**, 2068 (2003).

[114] W.F. Chow, *Principles of Tunnel Diode Circuits*, Wiley & Sons Inc. (1964).

[115] F. Hohls, U. Zeitler, R.J. Haug, Phys.Rev. Lett. **88**, 036802 (2002).

Acknowledgments

The work presented in this dissertation was carried out in the "Technische Universität Carolo-Wilhelmina zu Braunschweig" and in the "Max-Planck-Institut für Festkörperforschung" in Stuttgart, Germany. Part of the device fabrication was done in the "Physikalisch-Technische Bundesanstalt" in Braunschweig. I am indebted to the "Deutsche Akademische Austauschdienst (DAAD)" and to the "Max-Planck-Gesellschaft (MPG)" for the financial support for my stay in Germany. I would like to take this opportunity to express my deepest gratitude to all these institutions, but especially to the people, without whom this work would not have been possible. My very special thanks go to:

- Prof. Dr. G. Nachtwei for his excellent supervision, for his deep insight in this subject, for his new ideas, for the numerous discussions and for the very fruitful four-year work. I would also like to thank him especially for his patience, understanding and care throughout all the phases of my dissertation;
- Prof. Dr. K. von Klitzing for giving me the opportunity to work in his department, for his continuous interest to our experiments and especially for his challenging questions;
- Dr. I.I. Kaya for introducing me to cryogenics, magnetotransport measurements and to the QHE breakdown. I would also like to thank him and his wife Yeşim Kaya sincerely for their support and help in the very first months of my stay in Germany;
- Prof. Dr. R.J. Haug for reading and evaluating my thesis;
- Prof. Dr. J. Hesse, Prof. Dr. P. Weidelt and Prof. Dr. R.J. Haug for accepting to be the members of my examination committee;
- Prof. Dr. R.R. Gerhardts and Dr. K. Güven for their excellent numerical calculations that successfully simulated the space-resolved excitation measurements;
- Prof. Dr. A. Hangleiter for his references that helped me to prolong my DAAD scholarship;

- Dr. N.G. Kalugin for the valuable discussions and for the fruitful cooperation, but especially for his idea to build the Corbino oscillator;
- Dr. F.J. Ahlers for giving me the opportunity to fabricate our samples in the cleanroom facilities of PTB;
- Dr. G. Hein for the introduction and continuous help in the cleanroom facilities of PTB, for his interest to our subject, but especially for designing our photomasks and for the deposition of the contact materials;
- Dr. K. Eberl and Mr. M. Hauser for their supposedly "low quality" wafers, which were indispensable for our experiments;
- Mr. A. Buß, Mr. A. Hirsch, Mr. C. Stellmach for their rapid learning of the measurement setup and the device fabrication and for their moral help in the last months of my work;
- Mr. F. Werner, Mr. H.J. Wruck, and Mr. H. Kroker for their efforts in supplying us huge amounts of liquid helium for our hungry magnet-cryostats and for their competence in assembling and disassembling of all kinds of mechanical objects;
- Mr. F. Hitzel for solving all kinds of software, hardware and shareware problems;
- Mrs. M. Riek for introducing me to the cleanroom facilities of MPI and for the chip carriers;
- Mr. M. Schmid for helping me to build the sample holder for the time-resolved measurements;
- Mr. T. Reindl and Mrs. U. Waizmann for their assistance in the cleanroom;
- Dr. H. Neemann for answering all my questions about the Ph.D. procedures and sending me the related files;
- Mrs. H. Ludwig for her organizational competence and for her laughters that always made me happy;
- Mrs. D. Schumacher for her readiness to help and for informing us about the cultural events in Braunschweig;
- Mrs. G. Salman on behalf of the DAAD;
- Georg and Iris for their hospitality;
- My former officemates Martin and Erik, and my good old friends and flatmates Kaan and Alpan for their friendships;

- And finally my parents Ellen and Mahmut Sağol, my brother Ertan, my uncle Ahmet Sağol and my aunt Editha Maley for their continuous support in these last four years.

- Also my very very special thanks go to the Braunschweig Turkish Students Organization (BTÖB) for its unforgettably warm atmosphere and for its super-friendly members. In the name of BTÖB I especially thank Serhat, Cem Koyuncu, Alp, Erdeniz, Ismail, Timur, Cem Ünlü, Tuncay, Erdem, Güçlü, Korcan...

Resume

24.2.1973	born in Adana-Turkey as a son of Ellen and Mahmut Sağol
1979-1984	Ali Fuat Cebesoy Elementary School, Adana-Turkey
1984-1988	Tarsus American High School, Tarsus-Turkey
1988-1991	Ankara Science High School, Ankara-Turkey
1992-1996	Bachelor of Science in Physics (summa cum laude) Bilkent University, Ankara-Turkey
1996-1998	Master of Science in Physics Bilkent University, Ankara-Turkey Thesis: *Fabrication and Characterization of Semiconductor Double Quantum Well Diode Lasers* Supervisor: Prof. Dr. Ali Serpengüzel
1.12.1998	began the Ph.D. work
1.12.1998-30.9.2000	Max-Planck-Institut für Festkörperforschung, Stuttgart-Germany Department of Prof. Dr. Klaus von Klitzing Scholarship from the Max Planck Society
1.10.2000-31.3.2003	Technische Universität Braunschweig, Institut für Technische Physik, Braunschweig-Germany Group of Prof. Dr. Georg Nachtwei Scholarship from the German Academic Exchange Service